

Thesis Report

Geometrical Optics - Physical Optics model of the mutual coupling between antennas under integrated lenses

Ashwita Nair

Thesis Report

Geometrical Optics - Physical Optics model of
the mutual coupling between antennas under
integrated lenses

by

Ashwita Nair (5088062)

Supervisors

Prof. Nuria Llombart

Dr. Shahab Oddin Dabironezare

Master committee composition:

Prof. dr. N. Llombart	Professor, Academic Supervisor, Chair	TU Delft
Prof. dr. A. Neto	Professor, Committee	TU Delft
Dr. ir. R.F. Remis	Associate Professor, Committee	TU Delft
Dr. S.O. Dabironezare	Postdoc, Daily Supervisor, Committee	TU Delft



The work presented in this thesis was performed at:
Tera-Hertz Sensing Group
Department of Microelectronics
Faculty of Electrical Engineering, Mathematics and Computer Science
Delft University of Technology

Copyright © 2021 by Ashwita Nair.
All rights reserved.

An electronic version of this thesis is available at
<http://repository.tudelft.nl/>.

Geometrical Optics - Physical Optics model of the mutual coupling between antennas under integrated lenses

Thesis

This thesis is submitted in partial fulfillment of the requirements for the degree of

MASTER OF SCIENCE

in

ELECTRICAL ENGINEERING

at Delft University of Technology

by

Ashwita Nair

Acknowledgements

I have had the privilege of being taught and mentored by professors who truly inspired me with their utmost enthusiasm and expertise in their subjects. Your sheer passion and dedication motivated me to pursue my master thesis under the Terahertz Sensing group and so for that, I would like to extend my sincere gratitude to prof. dr. Andrea Neto, prof. dr. Nuria Llombart, and dr. Daniele Cavallo.

My master thesis journey has been an exciting one, and it could not have been possible without the guidance and support of everyone who facilitated it. Thus, it gives me immense pleasure to express my gratitude to each and every one of you.

First and foremost, I would like to thank my academic supervisor, prof. dr. Nuria Llombart. You have been an excellent supervisor and mentor, guiding me through the highs and lows of this project. I am completely in awe of your astute observation skills that have helped resolve various issues throughout the course of this thesis. I have also been fascinated by the way you bounce off new ideas and directions to think in, which gave me a glimpse of the rigour in research. There was something new to take away from every interaction with you, and I always looked forward to them.

I would also like to extend my sincere gratitude to my daily supervisor, dr. Shahab Dabironezare. Despite the online work format, you have constantly kept in touch with me to monitor my progress. You have always been available to clarify my doubts, help me with coding, review my work, and teach every new concept with time and patience. It was an absolute delight to work under your supervision. You have been an exceptional teacher and mentor to me. Every interaction with you made me feel more comfortable and confident about the work, especially with your ever-so-positive attitude. I cannot thank you enough for all the support and supervision.

I would also like to thank all my friends who have become akin to family here in Delft for their constant support and encouragement, especially Anil, Krishna, Poornashri, Avni, Gopika, Saurabh, Girish, and Aman.

Lastly, I would like to thank my little brother and my parents for believing in me and supporting my decision to pursue my master study in a new country. I would like to dedicate this thesis to you.

*bedankt iedereen
Ashwita Nair
Delft, August 2021*

Contents

Acknowledgements	i
1 Introduction	1
1.1 Mutual coupling in lens array systems	1
1.2 Methods to evaluate mutual coupling in Quasi-optical systems.	3
1.3 Thesis outline and contributions	4
2 Evaluation of Mutual Coupling	5
2.1 Mutual Coupling between two antennas in a homogeneous medium.	5
2.1.1 Calculating Magnetic Field over the receiver's Ground Plane - Analytical approach	6
2.1.2 CST simulation setup and validation.	6
2.1.3 Calculating mutual coupling between two CWG antennas.	9
2.2 Effect of Lens surface on the Mutual coupling between two antennas.	10
3 Geometrical Optics - Physical Optics (GO-PO) Model	12
3.1 Forward Ray-Tracing in a dielectric Lens	12
3.1.1 Determining the incident direction of propagation	12
3.1.2 Determining the intersection position of the incident rays with the elliptical lens surface	13
3.1.3 Determining reflected and transmitted direction of propagation	14
3.2 Geometrical Optics - Physical Optics Method.	15
3.2.1 Adding GO field contribution to the Ray tracing analysis.	16
3.2.2 Calculating the magnetic field inside the lens using PO method	18
3.3 Results and Validation	19
3.3.1 Small plastic lens case: $D_{lens} = 6\lambda_0$	19
3.3.2 Large plastic lens case: $D_{lens} = 15\lambda_0$	30
3.4 Bi-Directional Ray-Tracing via Reciprocity	35
3.4.1 Results and Validation	36
4 Case Study: Plastic Lens	39
4.1 Geometry of the considered plastic lenses	39
4.2 Considered plastic lens antenna feeds	40
4.3 Results and Inferences	41
4.3.1 Impact of lens diameter	41
4.3.2 Effect of feed pattern on mutual coupling	46
5 Case Study: Silicon Lens	49
5.1 Geometry of the considered silicon lenses	49
5.2 Considered silicon lens antenna feeds	50
5.3 Results and Inferences	51
5.3.1 Impact of the lens diameter	51
5.3.2 Effect of the feed pattern on the mutual coupling	55
6 Conclusion	58
6.1 Summary and Conclusion	58
6.2 Future Outlook	59
Bibliography	60

1

Introduction

In recent years, lens array architectures have become significantly more prominent in the literature in combination with integrated feed technologies to generate highly directive antenna patterns for high frequency applications. The lens array systems prove to be a potential candidate for 5G point-to-point communications [1], [2], wide-band wireless communications [3], [4], imaging systems [5], [6], and multiple-input multiple-output (MIMO) RADAR systems [7] with a few examples shown in Figure 1.1. This can be ascribed to their ease of integration with other electronic components to mitigate surface waves in relatively thick feed substrates at (sub)-millimeter wavelengths. Furthermore, the shape of the lens substantially improves the directivity and efficiency of the antenna system. The lens interface, however, generates reflections within the lens substrate, which can seriously affect the radiation properties of a lens array system [8]. When multiple feeds are placed under a lens or an array of lenses, these reflections increase the mutual coupling between the feeds thus making it a critical aspect to investigate while designing an integrated lens antenna system. The focus of this thesis is to study the effect of mutual coupling in lens antenna systems and propose a model to calculate and analyse this impact with a reasonable computational complexity and speed.

Phased Array for 5G point-to-point Communications



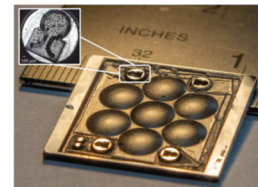
(a)

Fly's Eye Lens array for wideband wireless communications



(b)

Scanning Phased Array at Submillimeter Wavelengths



(c)

Figure 1.1: (a) Phased array for 5G point-to-point communications [1], (b) Fly's eye lens array for wideband wireless communications [3], and (c) Scanning phased array at sub-millimeter wavelengths [7].

1.1. Mutual coupling in lens array systems

In an array antenna system operating in reception mode, when the incident electromagnetic (EM) waves interact with an antenna element, a current is induced on the antenna. This induced current radiates a field that causes surface current on the neighbouring elements. As a result, the radio signal received by an antenna element represents the incoming signal but also a part of the signal received by its neighbouring radiating elements [9]. This effect is termed as mutual coupling. Figure 1.2 depicts this coupling in an antenna array. The mutual coupling alters the amplitude and phase of the induced current in each antenna element, thus affecting the antenna gain, pattern, resonant frequency, beamwidth, and input impedance [9].

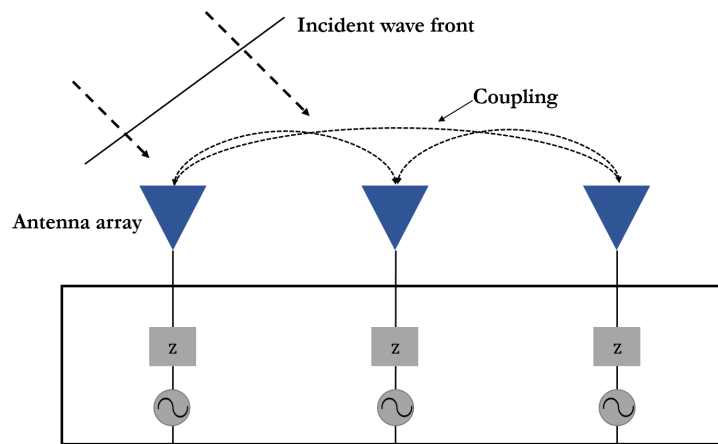


Figure 1.2: Mutual coupling between elements of an antenna array system.

There are several parameters that affect the mutual coupling level in an antenna array. One such critical parameter is antenna element spacing. As the spacing between the elements increases, the mutual coupling decreases. Various studies have shown that to achieve low mutual coupling, the element spacing should be larger than half-wavelength [9]. This in-turn makes the operating frequency also an important parameter that affects the mutual coupling.

But are these parameters equally significant in high frequency quasi-optical systems? Are there additional parameters that need to be taken into account for evaluating mutual coupling in these scenarios? Although there are substantial studies available in the literature on the mutual coupling in the context of phased and focal plane arrays [9], [10],[11], to the best of the knowledge of the author, there is not enough research performed on how the mutual coupling is impacted in high frequency quasi-optical systems. In the case of lens antenna array systems, multiple feeds are placed at the ground plane under a single lens or array of lenses depending upon the application demand.

Figure 1.3 depicts three different types of integrated lens antenna array configurations, their feed isolation requirements and their use in potential applications. For interferometry applications, the signals received by array elements are correlated and hence a feed isolation level in the order of 70 dB is required [12]. In lens phased array geometries, a single feed is placed under each lens element. In this case, the active impedance of the antenna elements is unaffected when the mutual coupling level is below -20 dB [13]. On the other hand, the isolation between antenna elements in lens array geometries for communication systems is related to the Signal to Noise Ratio (SNR) level required for the modulation. For example, in the Fly's eye lens array studied in [14], an SNR of 25 dB was required for the modulation of signals; therefore the mutual coupling level between antenna elements receiving different signals needed to be smaller than -25 dB [14]. Whereas, in a lens array geometry where the transmitting and receiving feeds are placed under the same lens, then a higher feed isolation in the order of 60 dB is required [14].

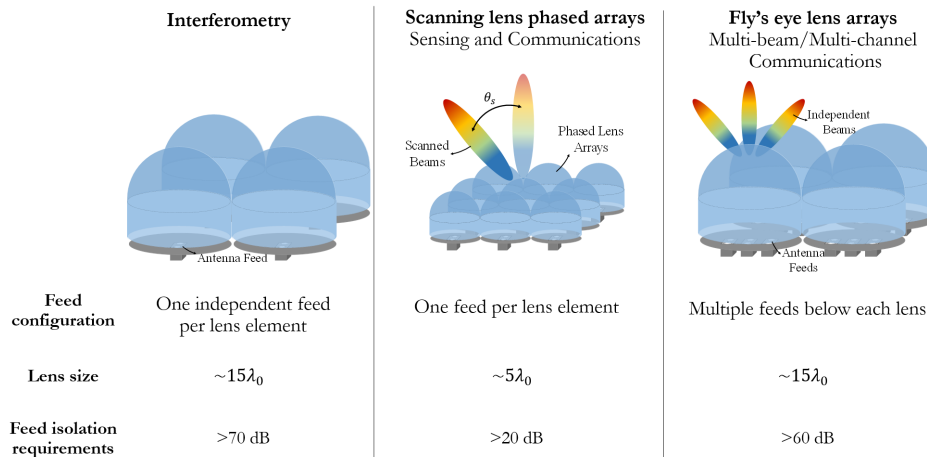


Figure 1.3: Examples of integrated lens antenna array geometries.

The mutual coupling between feeds in a lens array configuration is impacted by not just the adjacent radiating antenna element but also by the multiple reflections that occur at the lens surface as depicted in Figure 1.4 [8]. Although most of the power from the feeds are transmitted out of the lens, a portion is reflected back inside the lens due to the refraction that occurs at the lens interface. In fact, multiple reflections tend to occur at the lens surface. These reflected EM fields interact with the antenna elements present under the lens, thus increasing the mutual coupling between feeds which can degrade the antenna array performance. Therefore, in these configurations the mutual coupling can be significant even when the element spacing is greater than half-wavelength.

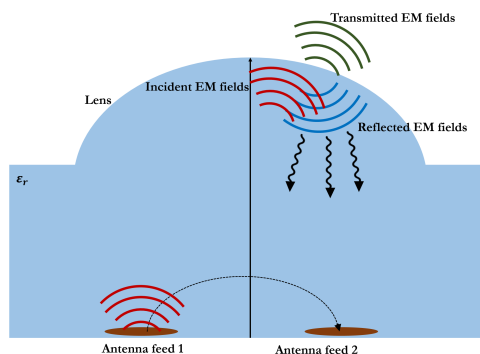


Figure 1.4: Effect of the lens surface on the mutual coupling between antenna feeds in a lens antenna system

In order to achieve the required feed isolation levels for various lens antenna systems, it becomes pertinent to study the effect of mutual coupling due to internal reflections inside a lens. The high frequency methods available in the literature that will aid to evaluate mutual coupling in quasi-optical systems are discussed in Section 1.2.

1.2. Methods to evaluate mutual coupling in Quasi-optical systems

There are several methods developed in the literature to analyse high frequency EM fields [15], [16], [17], [18]. Ray tracing is one such method that can be used to trace the path of the refracted EM fields when they interact with a surface that is large with respect to the wavelength. The method is well suited to model the path of the reflected EM fields from the lens surface to the ground plane. The field propagation paths can be either computed analytically or numerically. Various analytical and numerical approaches are available in the literature for ray tracing in lens antennas, [16], [19], [20], [21]. Even though the direction of the reflected EM waves can be determined accurately, the method does not provide the amplitude or phase information of these fields.

In order to obtain the EM fields for the evaluation of mutual coupling, the field calculation can be approximated using Geometrical Optics (GO) combined with Physical Optics (PO) approximation methods used for high frequency EM analysis [22], [23]. This method can be incorporated with the ray tracing analysis. In [8], a ray tracing approach is presented and combined with GO-PO approximations to evaluate the effect of the internal reflections on the input impedance of a feed placed at the focus of an elliptical lens [8]. According to the paper, the EM rays emanating from the source undergo reflections at the lens surface and the doubly reflected rays return to the focus [8], thus affecting the input impedance of the antenna element. Further, [19] uses ray tracing and GO-PO method to calculate mutual admittance between two slots spaced equally off-focus under a dielectric lens. It was found that the internal reflections on the dielectric lens impacted the mutual admittance value. The study also posited that in the plane where the direct coupling is weak, the lens reflections dominate the mutual admittance between the slots [19].

The mutual coupling between elements in a lens antenna system can also be computed accurately using full-wave simulations in terms of S-parameters. Nevertheless, the high computational cost and complexity in setting up these simulations make this approach impractical for optimization iterations and design states. Another method to evaluate mutual coupling is by performing physical measurements of the lens antenna systems which pose to be extremely expensive and will not give a clear picture of the internal reflections that occur inside the lens.

1.3. Thesis outline and contributions

The model proposed in this thesis incorporates the high frequency EM analysis techniques such as ray tracing and GO-PO approximations to compute mutual coupling between feeds placed under an elliptical lens. The model uses a simple analytical approach for forward ray-tracing. The mutual coupling is directly represented in term of S-parameter using an antenna in reception formulism instead of the mutual admittance parameter. The model takes as input the equivalent currents of the feed, thus making it capable of modelling mutual coupling for different feed types. The entire model is computationally efficient and provides the flexibility to rapidly study the mutual coupling behaviour in various scenarios such as different feed types, elliptical lens geometries, lens material, matching layer, and displacement of antenna elements to any location in the lens focal plane. The implemented method does not consider the diffraction effects at the lens edge [24] but takes into account the reflections at the surface until the second order reflections. It can be easily extended to higher order reflection effects as well. In the future this method will be extended and employed to analyse mutual coupling in applications with array of lenses with single or multiple feeds under each lens.

This thesis is divided into six chapters. Chapter 2 explains in detail the methodology for calculation of mutual coupling between two antennas. This chapter also puts forward an analytical model to evaluate mutual coupling between two antennas in a homogeneous medium and showcases the impact on this coupling when the two antennas are placed under a dielectric lens. In Chapter 3, a Geometrical Optics - Physical Optics (GO-PO) model is proposed that combines ray-tracing, geometrical optics and physical optics to obtain EM fields radiated from the lens surface back to its feeds which leads to the evaluation of mutual coupling between two feeds under a lens antenna system. The results attained from the GO-PO model is validated using CST MS fullwave simulation [25]. This model can be applied to different lens geometries, materials, feed types and feed locations. Using the GO-PO model, the effect of lens truncation angle, edge illumination and lens material on the mutual coupling between two feeds placed under a lens is studied and the inferences gained are documented as case studies in Chapters 4 and 5 for plastic and silicon lenses, respectively. Chapter 6 contains the conclusion of this thesis which summarizes the main ideas discussed in the thesis and then sets goals for the possible future work based on the research performed in this thesis.

2

Evaluation of Mutual Coupling

This chapter discusses the method used to evaluate mutual coupling between two antennas. Firstly, an analytical approach is presented for calculating the mutual coupling between two antennas in a homogeneous medium. This approach is validated using a full wave simulation in CST MS fullwave simulator [25]. Lastly, the effect of a lens surface on the mutual coupling between two antennas is studied.

2.1. Mutual Coupling between two antennas in a homogeneous medium

The mutual coupling between antennas placed in a homogeneous dielectric medium can be evaluated by considering two antennas. A transmitting test antenna \vec{M}_1 and a receiving one, \vec{M}_2 . These test antennas are placed in the homogeneous semi-infinite dielectric medium at a distance of R from each other as shown in Figure 2.1.

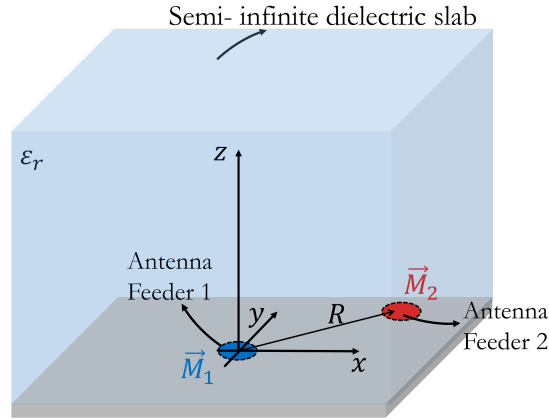


Figure 2.1: Two test antennas placed in homogeneous medium

For an arbitrary field incident on an antenna, one can resort to a reception formalism [26] by employing an equivalent Thevenin circuit. The induced open circuit voltage in this formalism can be evaluated over any surface \mathbf{S} enclosing the receiving test antenna \vec{M}_2 as [27]:

$$V_{oc} I_0 = \iint_S (\vec{H}_1 \cdot \vec{M}_2 - \vec{E}_1 \cdot \vec{J}_2) dS \quad (2.1)$$

where $[\vec{E}_1, \vec{H}_1]$ are the electric and magnetic fields radiated by the transmitting test antenna \vec{M}_1 over the surface \mathbf{S} . \vec{M}_2 and \vec{J}_2 are the equivalent magnetic and electric currents of the receiving test antenna when fed by a current I_0 . In the case where this surface \mathbf{S} is located at ground plane, the equation 2.1 reduces to:

$$V_{oc} I_0 = \iint_S 2(\vec{H}_1 \cdot \vec{M}_2) dS. \quad (2.2)$$

The magnetic field has a factor of two since the effect of the ground plane on the EM fields is taken into account by using the Image theorem with respect to $z = 0$ plane [28].

Assuming impedance matched antennas, the mutual coupling, S_{12} , can be calculated as:

$$S_{12} = \frac{P_{l2}}{P_{rad1}} = \frac{|V_{oc}I_0|^2}{16P_{rad1}P_{rad2}}. \quad (2.3)$$

where P_{l2} is the power delivered to the load of the receiving test antenna, and $P_{rad1/2}$ is the total power radiated by the test antennas 1 and 2 in the far-field, respectively. The magnetic field \vec{H}_1 is evaluated over the surface \mathbf{S} enclosing \vec{M}_2 using the analytical method described in section 2.1.1. This method is validated using a full wave CST simulation as shown in section 2.1.2.

2.1.1. Calculating Magnetic Field over the receiver's Ground Plane - Analytical approach

The magnetic field \vec{H}_1 radiated by the transmitting test source \vec{M}_1 can be calculated using the Green's function, \tilde{g}^{hm} , in a homogeneous medium as:

$$\vec{H}_1 = \iint_{A_1} \tilde{g}^{hm}(\vec{r} - \vec{r}') \vec{M}_1(\vec{r}') dS' \quad (2.4)$$

when the distance between the two test antennas $|\vec{\rho}_2 - \vec{\rho}_1|$ is much larger than $\frac{\lambda_d}{2\pi}$, where λ_d is the wavelength in the dielectric medium, the magnetic field can be computed using only the radiative components of the Green's function as shown:

$$\vec{H}_1 = -\frac{jk}{\zeta} \iint_{A_1} (\tilde{I} - \hat{R}\hat{R}) \frac{e^{-jkR}}{4\pi R} \vec{M}_1(\vec{r}') dS' \quad (2.5)$$

where k is the wave number, ζ is the characteristic impedance of the homogeneous medium, \tilde{I} is the identity matrix, $\hat{R} = \frac{\vec{r} - \vec{r}'}{|\vec{r} - \vec{r}'|}$ is the unit vector representing the direction from the source point (\vec{r}') to the observation point (\vec{r}); and A_1 is the spatial domain of the transmitting test antenna. This magnetic field is calculated at a surface \mathbf{S} enclosing antenna \vec{M}_2 using a reference system centred at test antenna \vec{M}_1 and considering the relative position of the two antennas as shown in Figure 2.2.

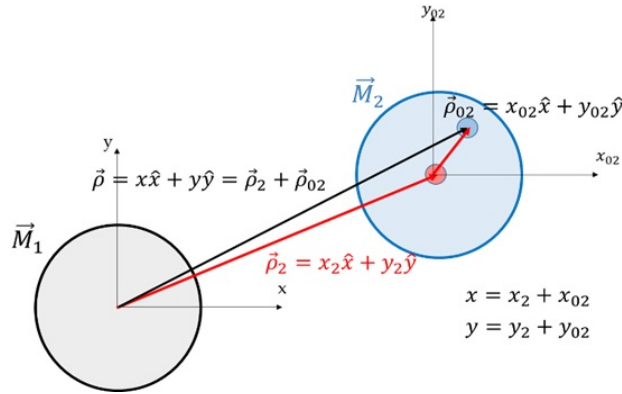


Figure 2.2: Relative position of the two test antennas

2.1.2. CST simulation setup and validation

A simulation model is set up in CST wherein an imported test antenna \vec{M}_1 is placed at the centre of a semi-infinite dielectric slab with a ground plane as shown in Figure 2.3. The magnetic field radiated by the antenna is calculated by the full wave simulator and exported at $z \approx 0$ (signifying ground plane) to the MATLAB environment.

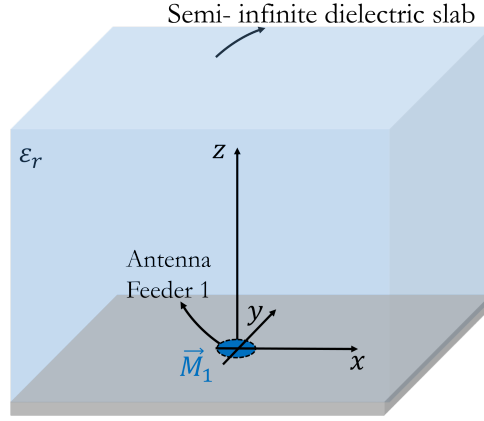


Figure 2.3: CST simulation setup

The induced open circuit voltage at antenna \vec{M}_2 is calculated as:

$$V_{oc}I_0 = \iint_{A_2} \vec{H}_{1x}(\rho_{02}, \phi_{02}) \cdot \vec{M}_2(\rho_{02}) d\rho_{02} d\phi_{02} \quad (2.6)$$

where ρ_{02} and ϕ_{02} indicate the radial and azimuth location of the receiving antenna with respect to a coordinate system centred at the centre of the receiving antenna (see Figure 2.2). Here the magnetic field exported from CST is evaluated at (ρ_{02}, ϕ_{02}) by performing a standard 2D interpolation in MATLAB.

In order to validate the analytical model, two circular waveguide (CWG) test antennas of diameter $D_f = 1.6\lambda_d$ are considered in a semi-infinite dielectric medium with relative permittivity of $\epsilon_r = 2.5$ (plastic) operating at a frequency of 300 GHz. The fundamental mode propagating in the considered CWG geometry is TE_{11} with the expression of its field distribution given in [29] and shown in equation 2.7, where J_1 is the first order Bessel function. The magnetic equivalent current (\vec{m}) of the CWG is calculated using the expression shown in equation 2.8, where \vec{E} is the electric field distribution and \hat{n} is the unit normal vector. The equivalent current and the normalized magnitude of the far-field radiated by this test antenna are as shown in Figures 2.4 and 2.5, respectively.

$$\begin{aligned} E_\rho &= \frac{-j\omega\mu}{k_c^2\rho} (-B \sin\phi) J_1(k_c\rho) e^{-j\beta z} & E_\phi &= \frac{j\omega\mu}{k_c} B \cos\phi J_1'(k_c\rho) e^{-j\beta z} \\ H_\rho &= \frac{-j\beta}{k_c} B \cos\phi J_1'(k_c\rho) e^{-j\beta z} & H_\phi &= \frac{-j\beta}{k_c^2\rho} (-B \sin\phi) J_1(k_c\rho) e^{-j\beta z} \\ H_z &= B \cos\phi J_1(k_c\rho) e^{-j\beta z} & B &= \sqrt{\frac{P_0 4k_c^4}{(p_{11}^2 - 1) J_1(k_c a) \pi \omega \mu \text{Re}(\beta)}} \end{aligned} \quad (2.7)$$

$$\vec{m} = \hat{n} \times \vec{E} \quad (2.8)$$

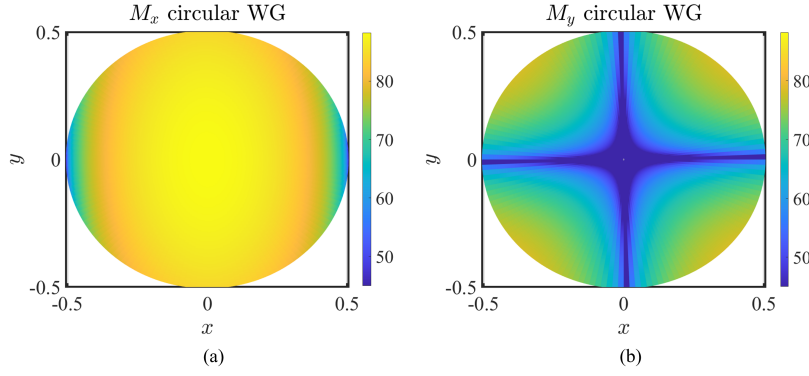


Figure 2.4: Equivalent magnetic currents at the opening of the considered circular waveguide for (a) co- (M_x) and (b) cross- (M_y) polarization

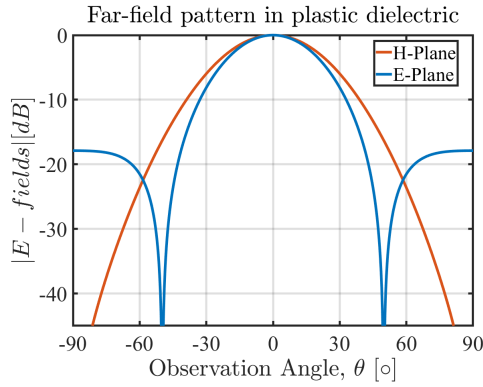


Figure 2.5: Far-field pattern of CWG in plastic ($\epsilon_r = 2.5$)

The magnetic field radiated by the described test antenna is computed by and exported from CST at $z \approx 0$ in both the main planes as shown in Figure 2.6. The figure also shows the magnetic field obtained using analytical approach as discussed in section 2.1.1. As it can be observed, the magnitude of the magnetic field evaluated using CST simulation and the one evaluated using the analytical approach are comparable in both planes. It is also evident that the magnetic field has a higher amplitude value in the E-plane. This is due to the fact that the far-field level of the antenna at 90° is more significant in the E-plane with respect to the H-plane as shown in Figure 2.5. The oscillations in the magnetic field from CST in the H-plane is due to the small reflections happening at the bounding box borders in CST MS simulation software.

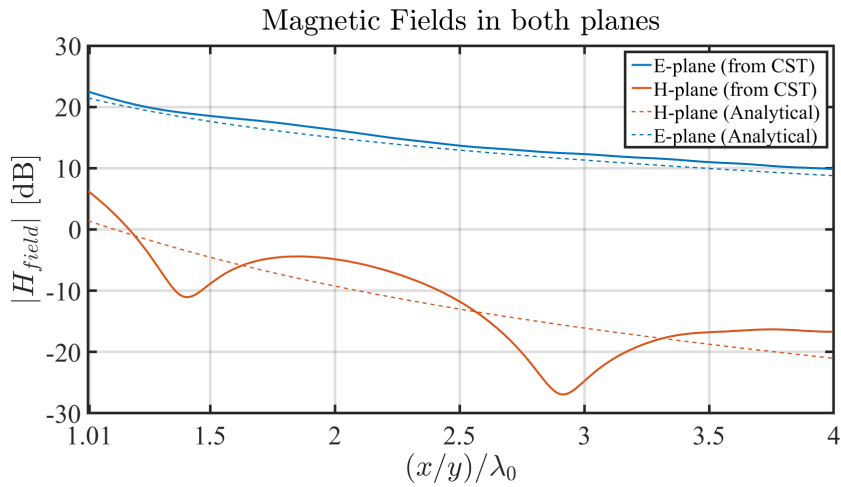


Figure 2.6: Magnetic Field of the test antenna at Ground plane in both planes

By using the magnetic field calculated at the receiving test antenna, the mutual coupling between the two test antennas can be evaluated using Equation 2.3. The simulation setup and the results obtained for this coupling are detailed in 2.1.3.

2.1.3. Calculating mutual coupling between two CWG antennas

To calculate the mutual coupling between the two test antennas as a function of their relative distance, the transmitting test antenna \vec{M}_1 is placed at the centre of a reference system and the receiving test antenna \vec{M}_2 is displaced along the E- and H-planes. The mutual coupling between the two antennas is calculated as a function of this displacement distance in both planes.

To validate the mutual coupling calculated analytically, three different CST simulations were set up and compared with the analytical method.

1. Case 1 : Using a single CWG placed in a semi-infinite medium

In this case a y-polarized CWG is modeled in CST and placed at the centre of a semi-infinite medium with $\epsilon_r = 2.5$ as shown in Figure 2.7 (a). The magnetic field radiated by this antenna is simulated and exported at the ground plane.

2. Case 2 : By importing the equivalent current of CWG to CST from MATLAB

In order to ensure that the CWG is operating at its fundamental mode (TE_{11}) and no higher order modes are considered, the magnetic currents are calculated analytically [29] and imported from MATLAB to CST as depicted in Figure 2.7 (b). Similar to Case 1, the magnetic field is simulated and exported back to MATLAB.

3. Case 3 : Using Two CWGs

Here, two CWGs are placed in a semi-infinite medium of $\epsilon_r = 2.5$ as shown in Figure 2.7 (c). The transmitting test antenna is placed at the centre of the setup. The receiving test CWG is displaced in the E-plane and H-plane. The mutual coupling between the two sources is calculated using CST as the S-parameter (S_{12}).

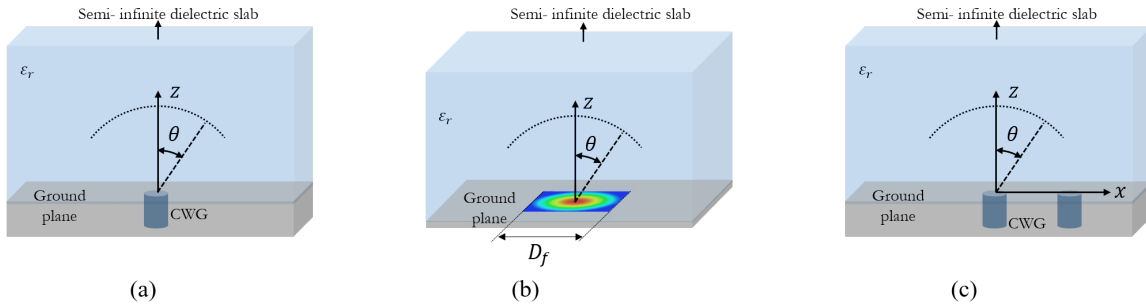


Figure 2.7: (a) Case 1: Single CWG in a semi-infinite medium, (b) Case 2: Equivalent current of CWG imported to CST, (c) Case 3: Using Two CWGs

Mutual coupling between the two antennas as a function of displacement in E- and H-planes is shown in Figures 2.8 and 2.9, respectively.

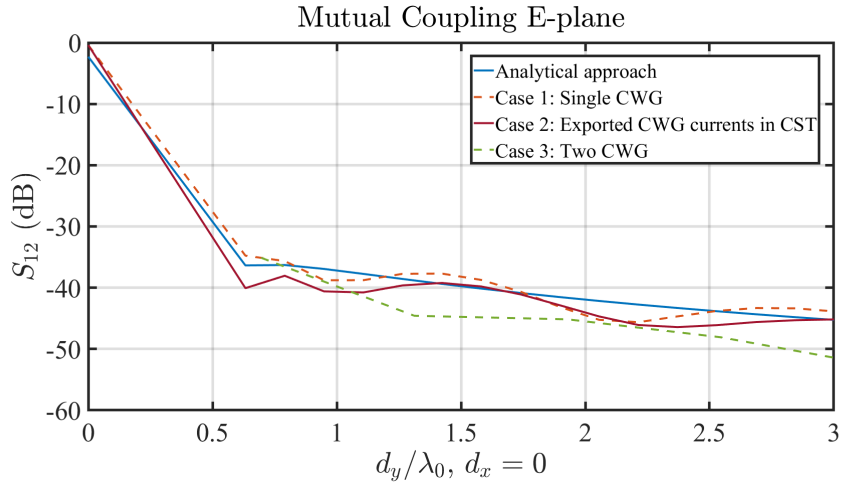


Figure 2.8: Mutual Coupling between two circular waveguides in a semi-infinite medium of $\epsilon_r = 2.5$ in E-Plane

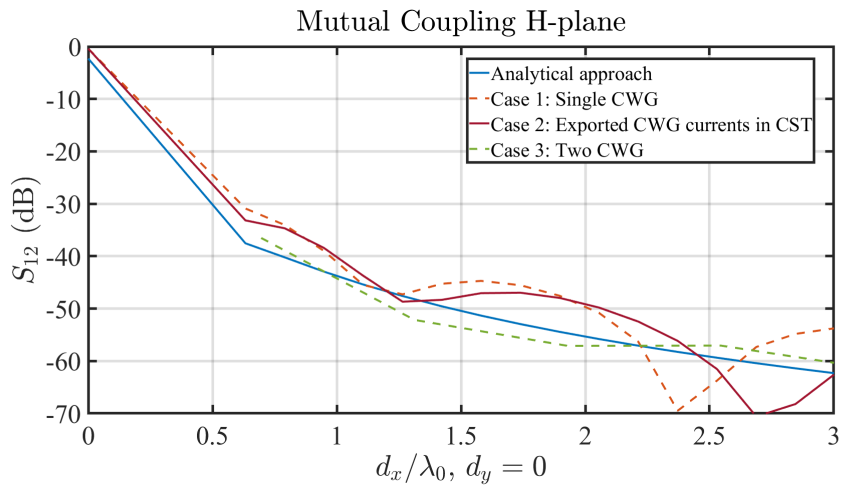


Figure 2.9: Mutual Coupling between two circular waveguides in a semi-infinite medium of $\epsilon_r = 2.5$ in H-Plane

It can be observed from the above graphs that the mutual coupling values obtained analytically for the two test antennas placed in a semi-infinite medium is comparable to the ones obtained from all the three CST simulation setups. The oscillations in the magnetic fields simulated in CST are due to the reflections at the edges of the simulation box.

2.2. Effect of Lens surface on the Mutual coupling between two antennas

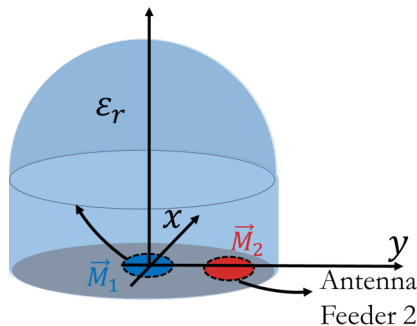


Figure 2.10: Two antennas placed under a Lens

When a truncated elliptical lens is placed over the semi-infinite dielectric slab as shown in Figure 3.3, the mutual coupling between the two antenna elements is significantly altered [19]. In order to understand the

impact of the lens surface, a plastic ($\epsilon_r = 2.5$) lens of diameter $D_{lens} = 6\lambda_0$ with a truncation angle of 30° is placed over the semi-infinite medium and the mutual coupling in this new geometry is compared with the one of the homogeneous medium. It is evident from Figure 2.11 that the presence of a lens surface increases the overall mutual coupling level between the two CWG antennas.

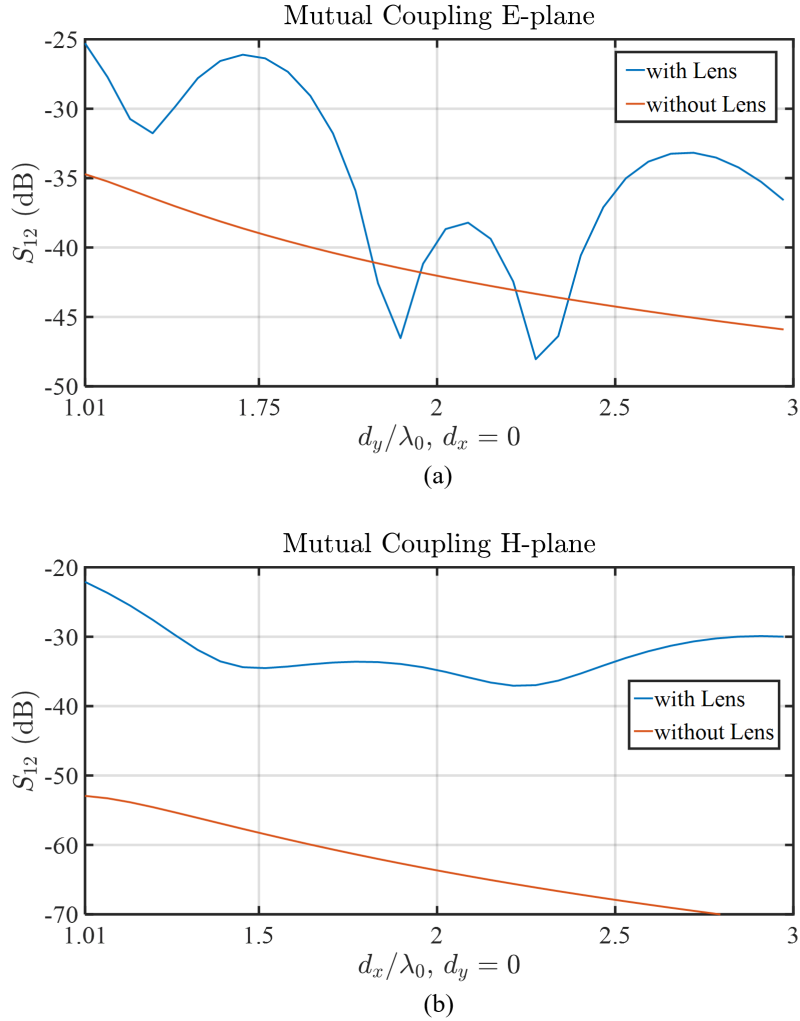


Figure 2.11: Comparison of mutual coupling between two antennas under a lens to that in a semi-infinite medium (a) E-Plane (b) H-Plane

The increase in the mutual coupling between the antennas below a lens surface can be attributed to the EM wave refraction that occurs at the intersection between the homogeneous dielectric medium and the second medium outside the lens (in this case the free space). Due to the change of material, a part of the incident power propagates to the second medium while a part reflects to the first medium at the intersection point. The reflected fields impinge on the ground plane thus increasing the mutual coupling levels [19]. Hence it is relevant to incorporate the effect of these secondary fields while calculating the mutual coupling between two antennas placed under a lens surface. The modelling of these refractions at the lens surface are discussed in detail in Chapter 3.

3

Geometrical Optics - Physical Optics (GO-PO) Model

This chapter delves into the modelling of the mutual coupling between two antenna elements when placed under a lens. The impact of the lens surface on the mutual coupling between two antenna elements/feeds is modelled using ray-tracing and Geometrical Optics - Physical Optics (GO-PO) approach as described in this chapter.

3.1. Forward Ray-Tracing in a dielectric Lens

Forward Ray tracing is a high frequency technique to analyze the EM fields transmitting through or reflecting from a generic and smooth (with respect to operation wavelength) surface. In this technique, EM radiation from an antenna is represented by a set of rays. These rays propagate in a homogeneous environment surrounding the antenna in straight lines. When these incident rays intersects with another medium (in this case a lens surface), they refract at the intersection points. Depending on the material of the second medium, part of the rays propagate through and part reflect from the intersection point. The direction of propagation of these secondary reflected or transmitted rays are approximated using Snell's law in optics. This approximation is reasonable when the surface of the secondary medium can be assumed locally flat, i.e. the surface is large in terms of the wavelength.

The key steps involved in the ray tracing technique include:

1. Determining the incident direction of propagation
2. Determining the intersection position of the incident rays with the elliptical lens surface
3. Determining the reflected and transmitted direction of propagation

3.1.1. Determining the incident direction of propagation

The energy of the EM fields propagates through an environment in the direction of its Poynting vector. Hence it can be assumed that the direction of propagation of the incident rays is the same as the Poynting vector.

$$\vec{S} = \frac{1}{2} \vec{E} \times \vec{H}^* \quad (3.1)$$

where \vec{S} is the Poynting vector, \vec{E} and \vec{H} are the electric and magnetic far-fields. Therefore, the direction of incident rays (\hat{s}_i) coming from the antenna can be represented as shown:

$$\hat{s}_i = \frac{\vec{S}}{|\vec{S}|} \quad (3.2)$$

Figure 3.1 depicts the EM far-fields as a set of rays propagating inside an elliptical lens whose direction of propagation is determined by the Poynting vector. It can be observed from the figure that if these rays are propagated farther they would intersect with the lens surface. Section 3.1.2 describes the approach used to determine the points at which the rays would intersect with the lens surface.

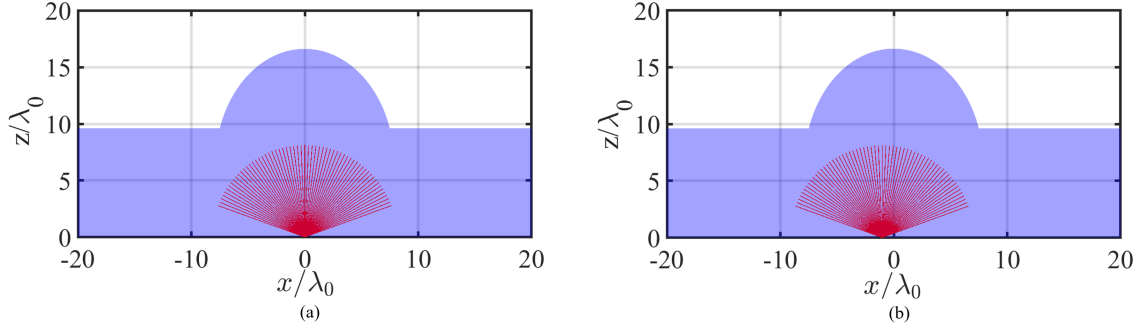


Figure 3.1: Direction of propagation of the incident rays (in red) from a source placed (a) at the focus of the ellipse, (b) displaced to -2 beams from its focus. The dielectric lens is made of plastic with $\epsilon_r = 2.5$ and diameter $D_{lens} = 15\lambda_0$

3.1.2. Determining the intersection position of the incident rays with the elliptical lens surface

The positions at which each incident ray will intersect with the lens surface can be derived by using the below equation:

$$Q_2^x = Q_1^x + Ss_i^x \quad Q_2^y = Q_1^y + Ss_i^y \quad Q_2^z = Q_1^z + Ss_i^z \quad (3.3)$$

where s_i^x , s_i^y , s_i^z are the Cartesian components of the incident direction; Q_1^x , Q_1^y and Q_1^z are the x, y and z starting points of the incident rays, Q_2^x , Q_2^y and Q_2^z are the x, y and z intersection position on the lens surface and S is the propagation length of the incident rays which is unknown. The positions on the lens surface are related by the equation of an ellipsoid as shown:

$$\frac{z_2^2}{a^2} + \frac{y_2^2}{b^2} + \frac{x_2^2}{b^2} = 1 \quad (3.4)$$

where a and b are the ellipsoid's semi-major and semi-minor axis, respectively. By substituting x_2 , y_2 and z_2 as the positions Q_2^x , Q_2^y and Q_2^z for the lens surface, Equation 3.3 becomes:

$$x_2 = Q_1^x + Ss_i^x \quad y_2 = Q_1^y + Ss_i^y \quad a\sqrt{1 - \frac{x_2^2 + y_2^2}{b^2}} = Q_1^z + Ss_i^z \quad (3.5)$$

Equation 3.5 can be solved further to form:

$$Q_1^z + Ss_i^z = a^2 - \frac{a^2}{b^2} [(Q_1^x + Ss_i^x)^2 + (Q_1^y + Ss_i^y)^2] \quad (3.6)$$

$$S^2 [(s_i^z)^2 + \frac{a^2}{b^2} ((s_i^x)^2 + (s_i^y)^2)] + S [2Q_1^z s_i^z + 2\frac{a^2}{b^2} (Q_1^x s_i^x + Q_1^y s_i^y)] + [(Q_1^z)^2 - a^2 + \frac{a^2}{b^2} ((Q_1^x)^2 + (Q_1^y)^2)] = 0 \quad (3.7)$$

The propagation distance S for each incident ray can be calculated by solving Equation 3.7 which is of the form of a second order equation $AS^2 + BS + C = 0$, thus giving the intersection position for the incident rays on the lens surface. Figure 3.2 shows the incident rays intersecting with the lens surface.

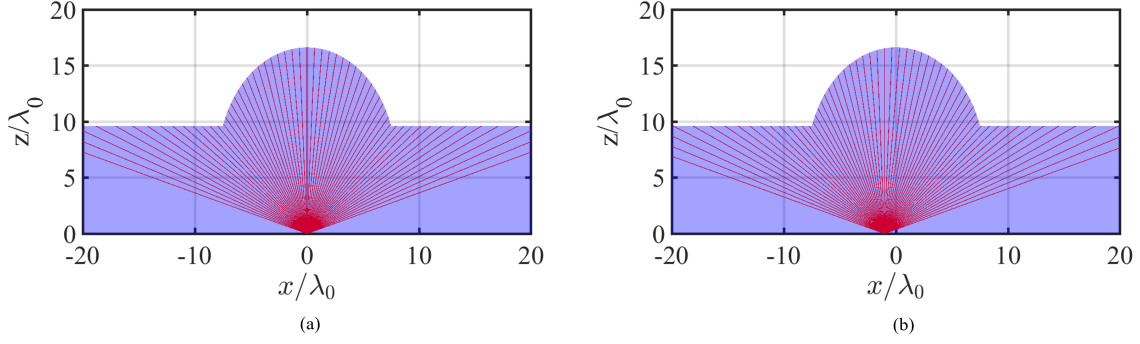


Figure 3.2: Incident rays intersecting with the lens surface when the antenna is placed (a) at the focus of the ellipse, (b) displaced to 2 beams from its focus. The dielectric lens is the same as the one in Figure 3.1

3.1.3. Determining reflected and transmitted direction of propagation

The incident rays propagate with direction of \hat{s}_i through the lens medium until it intersects with the lens surface as depicted in Figure 3.3. At the point of intersection the secondary transmitted and reflected direction of propagation can be approximated using the Snell's law [30].

$$\hat{s}_r = \hat{s}_i - 2(\hat{s}_i \cdot \hat{n})\hat{n} \quad (3.8)$$

$$\hat{s}_t = \frac{n^i}{n^t} \hat{s}_i + \left[\frac{n^i}{n^t} \cos \theta^i - \cos \theta^t \right] \hat{n} \quad (3.9)$$

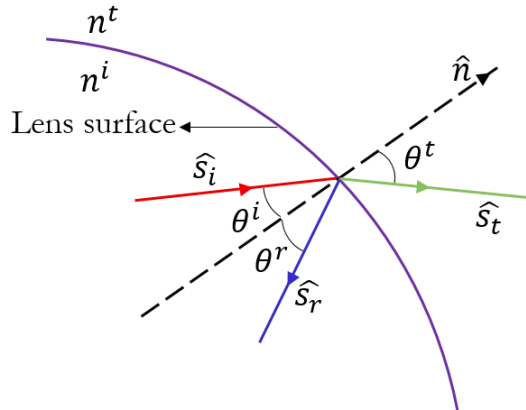


Figure 3.3: Direction of propagation of the incident, transmitted and reflected rays at an intersection point on the lens surface.

where θ^i , θ^r and θ^t represent the angle between the normal vector of the boundary surface, \hat{n} , with the direction of the incident, reflected and transmitted rays, respectively. $n^i = \sqrt{\epsilon_r^i}$ and $n^t = \sqrt{\epsilon_r^t}$ are the refractive indexes of the incident and transmission materials, respectively. The incident angle θ^i and transmitted angle θ^t are calculated as a function of the refractive index and the direction of propagation. Figure 3.4 shows the incident (red), reflected (blue) and transmitted (green) rays at the surface of an elliptical lens.

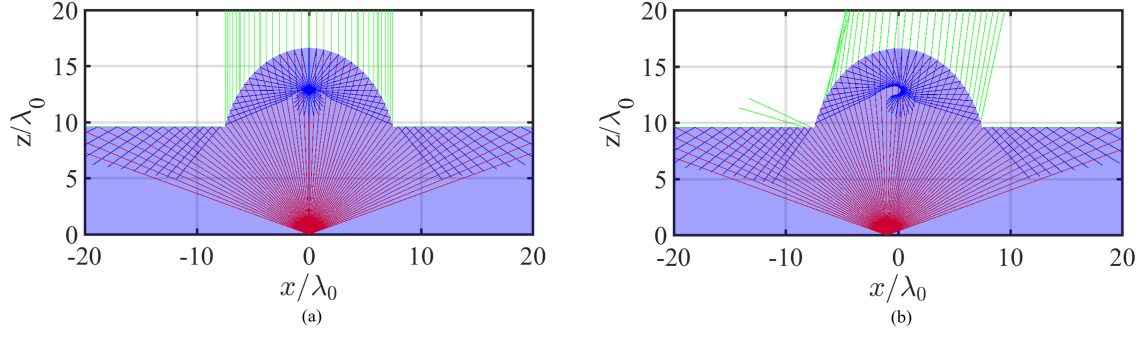


Figure 3.4: Ray tracing for an antenna placed (a) at the focus (b) displaced to -2 beams from the focus of a lens with $\epsilon_r = 2.5$ and $D_{lens} = 15\lambda_0$. The incident rays, reflected rays and the transmitted rays are depicted by red, blue and green coloured rays, respectively.

There are two main inferences that can be drawn from the above figure:

1. All the reflected rays (in blue) intersect with each other either at or around the second focus of the elliptical lens (caustic point).
2. If the reflected rays are propagated further, a part of the reflected rays will hit the ground plane below the lens, and a part will hit the lens surface again to form the secondary reflections.

The secondary reflections can be also modeled by the ray tracing analysis. Since the positions of the reflected rays on the lens surface and their direction of propagation is known along with the lens equation, the propagation distance of these reflected rays can be calculated by following all the above described steps. Figure 3.5 shows the ray tracing model incorporated with the secondary reflections.

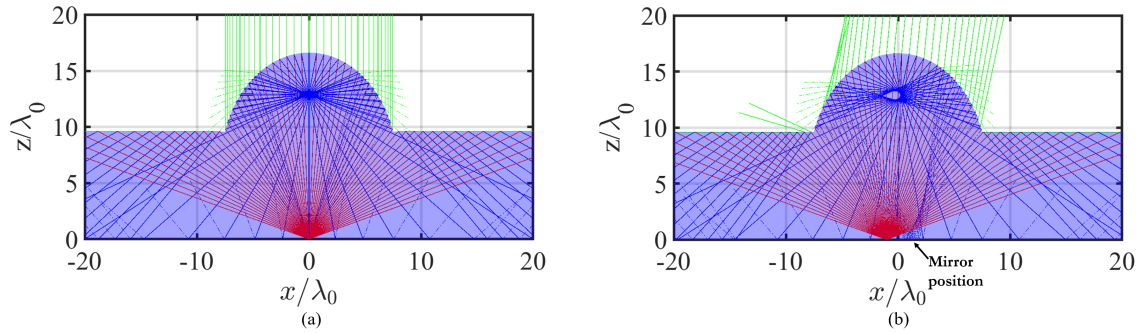


Figure 3.5: Ray tracing picture with first (solid lines) and second (dash-dotted lines) order rays, where the incident, reflected and transmitted rays are indicated with red, blue, and green colours, respectively. Antenna placed (a) at the focus (b) displaced to -2 beams from the focus of a lens with $\epsilon_r = 2.5$ and $D_{lens} = 15\lambda_0$.

In the case where the antenna is placed at the lower focus of the elliptical lens, the secondary reflections converge at the same focus of the lens. When the antenna is displaced from the focus of the lens, the secondary reflections converge at a mirror point with respect to the antenna position as depicted in Figure 3.5(b).

3.2. Geometrical Optics - Physical Optics Method

In this section the Geometrical Optics - Physical Optics (GO-PO) method is detailed, to model the impact of high frequency EM field reflections from the lens surface on the mutual coupling [15]. The GO-PO approach is employed to both the primary and secondary reflections from the lens surface.

3.2.1. Adding GO field contribution to the Ray tracing analysis

Geometrical Optics (GO) is a high frequency technique that approximates the EM propagation by tubes of rays with specific amplitude, phase and polarization characteristics [22], [17]. This technique assumes that the amplitude of the EM fields spreads as it propagates along the ray path and its phase oscillates [22]. The GO technique can be added to the ray-tracing method to represent both the amplitude and phase of the electric and magnetic fields on the lens surface.

In order to compute the GO contribution of the incident field on the lens surface, the steps below are followed:

1. The antenna far-field is calculated in a semi-infinite medium ($\vec{E}_i(Q_{FF})$). This far-field has a spherical wavefront originating from the antenna location. Therefore, its principle radii of curvature are equal to the radius of the far-field sphere, i.e, $\rho_1^i = \rho_2^i = R_{FF}$ as shown in Figure 3.6
2. The intersection points P_1 from the antenna to the lens surface are found using the ray tracing method as described in Section 3.1
3. The incident electric field ($\vec{E}_i(P_1)$) radiated by the antenna at the position P_1 for each ray is computed as a function of the far-field of the antenna, the amplitude spreading factor and phase term given by the equation:

$$\vec{E}_i(P_1) \approx \vec{E}_i(Q_{FF}) S_{spread}(Q_{FF}) e^{-jks} \quad (3.10)$$

where, k is the wavenumber, s is the distance between the lens surface and the far-field sphere of the antenna ($r_l - R_{FF}$) and $S_{spread}(Q_{FF})$ is the amplitude spreading factor. The GO method approximates the amplitude of the EM fields by spreading them along the propagation ray path. This amplitude spread is calculated as [22]:

$$S_{spread} = \sqrt{\frac{\rho_1 \rho_2}{(\rho_1 + s)(\rho_2 + s)}} \quad (3.11)$$

S_{spread} is a function of the principle radii of curvature, ρ_1 and ρ_2 , of the EM rays and s is the ray path length. The more complete expression of the spreading factor includes phase jumps where a ray crosses one or both of its caustic points. Ray caustics occur whenever a family of rays merge or intersect at a single point [22]. Specifically, a ray caustic occurs in a location ahead of the ray path if a radius of curvature is negative (converging) or occurs behind the ray path if the radius of curvature is positive (corresponding to a diverging behaviour). For example, consider the ray tracing case as shown in Figure 3.5 (a). The incident rays hit the lens curvature and the reflected rays (solid blue lines) all pass through the same point (upper focus of the ellipse) hence causing ray caustics in the forward path of the rays.

A caustic is crossed if $\rho_{1,2} < 0$ and $s > -|\rho_1|$ or $s > -|\rho_2|$, which leads to a change of sign in the denominators of Equation 3.11. Hence a phase jump of $\frac{\pi}{2}$ due to the caustic traversal is included to the Spreading factor [22]:

$$\sqrt{\frac{\rho_i}{(\rho_i + s)}} = \left| \sqrt{\frac{\rho_i}{(\rho_i + s)}} \right| e^{j\pi/2} \quad (3.12)$$

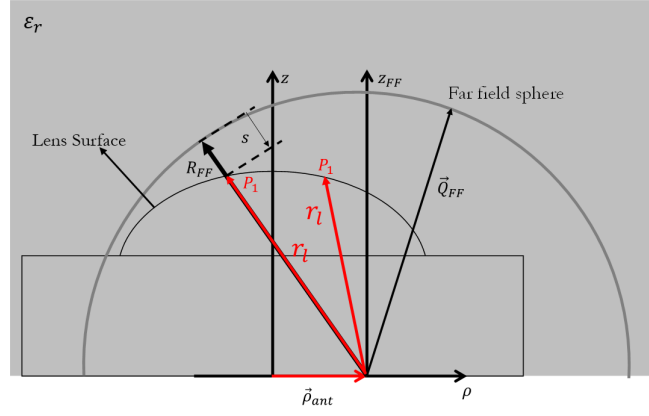


Figure 3.6: GO propagation scenario for incident rays in a homogeneous dielectric material

When the incident EM fields interact with a lens surface the following changes occur:

1. Change in the direction of propagation of the rays, leading to reflected and transmitted rays as observed in the ray tracing. The reflected (\hat{k}_r) and transmitted (\hat{k}_t) propagation unit vectors are calculated using Snell's law as shown below:

$$\hat{k}_r = \hat{k}_i - 2(\hat{k}_i \cdot \hat{n})\hat{n} \quad (3.13)$$

$$\hat{k}_t = \frac{\hat{k}_i}{\sqrt{\epsilon_t}} - \frac{1}{\sqrt{\epsilon_t}} \left[(\hat{k}_i \cdot \hat{n}) + \sqrt{\epsilon_t - [1 - (\hat{k}_i \cdot \hat{n})^2]} \right] \hat{n} \quad (3.14)$$

where \hat{k}_i is the propagation constant of the incident ray and \hat{n} is the normal vector.

2. The incident radii of curvature of the rays are altered from ρ_1^i and ρ_2^i to $\rho_1^{r/t}$ and $\rho_2^{r/t}$ (reflection and transmission radii of curvature). These new radii of curvatures are related to $\rho_{1,2}^i$, and the geometry of the discontinuity surface as described in [31].
3. The TE and TM polarized portions of the field have different reflection and transmission coefficients at the lens surface. The TE and TM polarization of the incident/reflected/transmitted fields are defined based on the direction of propagation and the normal vector, as [30].

$$\hat{p}_{i/r/t}^{TE} = \frac{\hat{k}_{i/r/t} \times \hat{n}}{|\hat{k}_{i/r/t} \times \hat{n}|} \quad (3.15)$$

$$\hat{p}_{i/t}^{TM} = \hat{p}_{i/t}^{TE} \times \hat{k}_{i/t} \quad \hat{p}_r^{TM} = \hat{k}_r \times \hat{p}_r^{TE} \quad (3.16)$$

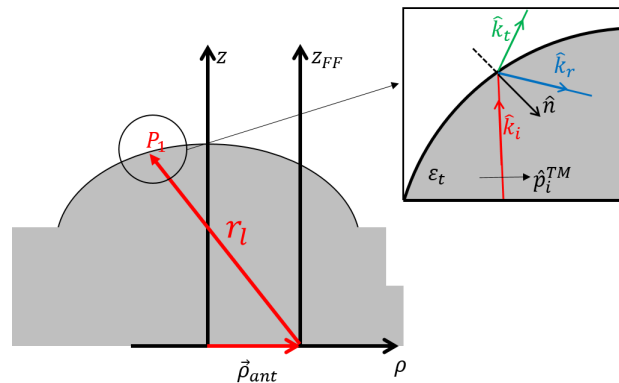


Figure 3.7: The polarization and direction of propagation of the reflected and transmitted GO fields.

The scattered GO fields (reflected and transmitted) on the lens surface, $\vec{E}_{r/t}(P_1)$, are calculated as:

$$\vec{E}_r(P_1) = \vec{E}_i(P_1) \cdot \vec{R}(P_1) \quad (3.17)$$

$$\vec{E}_t(P_1) = \vec{E}_i(P_1) \cdot \vec{T}(P_1) \quad (3.18)$$

where, $\vec{R} = \Gamma^{TE} \hat{\rho}_i^{TE} \hat{\rho}_r^{TE} + \Gamma^{TM} \hat{\rho}_i^{TM} \hat{\rho}_r^{TM}$ and $\vec{T} = \tau^{TE} \hat{\rho}_i^{TE} \hat{\rho}_r^{TE} + \tau^{TM} \hat{\rho}_i^{TM} \hat{\rho}_r^{TM}$ are the reflection and transmission dyads, respectively. $\Gamma^{TE/TM}$ and $\tau^{TE/TM}$ are the Fresnel reflection and transmission coefficients, respectively [30].

The incident, reflected and transmitted magnetic fields on the lens surface are approximated by assuming a local plane wave relation between EM fields at each P_1 position as shown below:

$$\vec{H}_{i/r/t}(P_1) = \frac{1}{\zeta_{i/r/t}} \hat{k}_{i/r/t} \times \vec{E}_{i/r/t}(P_1) \quad (3.19)$$

where, $\zeta_{i/r/t}$ are the characteristic impedance of the incident, reflected, and transmitted medium, respectively; and $\hat{k}_{i/r/t}$ are the unit propagation vectors of the incident/reflected/transmitted EM fields. Once the electric and magnetic fields are calculated over the lens surface, a Physical Optics (PO) technique can be used to calculate the EM fields inside the lens as described in Section 3.2.2.

3.2.2. Calculating the magnetic field inside the lens using PO method

In order to compute the mutual coupling between antennas below a lens, the magnetic field needs to be evaluated on the ground plane inside the lens. This can be achieved by using a PO approach as described below.

By using the incident and reflected fields calculated using the GO method, as described in Section 3.2.1, a set of equivalent currents can be approximated assuming local flat surface as shown in Figure 3.8. These equivalent currents are related to the GO fields as:

$$\vec{J}_s \approx \hat{n} \times [\vec{H}_i + \vec{H}_r] \quad \vec{m}_s \approx -\hat{n} \times [\vec{E}_i + \vec{E}_r] \quad (3.20)$$

where, \vec{J}_s and \vec{m}_s are the equivalent electric and magnetic currents, respectively; and \hat{n} is the normal vector at each position on the lens surface.

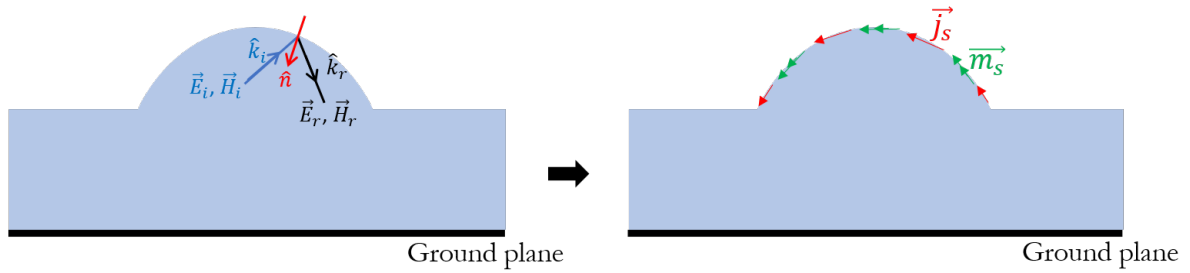


Figure 3.8: Physical Optics (PO) approximation for the equivalent currents on a lens surface

Since the lens is placed over a ground plane, the effect of the ground plane on the EM fields should be taken into account using the Image theorem with respect to $z = 0$ plane [28]. Figure 3.9 depicts the imaged geometry that accounts for the presence of the ground plane. The total equivalent electric and magnetic currents thus would be multiplied by a factor of two.

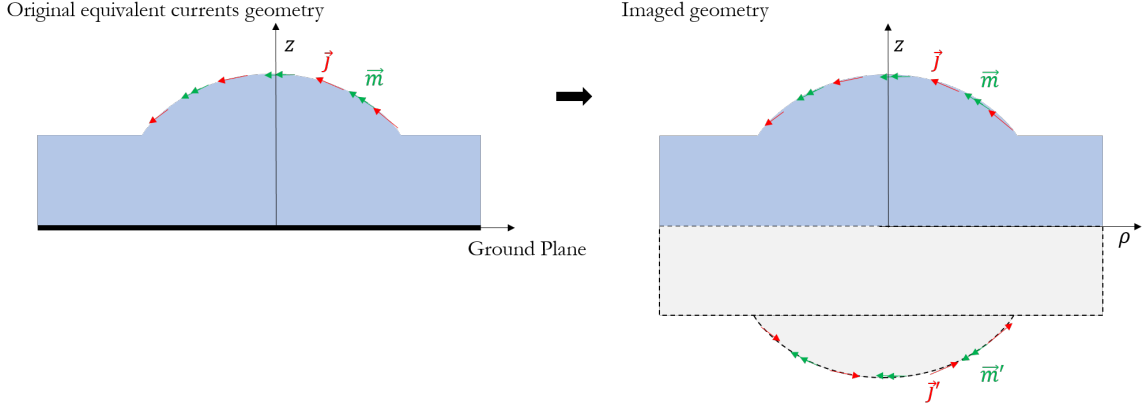


Figure 3.9: Substituting the effect of the ground plane on EM fields using imaged currents.

The magnetic field, $\vec{H}(\vec{r})$, is calculated at the observation point (in this case, the ground plane) using the radiative part of the Green's functions, i.e, $\vec{\nabla} \simeq -jk\hat{k}$ [31] as shown below:

$$\vec{H}_1(\vec{r}) = \frac{-jk_i}{\zeta_i} \int_s \left[\vec{m}(\vec{r}') - (\hat{k}(\vec{r}') \cdot \hat{m}(\vec{r}')) \hat{k}(\vec{r}') \right] \frac{e^{-jk_d|\vec{r}-\vec{r}'|}}{4\pi|\vec{r}-\vec{r}'|} dS' \quad (3.21)$$

where, k_i is the propagation constant of the incident medium, ζ_i is the characteristic impedance of the incident medium, \vec{m}_s is the equivalent magnetic current on the lens surface, \vec{r}' is the equivalent source position (in this case the lens surface) and \vec{r} is the observation point (in this case the ground plane).

Once the magnetic fields are evaluated at the ground plane for primary and secondary reflections, the open circuit voltage for the receiving test source can be evaluated using the expression given in Equation 2.2, and the mutual coupling between the two antennas can be calculated using Equation 2.3. Section 3.3 shows the mutual coupling results obtained for two antennas placed under a lens by using the GO-PO model. These results are compared and validated using CST MS fullwave simulation.

3.3. Results and Validation

The mutual coupling between two antennas placed under a single lens is calculated using the GO-PO model and is validated against the results obtained from CST MS fullwave simulator. For this purpose, two lens diameters are considered - $D_{lens} = 6\lambda_0$ and $D_{lens} = 15\lambda_0$ with the same dielectric constant, $\epsilon_r = 2.5$. These two lens diameters are relevant for phased array and Fly's eye applications.

3.3.1. Small plastic lens case: $D_{lens} = 6\lambda_0$

In order to validate the model for the smaller lens, a CWG source, defined in Section 2.1.2, is considered. The GO-PO model for calculating the mutual coupling between two antennas placed under a lens is compared with the mutual coupling values obtained by exporting the magnetic fields from a CST MS fullwave simulation. The specifications of the antenna and lens are as described below:

- Source type = Circular waveguide (CWG)
- Waveguide opening diameter, $D_f = 1.6\lambda_d$
- Lens diameter, $D_{lens} = 6\lambda_0$
- Lens material, $\epsilon_r = 2.5$, plastic
- Lens f-number, $f_{\#} = 0.812$ ($\theta_0 = 38^\circ$)

The results obtained using the GO-PO model is compared with the ones of the CST simulation for two scenarios:

- On-axis antenna: Test antenna \vec{M}_1 placed at focus of the lens

- Off-axis antenna: Test antenna \vec{M}_1 is displaced to $-1.5\lambda_d f_{\#}$ position from the focus of the lens which corresponds to scanning 1.5 beams using the lens

3.3.1.1. On-axis transmitting test antenna

The equivalent currents of a single CWG antenna is imported to CST MS fullwave simulator from MATLAB. The CWG antenna is placed at the focus of the truncated plastic lens as shown in Figure 3.10. The magnetic fields calculated at the ground plane ($z \approx 0$) of the lens using the CST MS is exported to MATLAB to calculate the mutual coupling between two CWG antennas under a lens as a function of their relative distance. These magnetic fields and mutual coupling values are compared with the ones obtained by using the GO-PO model.

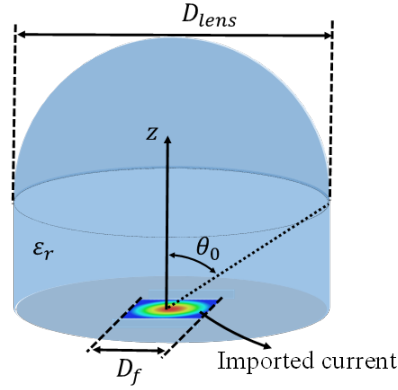


Figure 3.10: Equivalent currents of a CWG imported to CST and placed at the focus of a lens with dielectric constant $\epsilon_r = 2.5$ and lens diameter $D_{lens} = 6\lambda_0$

Although multiple reflections occur when the EM rays hit the lens surface, in this model only the primary (1^{st}) and secondary (2^{nd}) reflections are considered. This is due to the fact that when the EM fields interact with the lens surface most of the power radiated by the antenna is transmitted out of the lens, hence the power contained in the subsequent reflections becomes less significant and its effect on the mutual coupling is neglected here. The ray tracing analysis for the lens of diameter $D_{lens} = 6\lambda_0$ when an antenna is placed at the focus of the lens is as depicted in Figure 3.11 across the H-plane.

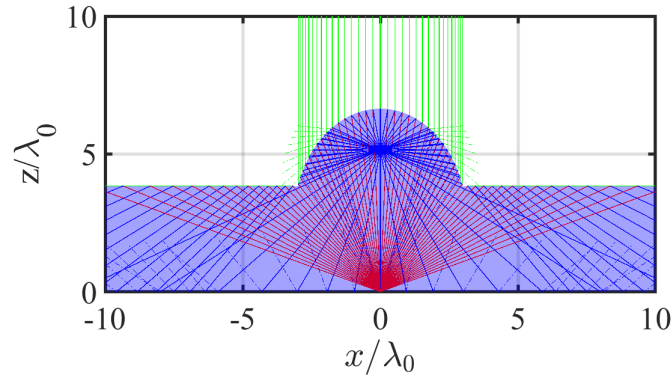


Figure 3.11: Ray-tracing for an antenna placed at the focus of a lens with a dielectric constant of $\epsilon_r = 2.5$ and lens diameter, $D_{lens} = 6\lambda_0$

The 2D incident, reflected and transmitted GO fields for primary and secondary reflections on the lens surface are shown in Figure 3.12 and Figure 3.13, respectively.

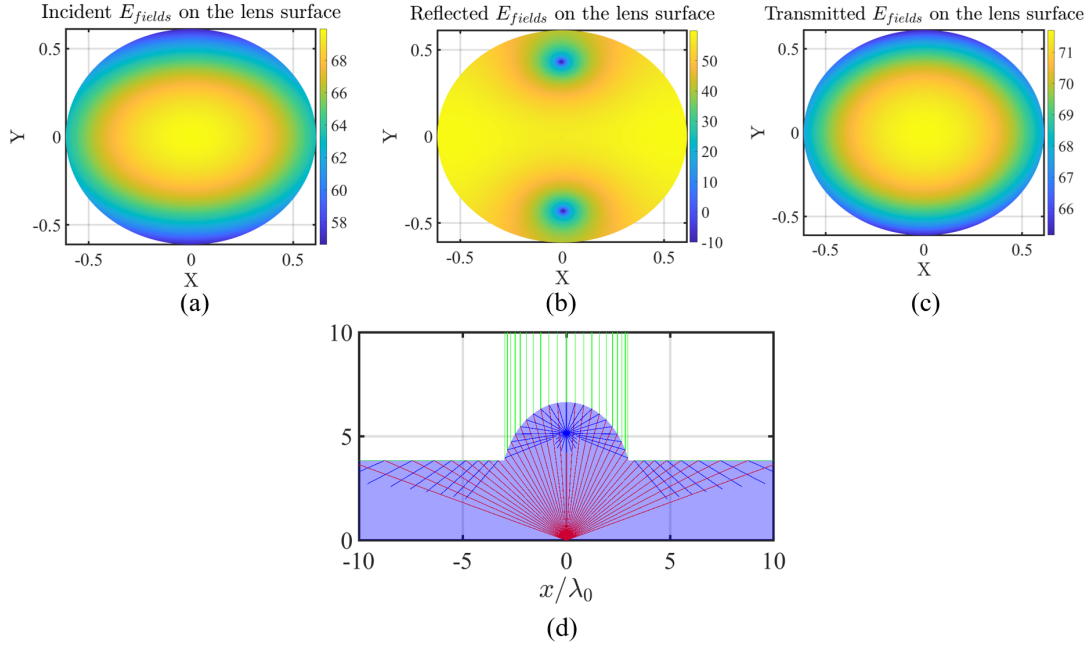


Figure 3.12: (a) Incident, (b) reflected, and (c) transmitted GO fields on the lens surface from primary reflections when the antenna is placed at the focus of the lens as shown in (d) ray-tracing picture.

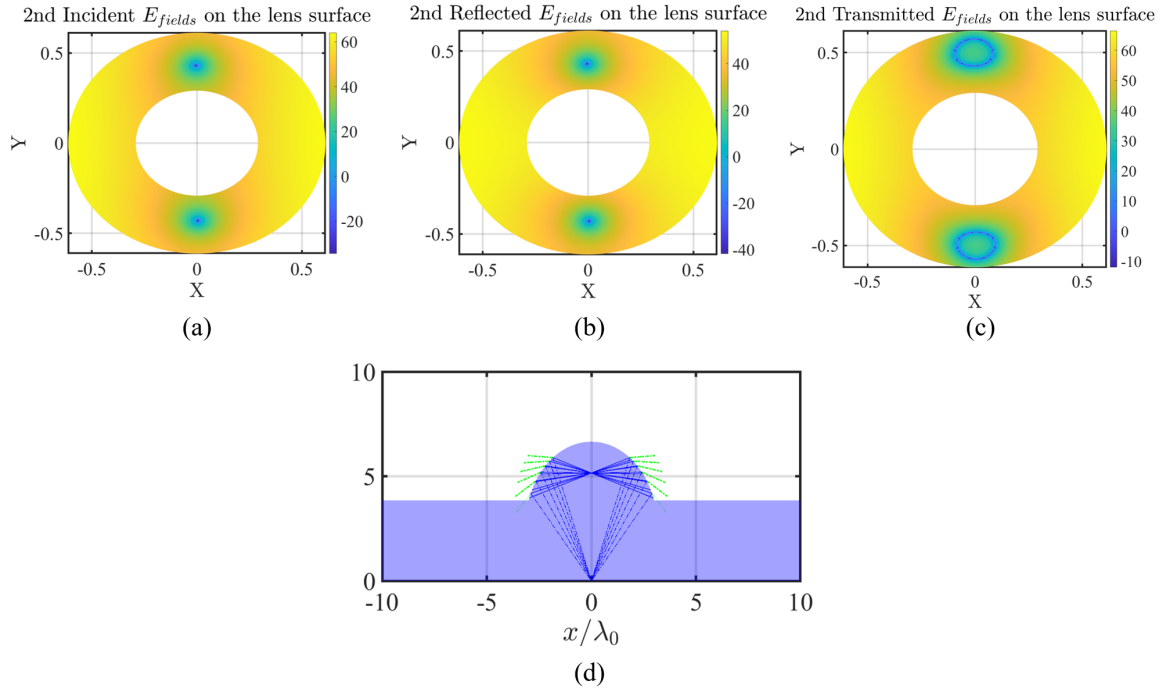


Figure 3.13: (a) Incident, (b) reflected, and (c) transmitted GO fields on the lens surface from secondary reflections when the antenna is at the focus of the lens as shown in (d) ray-tracing picture.

The magnetic field obtained on the ground plane in the H- and E- plane using the PO approximation is shown in Figure 3.14 (a) and (b), respectively, for both reflection scenarios. It is evident from the graphs that the magnetic fields from first reflections (shown in red) are uniformly spread across the ground plane, whereas the fields from second reflections (shown in yellow) have a higher value near the focus of the lens and taper down farther away from the focus. This finding is in agreement with the ray-tracing picture shown in Figure 3.11 and as discussed in [19]. The total magnetic field obtained on the ground plane under the lens is calculated as a summation of the magnetic fields approximated from each contribution - homogeneous medium (direct coupling) + 1st reflection + 2nd reflection.

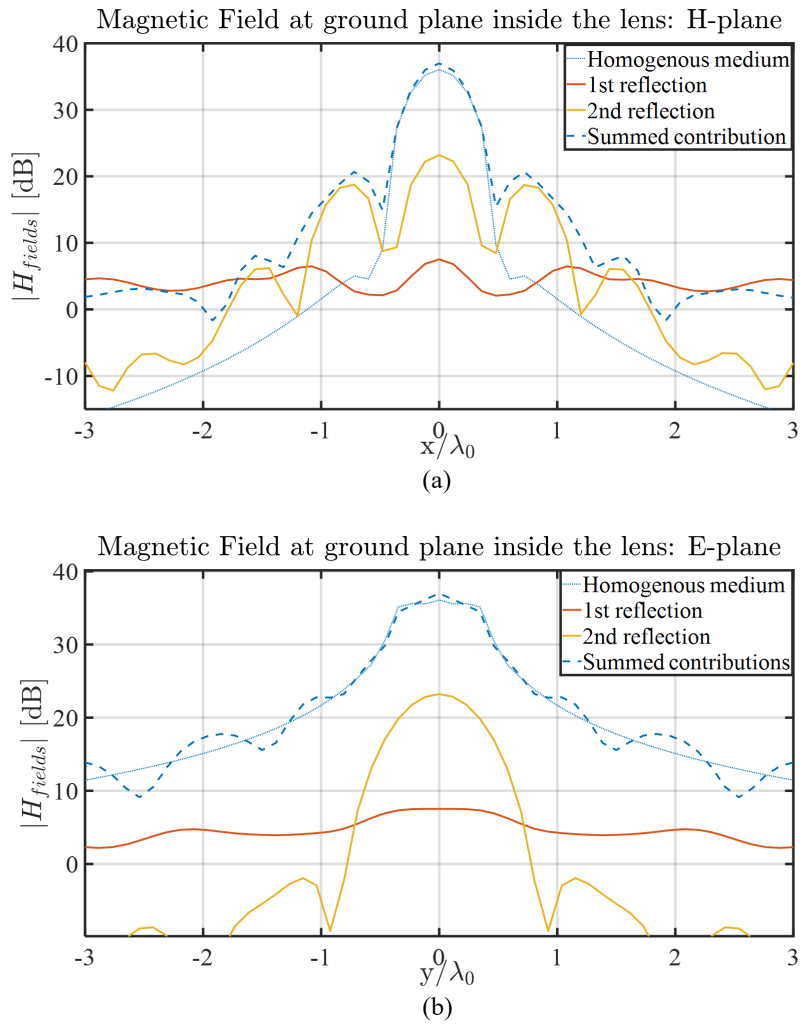


Figure 3.14: Magnetic fields from PO approximation at the ground plane in (a) H-plane and (b) E-plane

The total magnetic field from the GO-PO model is compared with the magnetic fields exported from CST MS in the region of interest. Figure 3.15 (a) and (b) compares the total magnetic field exported from CST MS simulation to that calculated using the GO-PO model in H- and E-plane, respectively. It can be observed from the graphs below that the magnetic field values obtained from the GO-PO model are comparable to the ones exported from CST MS simulation, especially in the region close to the focus of the lens. Along with the primary and secondary reflections, as shown in the GO-PO model, the CST MS simulation also accounts for additional reflections on the lens surface and diffraction effects at the lens edge. Thus resulting in differing magnetic field values near the lens edge.

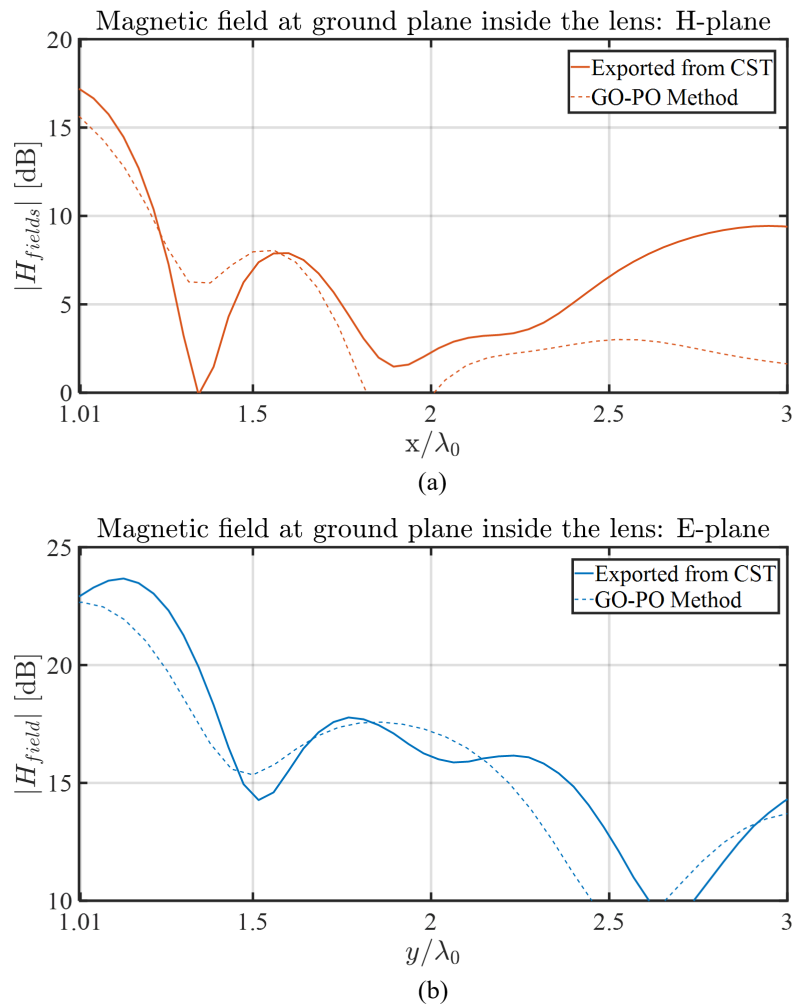


Figure 3.15: Comparison of Magnetic Fields obtained at the Ground Plane from CST & GO-PO Method in (a) H-plane and (b) E-plane

The mutual coupling between the two antennas placed under a lens is calculated using the magnetic fields obtained from the GO-PO model. This result is compared with the mutual coupling values calculated from the magnetic fields exported from CST MS simulator. Figure 3.16 (a) and (b) compares the results of the mutual coupling between two antennas under a lens, using the exported CST MS magnetic fields, as a function of their relative distance in H- and E-plane, respectively, to that of the GO-PO model.

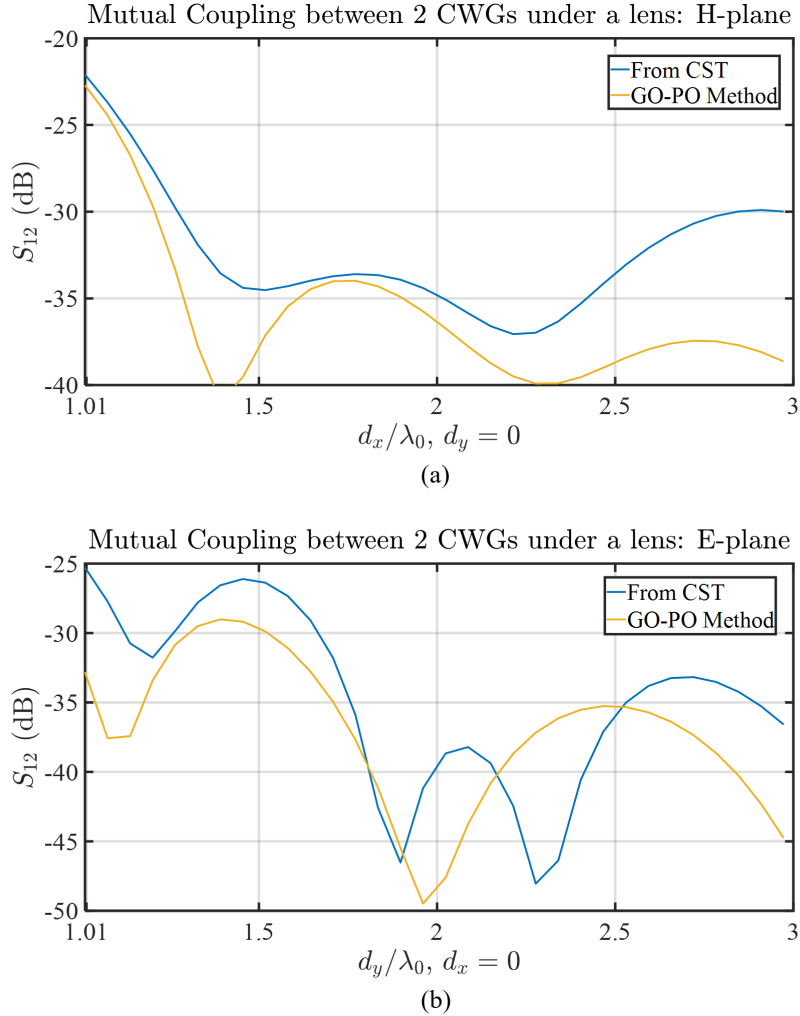


Figure 3.16: Mutual Coupling between two CWGs under a lens in (a) H-plane and (b) E-plane

It is clear from the graphs above that the mutual coupling value is significant when the second test source (\vec{M}_2) is close to the first test source (\vec{M}_1). The mutual coupling results using the GO-PO model are significantly better matched to the one from CST simulation results in the H-plane as compared to that in the E-plane. The reason for this can be explained using the far-field pattern of the CWG as shown in Figure 2.5. Despite having significantly low far-field value around 90° in the H-plane, the CWG field in the H-plane illuminates the lens surface more prominently because of a broader radiation pattern, thus both the first and second reflections become the major contributors to the mutual coupling. Whereas, in the E-plane due to a narrower radiation pattern and presence of nulls, the lens surface isn't as significantly illuminated and hence the second reflections have a lesser contribution to the mutual coupling. This is evident even from the magnetic field values on the ground plane from the second reflections as shown in Figures 3.14 (a) and (b). Since CST MS simulations account for additional reflections on the lens surface and edge diffraction effects [24], the mutual coupling values don't match exactly with the GO-PO model, especially in the E-plane. However, by using the proposed methodology the impact of the two major reflection phenomena are sufficiently well modeled, while the CST simulation proved to be much more time consuming, taking four hours for a complete simulation run, as well as having instability issues for low mutual coupling levels. In spite of the differences, the CST framework poses to validate the impact of the two reflections from the GO-PO model.

For the broadside scenario, it can be concluded that the mutual coupling between two test antennas is significant when the second test antenna is located close to the first test antenna due to the impact of second reflections that converge near the focus of the lens. The value of the mutual coupling reduces as the second test antenna is placed farther away from the first test antenna, since the impact on the mutual coupling between the two sources depends predominantly on the first reflections.

3.3.1.2. Off-axis transmitting test antenna

Similar to the CST MS framework above, here the equivalent currents of the CWG are imported to CST and are displaced to scan -1.5 beams (placed at $-1.5\lambda_d f_\#$ distance from the lens focus) in the H-plane and E-plane, as depicted in Figure 3.17 (a) and (b), respectively. The lens has a dielectric constant of $\epsilon_r = 2.5$ and $D_{lens} = 6\lambda_0$. Two CST simulations were performed: one for the case when the test antenna is displaced to -1.5 beams in the H-plane and the second for the case when it is displaced in the E-plane. The magnetic fields at the ground plane ($z \approx 0$) exported from CST MS were compared with the GO-PO model.

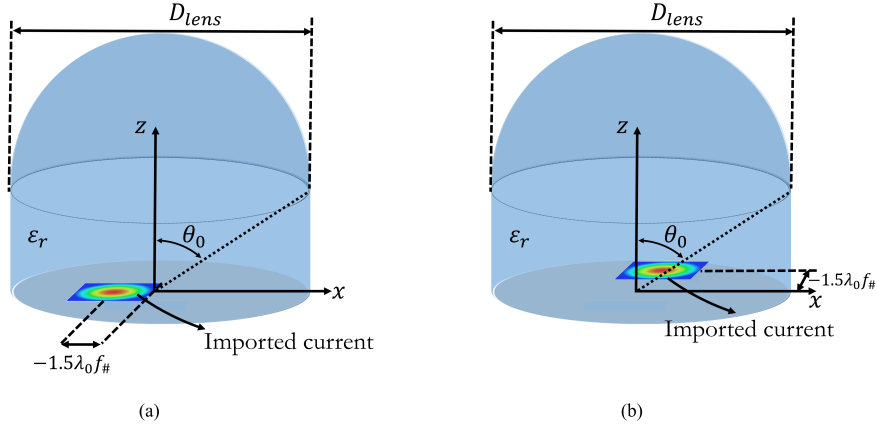


Figure 3.17: Equivalent currents of CWG imported to CST and displaced to -1.5 beams in the (a) H-plane, and (b) E-plane from the focus of a lens with dielectric constant $\epsilon_r = 2.5$ and lens diameter $D_{lens} = 6\lambda_0$

The ray-tracing picture for the relevant cases are as shown in Figure 3.18. For the case when the test CWG antenna is displaced to -1.5 beams in the H-plane, the GO fields on the lens surface for primary and secondary reflections are as shown in Figure 3.19 and Figure 3.20, respectively.

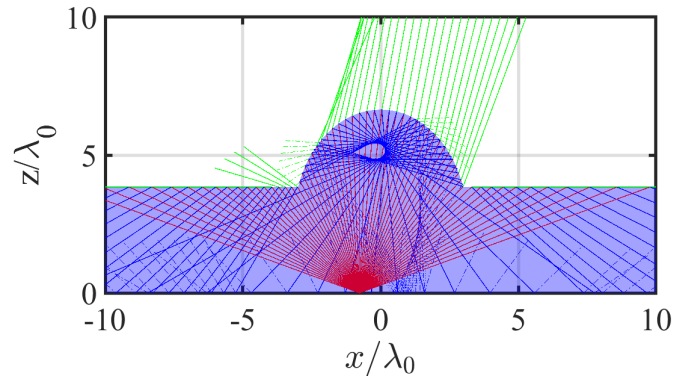


Figure 3.18: Ray-tracing for an antenna displaced to -1.5 beams from the focus of a lens with a dielectric constant of $\epsilon_r = 2.5$ and lens diameter $D_{lens} = 6\lambda_0$.

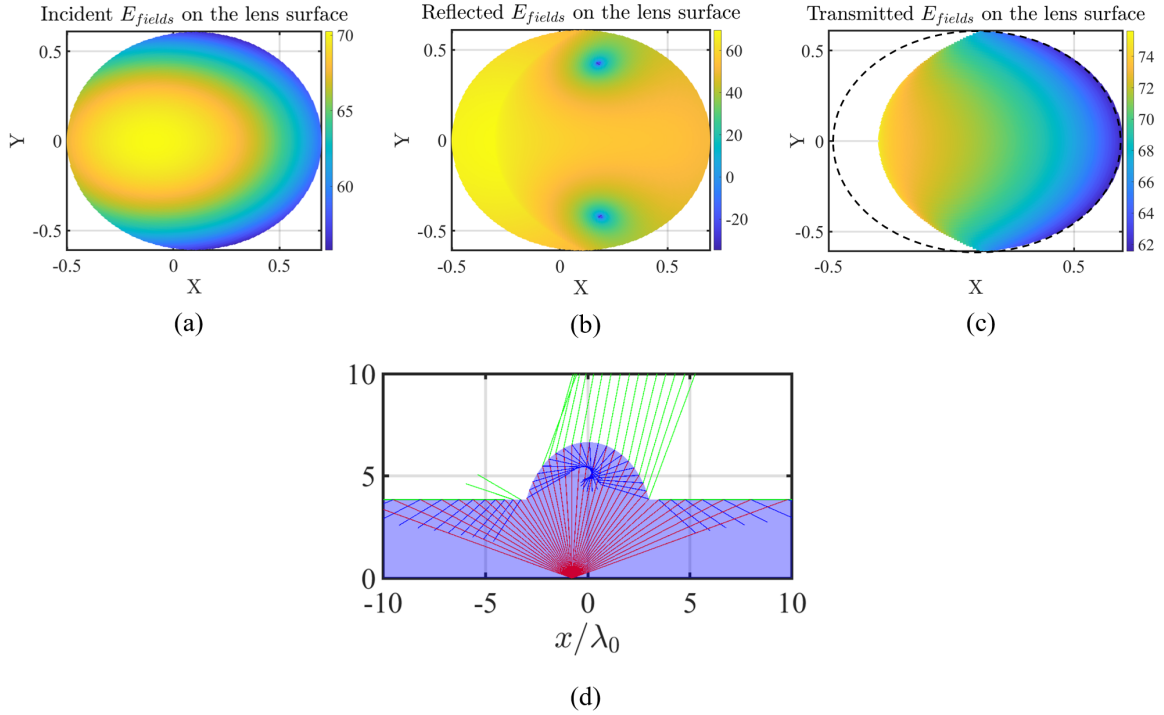


Figure 3.19: (a) Incident, (b) reflected, and (c) transmitted GO fields on the lens surface from first reflections when the CWG antenna is displaced to -1.5 beams in the H-plane as shown in the (d) ray-tracing picture.

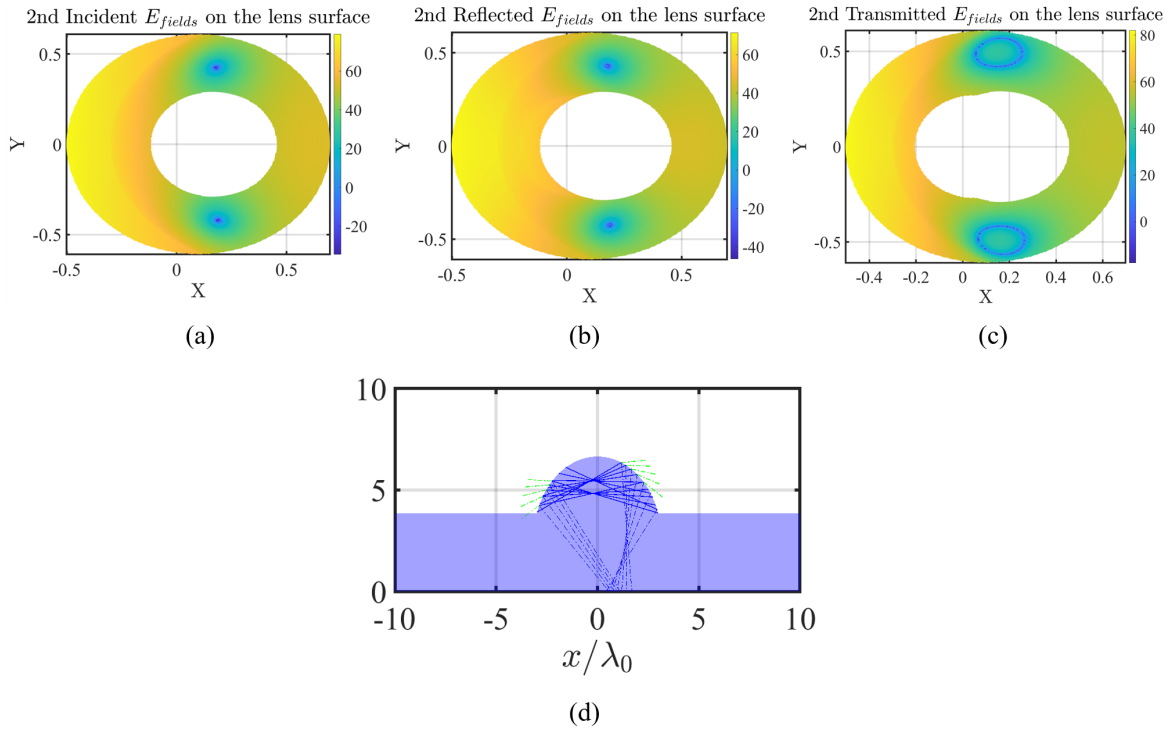


Figure 3.20: (a) Incident, (b) reflected, and (c) transmitted GO fields on the lens surface from second reflections when the CWG antenna is displaced to -1.5 beams in the H-plane as shown in the (d) ray-tracing picture.

If the rays hit the lens surface at a critical angle with the normal to the lens surface, total internal reflection occurs causing the EM fields hitting this region of the lens surface to completely reflect to the ground plane. This effect can be seen in Figure 3.19 (c) where only a section of the lens surface is transmitting the EM fields.

The mutual coupling between the two antennas in H-plane is calculated as a function of their relative

distance. In this case the first test feed (\vec{M}_1) is placed at -1.5 beams from the focus of the lens in the H-plane and the second test feed (\vec{M}_2) is displaced along this H-plane as depicted in Figure 3.21.

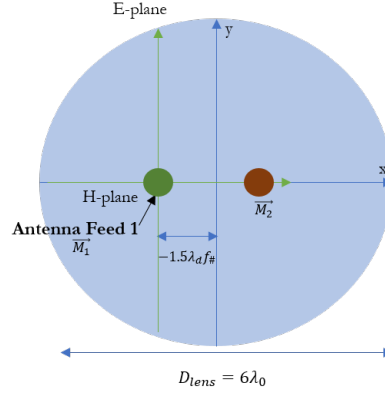


Figure 3.21: Location of the test feeds in the mutual coupling calculation for the displaced source in H-plane.

Using the GO fields, the magnetic fields are calculated on the ground plane under the lens using PO approximation. The magnetic field across the ground plane of the lens when the CWG antenna is displaced to $-1.5\lambda_d f_{\#}$ positions from the focus of the lens in the H-Plane is shown in Figure 3.22.

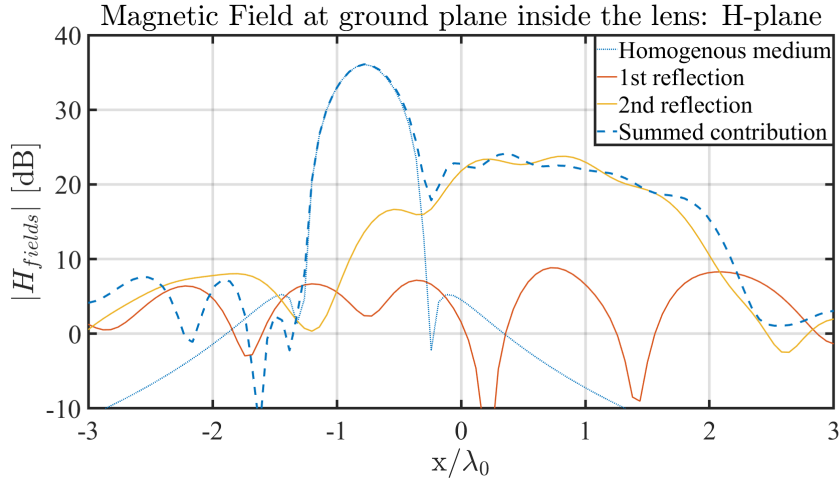


Figure 3.22: Magnetic fields from PO approximation at the ground plane in the H-plane when CWG is displaced to -1.5 beams in the H-plane.

From the above graph one can observe that the magnetic fields from the first reflection are spread across the ground plane under the lens (shown in red). On the other hand, the magnetic fields from the second reflections (shown in yellow) are significantly higher near the region that mirrors the source position (at $1.5\lambda_d f_{\#} = 0.77\lambda_0$). The total magnetic field at the ground plane from the GO-PO model (shown in blue dashed line) is compared with the magnetic fields exported from the CST at the region of interest in the H-plane.

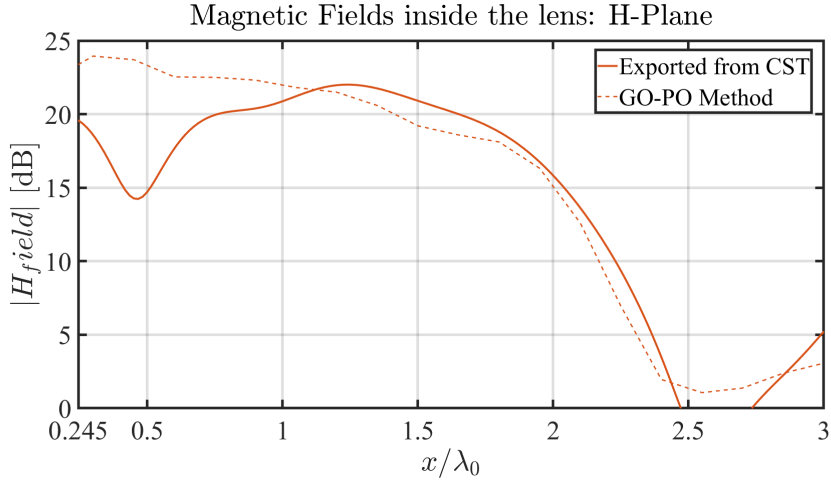


Figure 3.23: Comparison of magnetic fields obtained at the ground plane from CST & GO-PO method when the CWG is displaced to -1.5 beams in the H-plane.

From the graph above, it can be observed that the total magnetic field values from the GO-PO model, in the region of interest, are well matched with the magnetic fields exported from CST. The mutual coupling result is as shown in Figure 3.24.

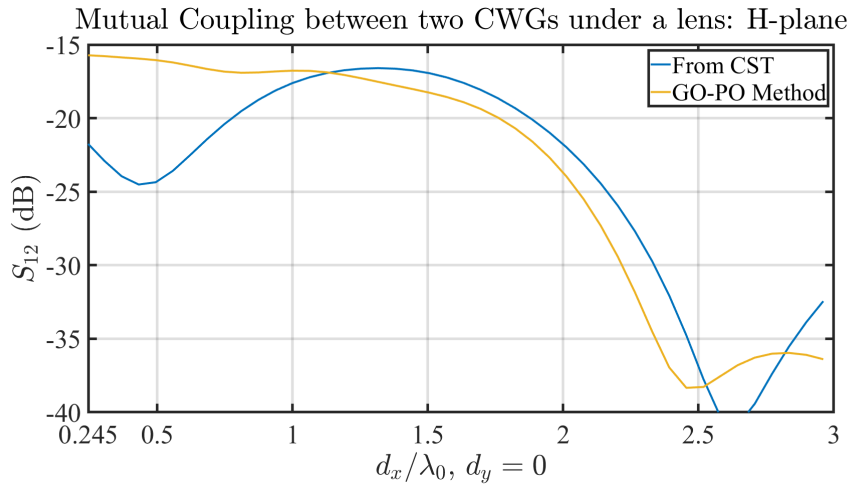


Figure 3.24: Mutual Coupling between two CWGs under a lens in H-Plane when the first test feed is displaced to -1.5 beams in the H-plane from the focus of the lens.

The mutual coupling between the two feeds shows a significant rise around the mirror region of the antenna (near 1.5 beams = $0.77\lambda_0$). This is predominantly due to the second reflections that impinge on this area as shown in the ray-tracing picture in Figure 3.18 by the blue dashed-dotted lines. The results from the GO-PO method are well matched with the CST MS fullwave simulation results.

Similarly, for the case when the first test feed is displaced to -1.5 beams in the E-plane, the magnetic fields from the GO-PO model is as shown in Figure 3.25. The magnetic field pattern from the first reflections (shown in red) in the E-plane is the same as the one in the case of the H-plane displacements as shown in Figure 3.22. However, the magnetic fields from the second reflections are not as dominating as the one in the case of displacement in the H-plane. This is due to the fact that the far-field radiation pattern of the CWG in the E-plane is more directive in comparison to the one in the H-plane. This basically translates to the fact that the plane in which the direct coupling is weak, the mutual coupling is dominated by the lens reflections [19]. The total magnetic field from the model is compared with the magnetic fields exported from CST MS fullwave simulator as shown in Figure 3.26.

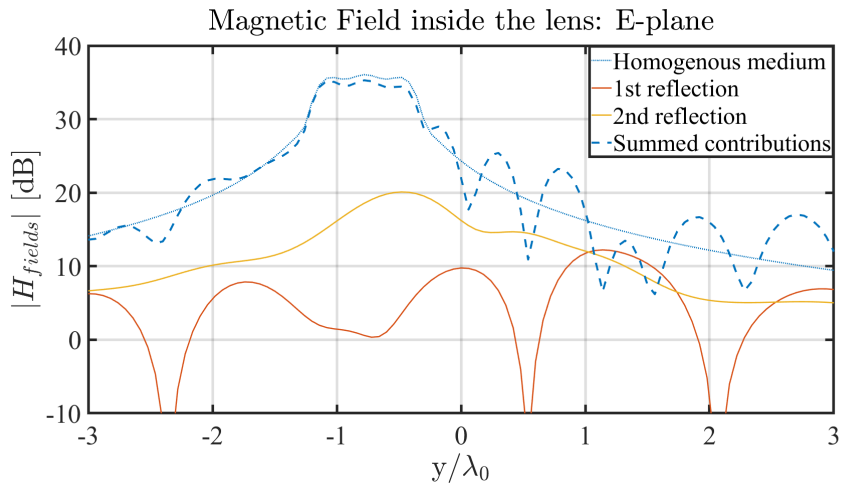


Figure 3.25: Magnetic fields from the PO approximation at the ground plane in the E-plane when the CWG is displaced to -1.5 beams in the E-plane.

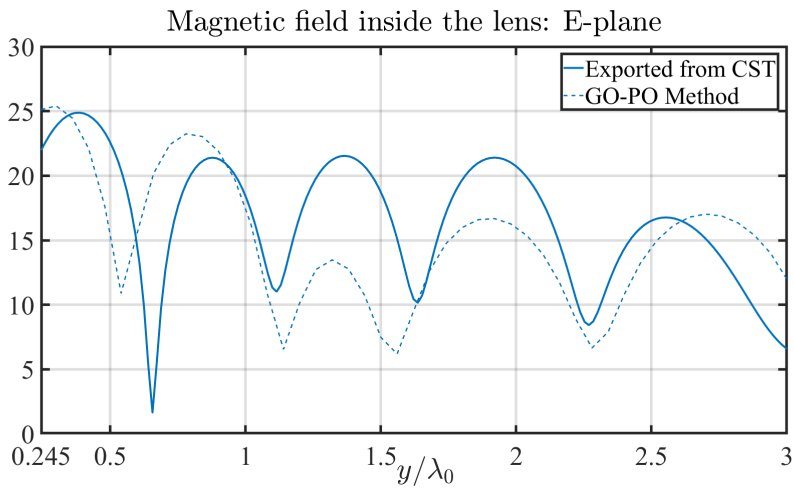


Figure 3.26: Comparison of the magnetic fields obtained at the ground plane from CST & GO-PO method when the CWG is displaced to -1.5 beams in the E-plane.

The mutual coupling between the two feeds under the lens, as a function of their relative distances is shown in Figure 3.27 for when the first test feed is displaced to -1.5 beams in the E-plane. The results are well matched until a distance of $1\lambda_0$. The subsequent disagreement between the results arises due to the total reflection regions and the edge diffraction that is accounted for in the CST MS simulation and not in the GO-PO model.

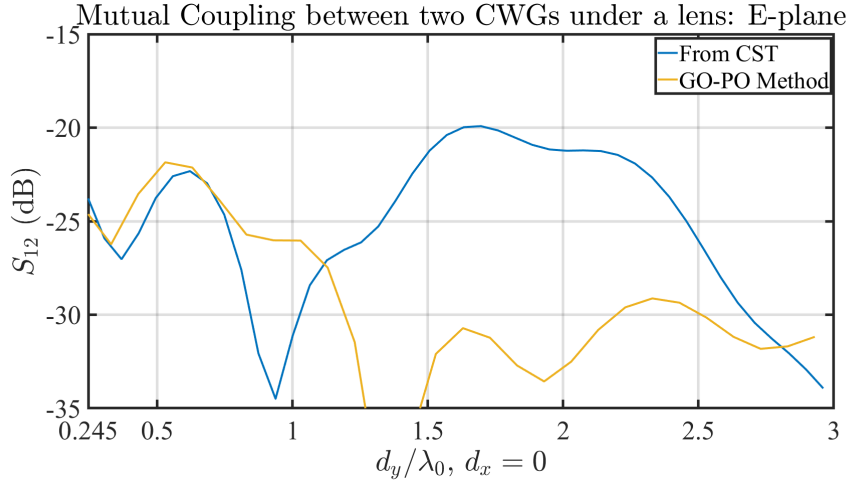


Figure 3.27: Mutual Coupling between two CWGs under a lens in the E-Plane when the first test feed is displaced to -1.5 beams from the focus of the lens in E-plane.

3.3.2. Large plastic lens case: $D_{lens} = 15\lambda_0$

To validate the model for a large plastic lens and other types of antenna elements, a Gaussian feed with an edge taper of -14dB at 38° is considered, whose current distribution is calculated using equation 3.22. The current distribution and far-field radiation pattern of the feed is shown in Figure Figure 3.28 (a) and (b).

$$F(u, v) = e^{\left[-\left(\frac{u}{u_0}\right)^2 - \left(\frac{v}{v_0}\right)^2\right]} \quad (3.22)$$

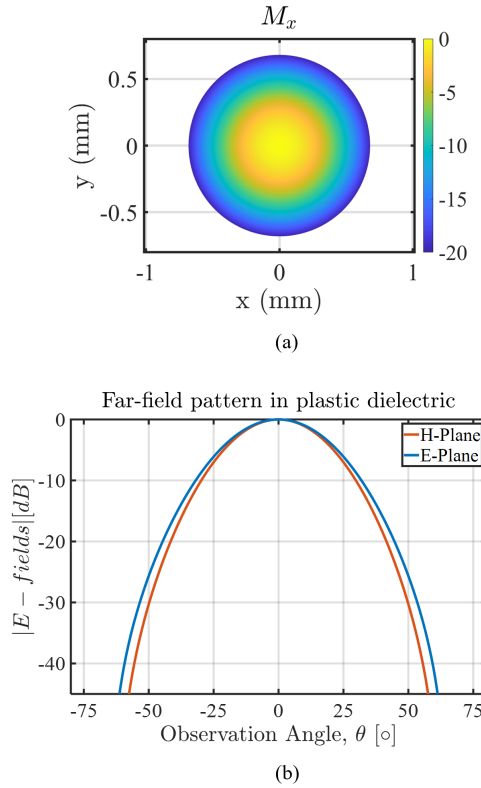


Figure 3.28: (a) A Gaussian feed current distribution and (b) its far-field radiation pattern in plastic ($\epsilon_r = 2.5$) homogeneous medium.

The GO-PO model for calculating the mutual coupling between two antennas placed under this lens is compared with the mutual coupling values obtained from the magnetic fields exported from a CST MS full-wave simulation. The specifications of the feed and lens are as described below:

- Source type = Gaussian feed
- Source diameter, $D_f = 2.15\lambda_d$
- Lens diameter, $D_{lens} = 15\lambda_0$
- Lens material, $\epsilon_r = 2.5$, plastic
- Lens f-number, $f_{\#} = 0.812$ ($\theta_0 = 38^\circ$)

The model is validated using the CST framework for two scenarios:

- On-axis antenna: Test feed \vec{M}_1 placed at focus of the lens
- Off-axis antenna: Test feed \vec{M}_1 is displaced to $-2\lambda_d f_{\#}$ position from the focus of the lens which corresponds to scanning 2 beams using the lens

3.3.2.1. On-axis transmitting test antenna

The equivalent currents of the Gaussian antenna are imported to CST MS fullwave simulator from MATLAB. The antenna is placed at the focus of the truncated plastic lens. The magnetic fields obtained at the ground plane ($z \approx 0$) of the lens from the CST MS simulation is exported to MATLAB for calculating the mutual coupling between the two Gaussian antennas under a lens as a function of their relative distance. These magnetic fields and mutual coupling values are compared with the GO-PO model.

The ray tracing for the lens of diameter, $D_{lens} = 15\lambda_0$ when the Gaussian antenna is placed at the focus of the lens is as depicted in Figure 3.29 across the H-plane.

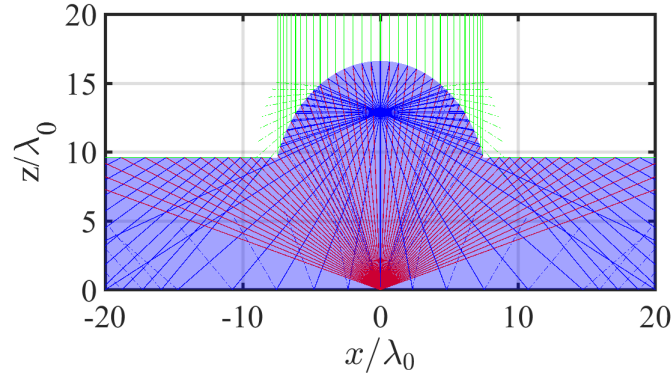


Figure 3.29: Ray-tracing for an antenna placed at the focus of a lens with a dielectric constant of $\epsilon_r = 2.5$ and lens diameter, $D_{lens} = 15\lambda_0$.

The far-field of the Gaussian antenna is calculated and is imported to the GO-PO model to compute the scattered GO fields on the lens surface. Using the incident and reflected GO fields, the magnetic fields are calculated at the ground plane under the lens surface using the PO approximation for the primary and the secondary reflections, as shown in Figure 3.30 (a) and (b) for H- and E- Plane, respectively. The magnetic fields from primary (1^{st}) reflections are uniformly spread across the ground plane, whereas the magnetic fields from secondary (2^{nd}) reflections have a higher value near the focus of the lens and taper down as it progresses away from the focus.

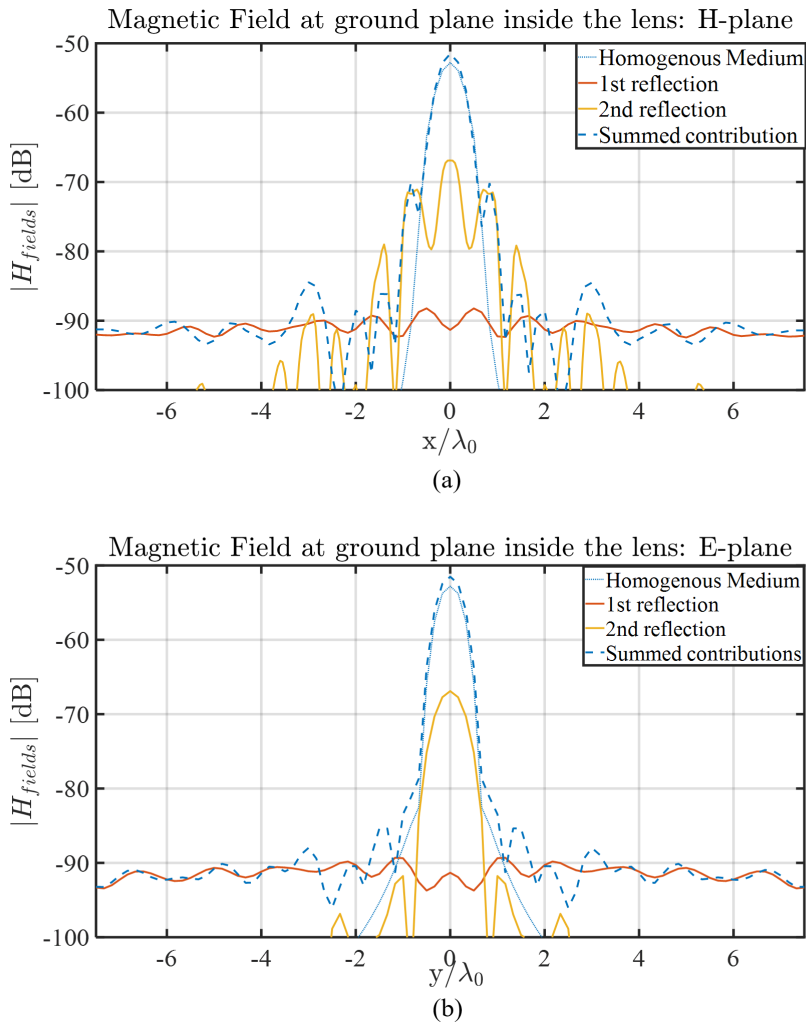


Figure 3.30: Magnetic fields from the PO approximation at the ground plane in the (a) H-plane and (b) E-plane.

The total magnetic field obtained at the ground plane from the GO-PO method is used to compute the mutual coupling. The mutual coupling between two Gaussian antennas under a lens as a function of their relative distance is shown in Figure 3.31 and Figure 3.32 in the H- and the E-plane, respectively. The mutual coupling results obtained from the GO-PO model is comparable to the CST MS simulation results.

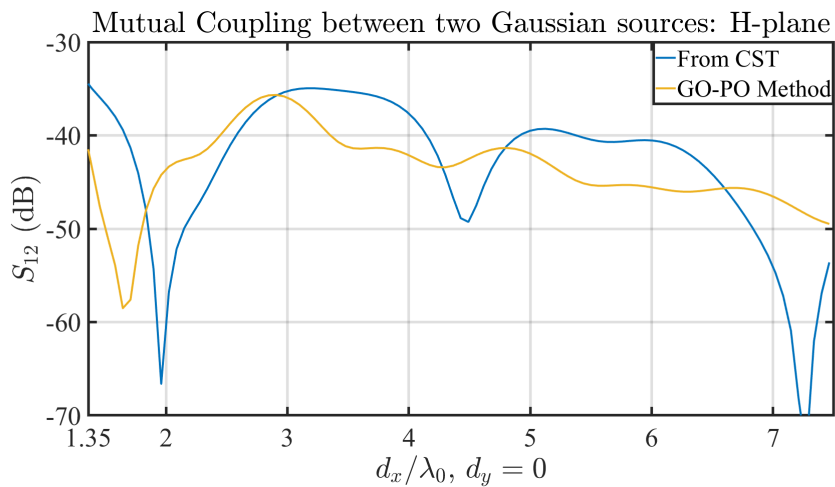


Figure 3.31: Mutual Coupling between the two Gaussian antennas under a lens in the H-plane.

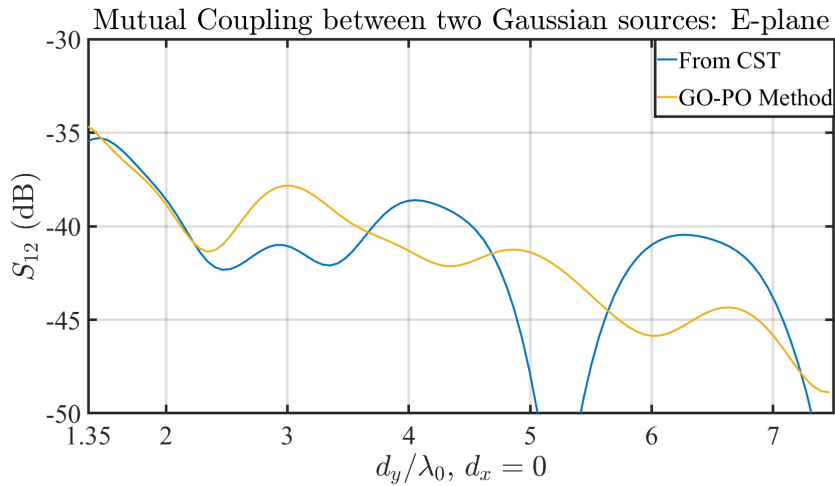


Figure 3.32: Mutual Coupling between the two Gaussian antennas under a lens in the E-plane.

3.3.2.2. Off-axis transmitting test antenna

In this case, the first test Gaussian antenna is displaced to -2 beams ($-2\lambda_d f\#$). The ray tracing analysis for this case is shown in Figure 3.33. It can be seen that the first reflections curve around the second focus of the elliptical lens and the second reflections (shown in dashed dotted lines) intersect the ground plane near a mirror region to the antenna location.

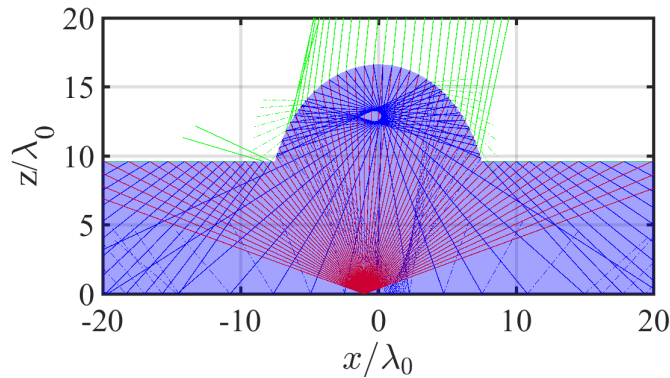


Figure 3.33: Ray-tracing picture for an antenna displaced to -2 beams from the focus of a lens with a dielectric constant of $\epsilon_r = 2.5$ and lens diameter, $D_{lens} = 15\lambda_0$.

The total magnetic field on the ground plane under the lens for when the test antenna is displaced to -2 beams in the H- and the E-plane is shown in Figure 3.34 and Figure 3.35, respectively. The total magnetic fields calculated using the GO-PO method is comparable to the exported CST MS simulation magnetic fields in both planes.

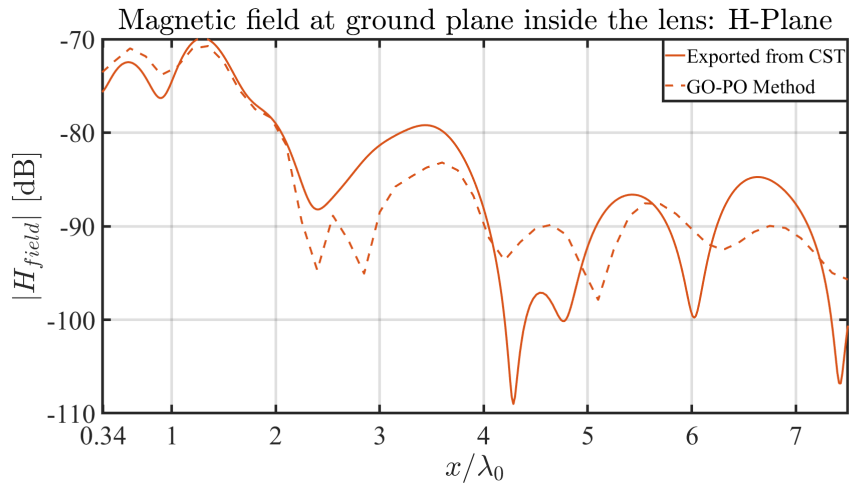


Figure 3.34: Comparison of Magnetic Fields obtained at the Ground Plane in H-plane from CST & GO-PO Method when the test antenna is displaced to -2 beams in H-plane.

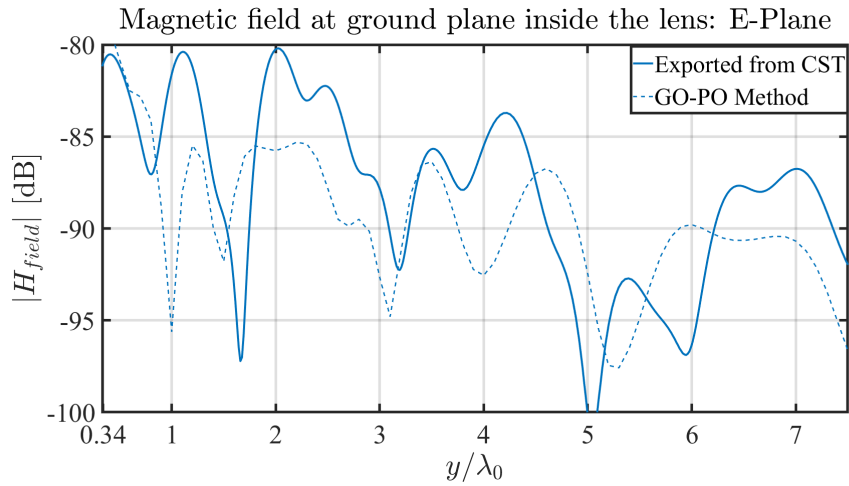


Figure 3.35: Comparison of magnetic fields obtained at the ground plane in E-plane from CST & GO-PO method when the test antenna is displaced to -2 beams in the E-plane.

The mutual coupling between the two Gaussian antennas as a function of their relative distance is calculated for both cases and compared with the results obtained from the CST MS framework as shown in Figure 3.36 and Figure 3.37. The mutual coupling between the two antennas is highest when the second antenna is placed at the mirror region ($2\lambda_d f_{\#} = 1.027\lambda_0$) with respect to the first test antenna due to the impact of the secondary reflections. This is especially evident in the H-plane displacement case.

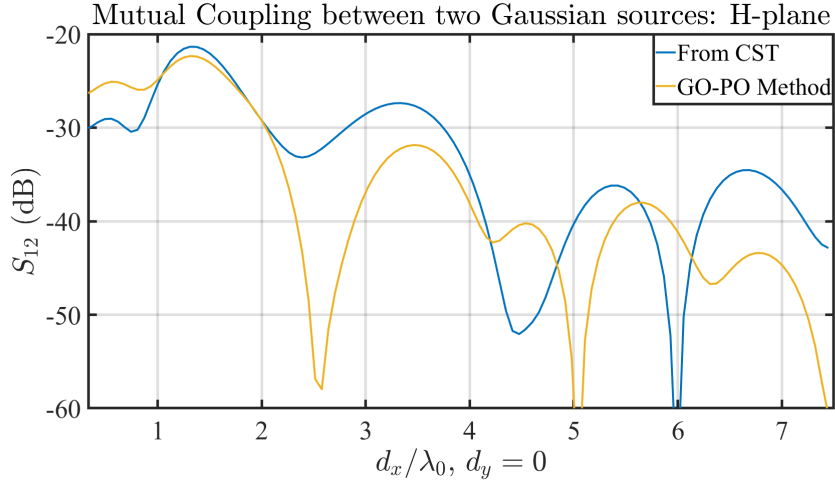


Figure 3.36: Mutual Coupling between two Gaussian antennas under a lens in the H-Plane when the first test antenna is displaced to -2 beams from the focus of the lens in H-plane.

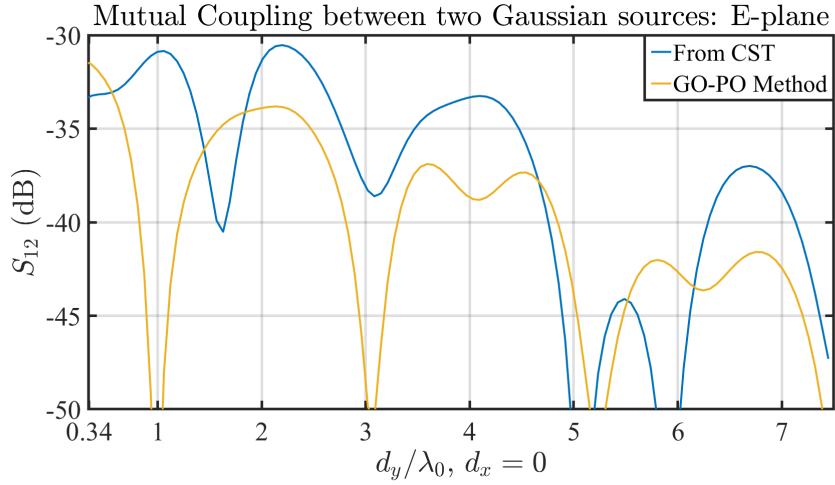


Figure 3.37: Mutual Coupling between two Gaussian antennas under a lens in E-Plane when the first test antenna is displaced to -2 beams from the focus of the lens in E-plane.

In conclusion, the GO-PO model for calculating the mutual coupling between two antennas placed under a lens is validated using the CST MS fullwave simulator, where the results obtained from the model is comparable to that obtained from CST simulations.

Since the magnitude of the magnetic field values exported at the ground plane of the lens surface from CST MS simulations are low, the CST simulations required a significantly fine mesh for both lenses ($D_{lens} = 6\lambda_0$ and $D_{lens} = 15\lambda_0$). Thus each CST simulation performed in this section were numerically cumbersome and time consuming. Whereas the GO-PO approximation model takes a quarter of the duration to run, while giving comparable mutual coupling results. To reduce the elapsed time further for developing a rapid design tool, reciprocity is employed in the GO-PO model. This method is explained in Section 3.4.

3.4. Bi-Directional Ray-Tracing via Reciprocity

In order to calculate the mutual coupling between the two feeds, the open circuit voltage ($V_{oc}I_0$) is calculated, as in Equation 2.2 where the magnetic field \vec{H}_1 from the lens surface is calculated at the ground plane using Equation 3.21. Due to the presence of two integration calculations, one for the Green's function integral to calculate the magnetic field at the ground plane and the second for the calculation of open circuit voltage, the code becomes computationally intensive, thus increasing the code run duration. In order to have a single integration and reduce the run-time of the code, the Green's function integral is replaced with the concept

from Reciprocity theorem to calculate the open circuit voltage using the fields on the lens surface, similar to [18].

The Reciprocity theorem states that the response of a system to a source is unchanged when the source and the observer are interchanged [32]. Here reciprocity is employed to equate the following two open circuit voltages:

$$V_{oc}I_0 = \int \vec{H}_1 \cdot \vec{M}_2 dS \equiv V_{oc}I_{0,lens} = \int (\vec{J}_s \vec{E}_2 - \vec{M}_s \vec{H}_2) \quad (3.23)$$

where, \vec{H}_1 is the magnetic field radiated by the equivalent currents on the lens surface, \vec{J}_s and \vec{M}_s , and evaluated on the ground plane; \vec{E}_2 and \vec{H}_2 are the EM fields radiated by the currents of the second test antenna, \vec{M}_2 , and evaluated on the lens surface.

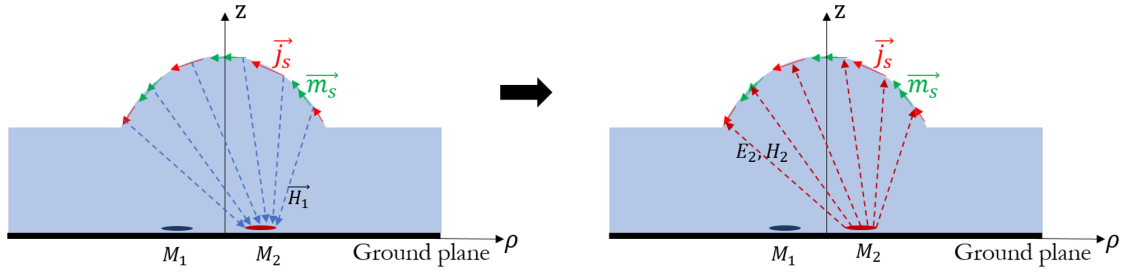


Figure 3.38: Reciprocity method for calculating the mutual coupling between the antennas \vec{M}_1 and \vec{M}_2 .

The electric (\vec{E}_2) and magnetic (\vec{H}_2) fields from the second test antenna (\vec{M}_2) can be evaluated on the lens surface using the GO approximation method for the incident fields as described in Section 3.2. Hence in this case, the Green's function integral for calculating the magnetic fields at the ground plane is replaced by one time integral calculation of the electric and magnetic field radiated by the second test antenna. The total open circuit voltage will be a summation of the lens and the homogeneous medium contributions as before. The results obtained for the mutual coupling between two antennas placed under a lens using the reciprocity theorem is compared with the previous method in Section 3.4.1.

3.4.1. Results and Validation

In order to validate the reciprocity method, a Gaussian feed as defined in Section 3.3, is placed at the focus of a truncated elliptical lens with a dielectric constant of $\epsilon_r = 2.5$ and lens diameter of $D_{lens} = 15\lambda_0$. The mutual coupling between the two antennas is shown in Figure 3.39 (a) and (b) for H- and E-plane, respectively. Similarly, the mutual coupling between the two antennas is calculated for the case when the Gaussian feed is shifted to -2 beams in the H-plane, as shown in Figure 3.40. It can be observed that the mutual coupling results obtained using the reciprocity method are the same as the ones obtained in Section 3.3, while the former is four times faster in generating these results.

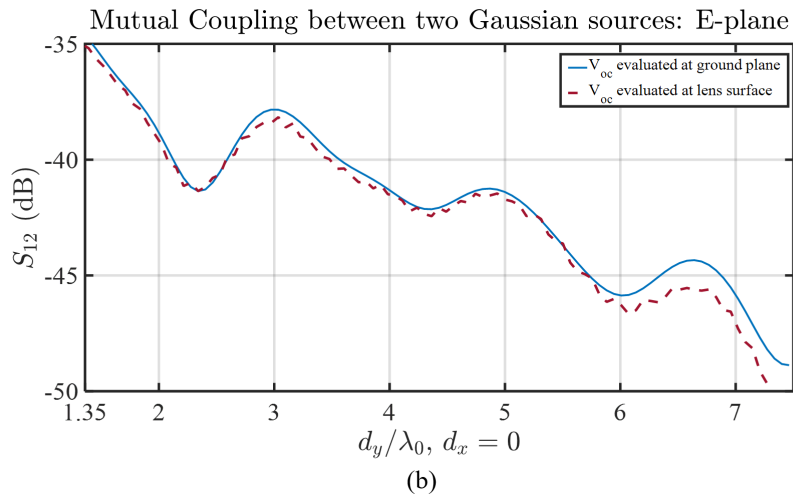
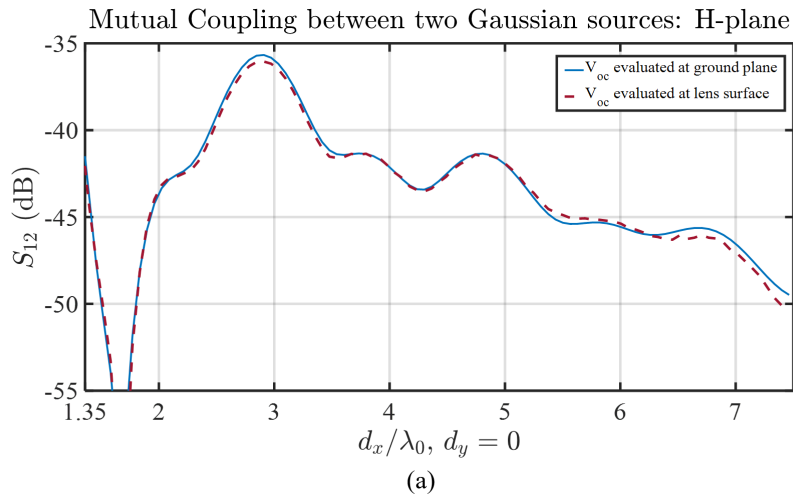


Figure 3.39: Mutual Coupling between two Gaussian antennas under a lens in the (a) H-Plane and (b) E-Plane, when the first test antenna is at the focus of the lens.

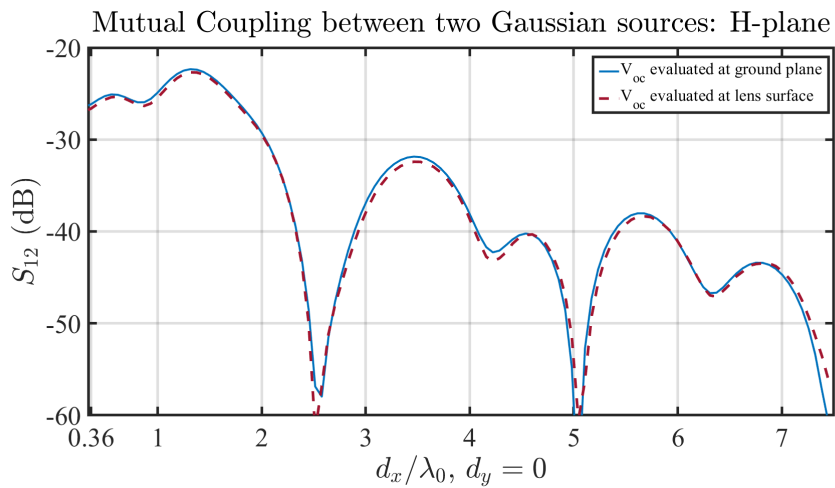


Figure 3.40: Mutual Coupling between two Gaussian antennas under a lens in the H-Plane when the first test antenna is displaced to -2 beams from the focus of the lens.

In conclusion, the GO-PO model for evaluating the mutual coupling between two feeds placed under a single lens is in fair agreement with the CST MS simulation framework up to the second reflection contributions. This model thus can form the basis to study different lens antenna scenarios in terms of the mutual

coupling. Chapter 4 and 5 delves into studying the impact of lens diameter, feed location and lens edge illumination on the mutual coupling results for plastic and silicon lens, respectively.

4

Case Study: Plastic Lens

In this chapter, plastic lenses with a dielectric constant of $\epsilon_r = 2.5$ are studied to understand their impact on the mutual coupling between two antennas. For this study, two different lens diameters are considered - $D_{lens} = 6\lambda_0$ and $D_{lens} = 15\lambda_0$. In addition, three different types of antennas are placed under the lenses of different $f_{\#}$ to understand the impact of lens edge illumination on the mutual coupling.

4.1. Geometry of the considered plastic lenses

For elliptical lenses, the eccentricity ($e = \frac{1}{\sqrt{\epsilon_r}}$) of the ellipse controls the curvature of the lens which is dependant on the lens material. In the case of plastic lenses ($\epsilon_r = 2.5$), the eccentricity value is close to 1 thus making the truncated lenses extremely curved. As explained in section 3.1 and shown in the ray tracing picture in Figure 4.1, part of the incident rays originating from a feed placed at the lower focus (f_1), illuminates the lens surface, reflects and crosses the upper (f_2) focus of the ellipse. Some of these reflected rays intersect with the lens surface again to create secondary reflected rays that trace a path back to f_1 [19]. The portion of incident rays that are launched within the solid angle, Ω (highlighted in orange), do not contribute to this secondary reflections. These rays experience secondary reflections at the ground plane and contribute to the mutual coupling caused by the first reflections. It is the reflected rays that originate from the edges of the lens, outside the solid angle, that cause the secondary reflections. For the case of plastic lenses ($\epsilon_r = 2.5$), due to the lens eccentricity, this solid angle is narrow which causes the secondary reflections on the lens surface to dominate the mutual coupling behaviour.

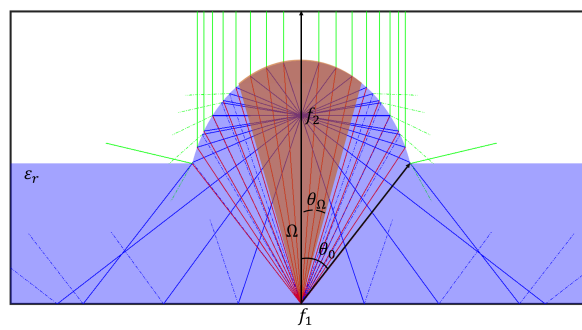


Figure 4.1: Ray tracing picture of a feed placed at the focus of an elliptical lens with $\epsilon_r = 2.5$ and $D_{lens} = 15\lambda_0$. The solid angle, Ω , is highlighted in orange. The incident, reflected and transmitted rays are indicated with red, blue, and green colours, respectively.

In order to understand the impact of lens material on the solid angle region, Figure 4.2 shows a plot of θ_{Ω} with respect to the lens dielectric for un-truncated lenses when the feed is placed at the focus of the lens. Here, θ_{Ω} depicts the solid angle cut in the $\phi = 0$ direction as highlighted in Figure 4.1. As the permittivity of the lens material is increased, the region where only first reflections occur increases. Thus the impact on the mutual coupling levels from the secondary reflections will decrease. This can be observed evidently even with the ray-tracing pictures shown in the inset for plastic ($\epsilon_r = 2.5$) and silicon ($\epsilon_r = 11.9$) lens cases.

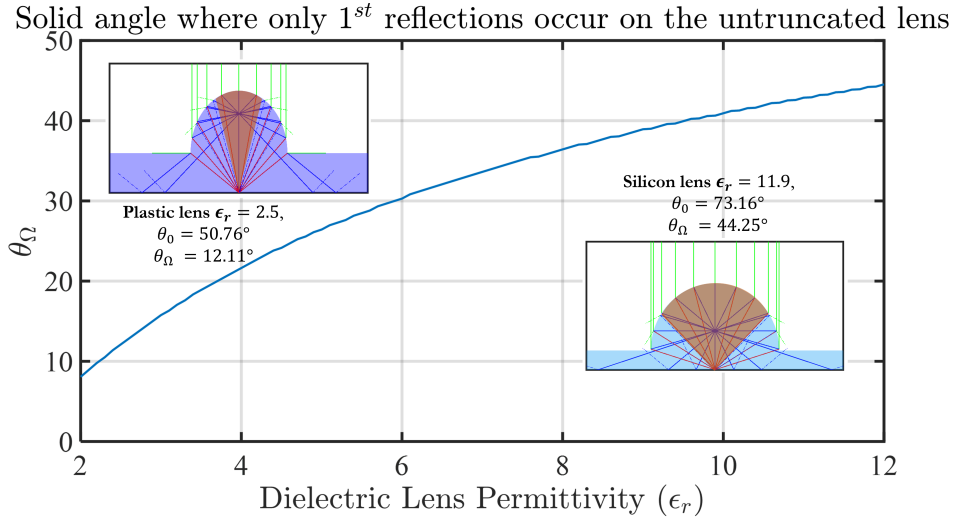


Figure 4.2: Impact of lens permittivity (ϵ_r) on the solid angle where only primary (1^{st}) reflections occur on the un-truncated lens surface when the feed is placed at the focus of the lens. Shown in this Figure is θ_Ω that depicts the solid angle cut in the $\phi = 0$ direction.

To explore the directivity effect of a lens surface on its secondary reflections, here the mutual coupling between two feeds when placed under a smaller plastic lens ($D_{lens} = 6\lambda_0$) is compared to the case of a larger lens ($D_{lens} = 15\lambda_0$). Since the second reflections occur close to the lens edges the type of feed placed under these lenses and the corresponding lens edge illumination are also considered as variables in this study. These feeds are described in Section 4.2.

4.2. Considered plastic lens antenna feeds

The impact of lens illumination on the mutual coupling results is studied here for different antenna feeds having varying radiation patterns. The following three types of feeds were considered for the study:

- Source 1: A Gaussian feed with an edge taper of -14 dB at 38° as defined in Section 3.3.2, whose far-field radiation pattern is shown in Figure 3.28 (b)
- Source 2: A CWG feed with an edge taper of -9 dB in the H-plane and -14 dB in the E-plane at 38° , as defined in Section 2.1.2, whose far-field radiation pattern is shown in Figure 2.5
- Source 3: A Gaussian feed with an edge taper of -13 dB at 30° whose far-field radiation pattern is shown in Figure 4.3

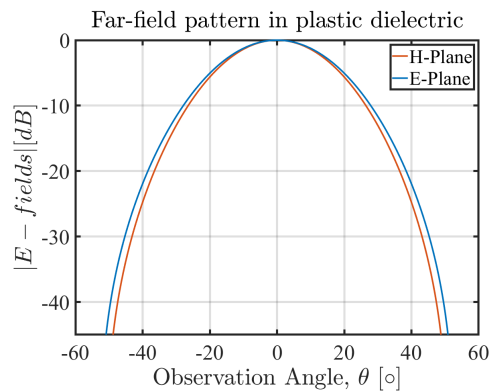


Figure 4.3: Far-field radiation pattern of a Gaussian feed with an edge taper of -13dB at 30° in plastic ($\epsilon_r = 2.5$) homogeneous medium.

The far-field radiation patterns of these fields are calculated inside a homogeneous medium of plastic with a dielectric constant of $\epsilon_r = 2.5$. The edge taper of the far-field radiation pattern of the feeds governs how effectively the surface area of the lens will be illuminated by the EM fields.

The mutual coupling between two feeds under a plastic lens was studied using the test cases tabulated below. The $f_{\#}$ and Feed type used determines the lens edge illumination. The inferences have been documented in Section 4.3

	Lens Diameter	$f_{\#}$	Feed Type	Edge Taper (E/H Plane)	Feed Location	Broadside Directivity	Broadside Radiation Efficiency
Case 1	$15\lambda_0$	0.812	Source 1: Gaussian Feed	-14 dB	On-axis Off-axis: -2 Beams, -4 Beams	33.11 dB	0.906
Case 2	$6\lambda_0$	0.812	Source 1: Gaussian Feed	-14 dB	On-axis Off-axis: -1.5 Beams	25.23 dB	0.906
Case 3	$15\lambda_0$	0.812	Source 2: CWG	-9 dB / -14 dB	On-axis Off-axis: -2 Beams, -4 Beams	33.28 dB	0.80
Case 4	$15\lambda_0$	1	Source 3: Gaussian Feed	-13 dB	On-axis Off-axis: -2 Beams, -4 Beams	33.15 dB	0.89

Table 4.1: Plastic Lens Case Study

4.3. Results and Inferences

4.3.1. Impact of lens diameter

Consider the case where Source 1 is placed at the focus of the plastic lens of $D_{lens} = 15\lambda_0$ having an $f_{\#} = 0.812$ (truncation angle = 38°). The broadside far-field radiation pattern of this lens antenna is shown in Figure 4.4. This pattern is symmetric in both planes with side lobe levels of about -20dB. The lens antenna has a radiation efficiency of $\eta_r = \frac{P_{rad}^{lens}}{P_{rad}^{feed}} = 0.906$, where P_{rad}^{lens} is the power radiated to air from the lens surface and P_{rad}^{feed} is the power radiated by the feed antenna into the homogeneous medium of lens.

When the Gaussian feed is placed off-axis, the radiation pattern and efficiency of the lens antenna changes. Figure 4.5 shows the far-field radiation patterns of the lens antenna for the Gaussian feed displaced to -2 beams ($-2\lambda_d f_{\#}$) in the H- and E-plane. The radiation efficiency of this lens antenna is $\eta_r = 0.86$. Similarly, the radiation efficiency of the lens antenna when the Gaussian feed is displaced to -4 beams ($-4\lambda_d f_{\#}$) in the H- and E-plane is $\eta_r = 0.73$ and Figure 4.6 depicts its far-field pattern.

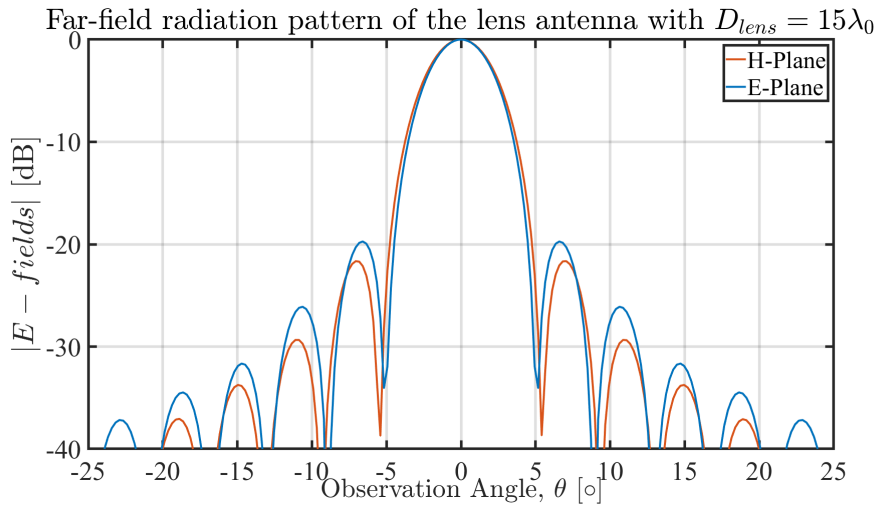


Figure 4.4: Far-field radiation pattern of the lens antenna when the Gaussian feed (Source 1) is placed at the focus of a plastic lens of $D_{lens} = 15\lambda_0$.

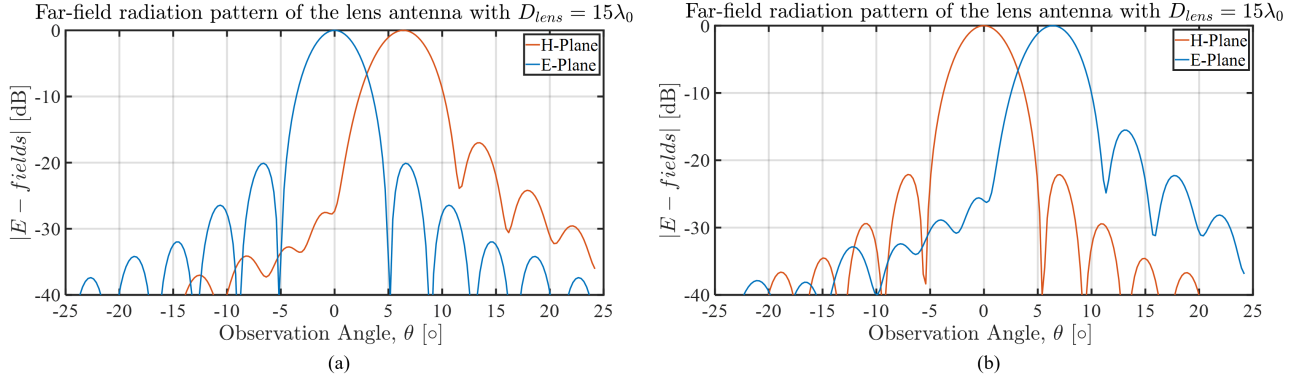


Figure 4.5: Far-field radiation pattern of the lens antenna when the Gaussian feed (Source 1) is displaced to -2 beams from the focus in (a) H-plane and (b) E-plane of a plastic lens of $D_{lens} = 15\lambda_0$.

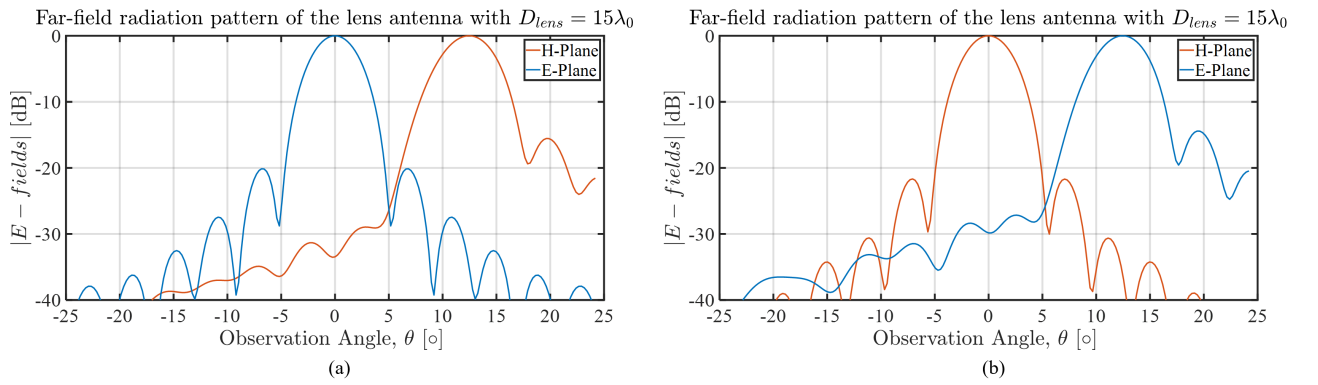


Figure 4.6: Far-field radiation pattern of the lens antenna when the Gaussian feed (Source 1) is displaced to -4 beams from the focus in (a) H-plane and (b) E-plane of a plastic lens of $D_{lens} = 15\lambda_0$.

Figure 4.7 compares the ray-tracing pictures for the on- and off-axis feed cases whose far-field shown above. Considering the case where Source 1 is placed at the focus of the lens and then displaced to -2 beams and -4 beams ($-4\lambda_d f_{\#}$) in the H- and the E-plane, the mutual coupling results obtained are as shown in Figure 4.8. From Figure 4.8 (a) it can be observed more distinctly in the H-plane results that the mutual coupling value becomes significantly higher when the source is displaced. This is due to the fact that the second reflections get re-focused to the mirror position of the source location as shown in the ray-tracing pictures in Figure 4.7 (b) and (c) for -2 beams and -4 beams displacement scenarios, respectively. For the case of broadside, the mutual coupling pattern is more uniformly spread across the area of interest since the impact of the secondary reflections are concentrated at the focus (where the feed is present). Therefore, for a transmitting antenna at focus, the primary (first) reflections from the lens surface are the contributors towards the mutual coupling between two feeds.

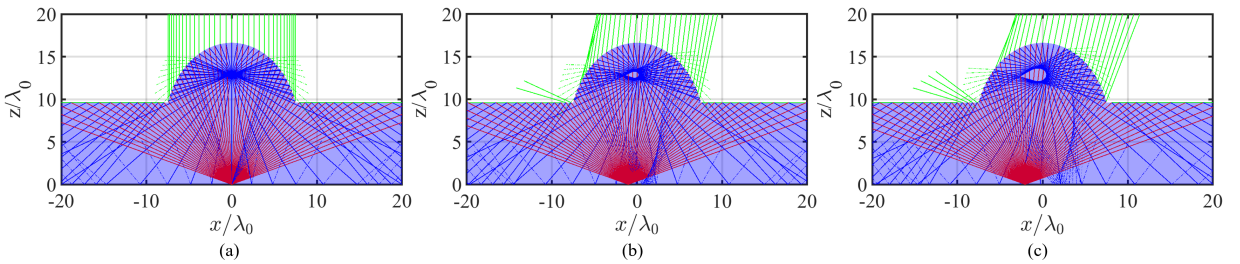


Figure 4.7: Ray tracing picture of a feed (a) placed at focus, (b) displaced to -2 beams, and (c) displaced to -4 beams from the focus of a plastic lens with $D_{lens} = 15\lambda_0$. The incident, reflected and transmitted rays are indicated with red, blue, and green colours, respectively.

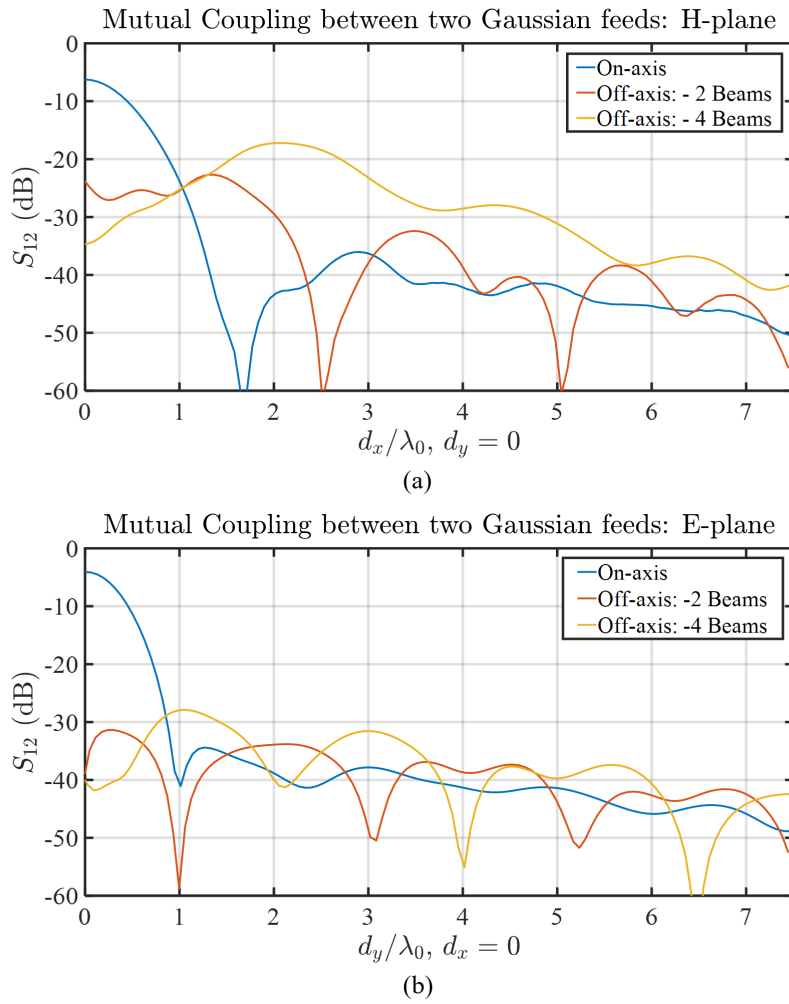


Figure 4.8: Mutual coupling between two Gaussian feeds when placed under a plastic lens of $D_{lens} = 15\lambda_0$ in (a) H-plane and (b) E-plane.

In order to visualise how the lens reflections affect the mutual coupling all over the ground plane, a 2-D mutual coupling graph is calculated for an off-axis scenario. Figure 4.9 shows the 2-D mutual coupling graph between the first test feed (Source 1) which is placed off-axis at -4 beams in the H-plane and the second test feed that is displaced in two directions across the ground plane under the lens. The surge in the mutual coupling value around the mirror region becomes particularly clear from this graph. In addition, the regions on the ground plane under the lens (marked by the dashed black circle) indicates where the mutual coupling is prominent.

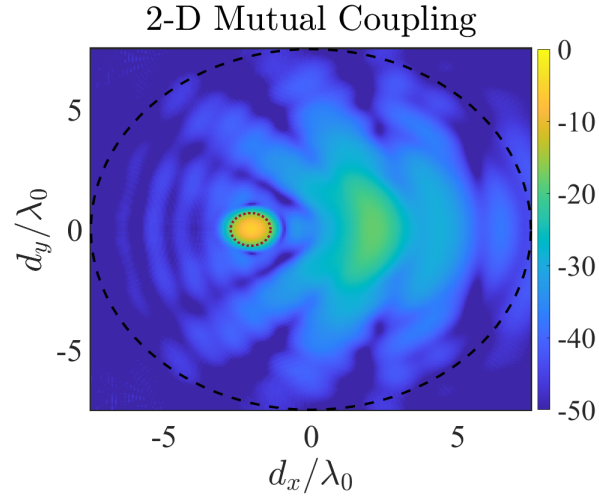


Figure 4.9: 2-D graph of mutual coupling distribution between two Gaussian feeds placed under a plastic lens of $D_{lens} = 15\lambda_0$. The transmission feed location is marked by the red dotted circle. The location of the receiving feed is displaced by d_x and d_y values over the lens focal plane.

Similarly, the mutual coupling between two feeds is calculated for the case when Source 1 (Gaussian feed) is placed under the smaller plastic lens of diameter, $D_{lens} = 6\lambda_0$. The far-field radiation pattern of the smaller lens antenna where Source 1 is placed at the focus of the lens is as shown in Figure 4.10. Similar to the previous case, the lens antenna radiation efficiency is $\eta_r = 0.906$. Figure 4.11 shows the far-field radiation pattern of the lens antenna when the Gaussian feed is displaced to -1.5 beams in both planes. The lens antenna in this case has a radiation efficiency of $\eta_r = 0.75$.

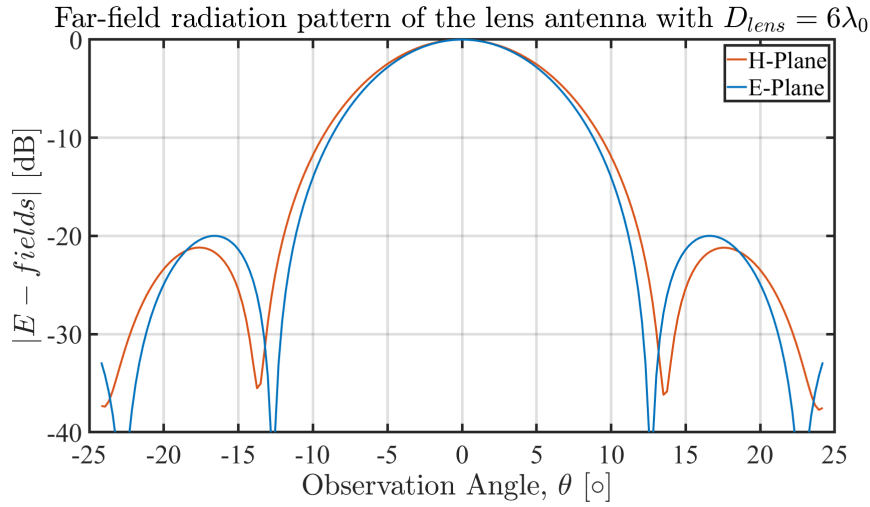


Figure 4.10: Far-field radiation pattern of the lens antenna when the Gaussian feed (Source 1) is placed under a plastic lens of $D_{lens} = 6\lambda_0$.

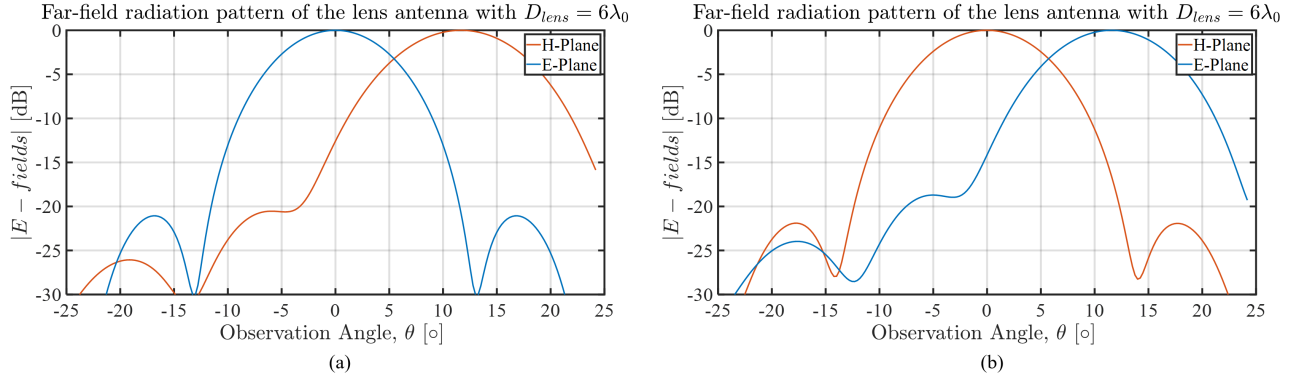


Figure 4.11: Far-field radiation pattern of the lens antenna when the Gaussian feed (Source 1) is displaced to -1.5 beams from the focus in (a) H-plane and (b) E-plane of a plastic lens of $D_{lens} = 6\lambda_0$.

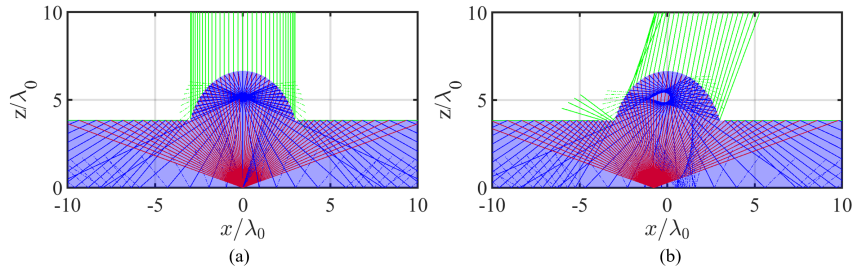


Figure 4.12: Ray tracing picture of a feed (a) placed at focus, and (b) displaced to -1.5 beams from the focus of a plastic lens with $D_{lens} = 6\lambda_0$. The incident, reflected and transmitted rays are indicated with red, blue, and green colours, respectively.

Figure 4.12 shows the ray-tracing pictures of the case when the first test feed is placed at the focus of the lens and when it is displaced to -1.5 beams from the focus of the lens. The mutual coupling results obtained when Source 1 is displaced to -1.5 beams is compared to the results obtained when the feed is placed at the focus of the lens in Figure 4.13. It can be observed in the smaller lens case that the mutual coupling results obtained for the off-axis feed scenario does not peak at the mirror position, rather the results remain consistently significant until 2λ , particularly in the H-plane. This is due to the fact that the second reflections in the small lens do not converge precisely at the mirror position but are spread all around the mirror area, as seen in the ray tracing image shown in Figure 4.12 (b). In other words, the second reflection phenomenon in smaller lens exhibits less directive behaviour with respect to the one of the larger lens. It is also noteworthy to mention that the mutual coupling value obtained between two feeds under a lens for an off-axis scenario is higher for the smaller lens as opposed to the bigger lens.

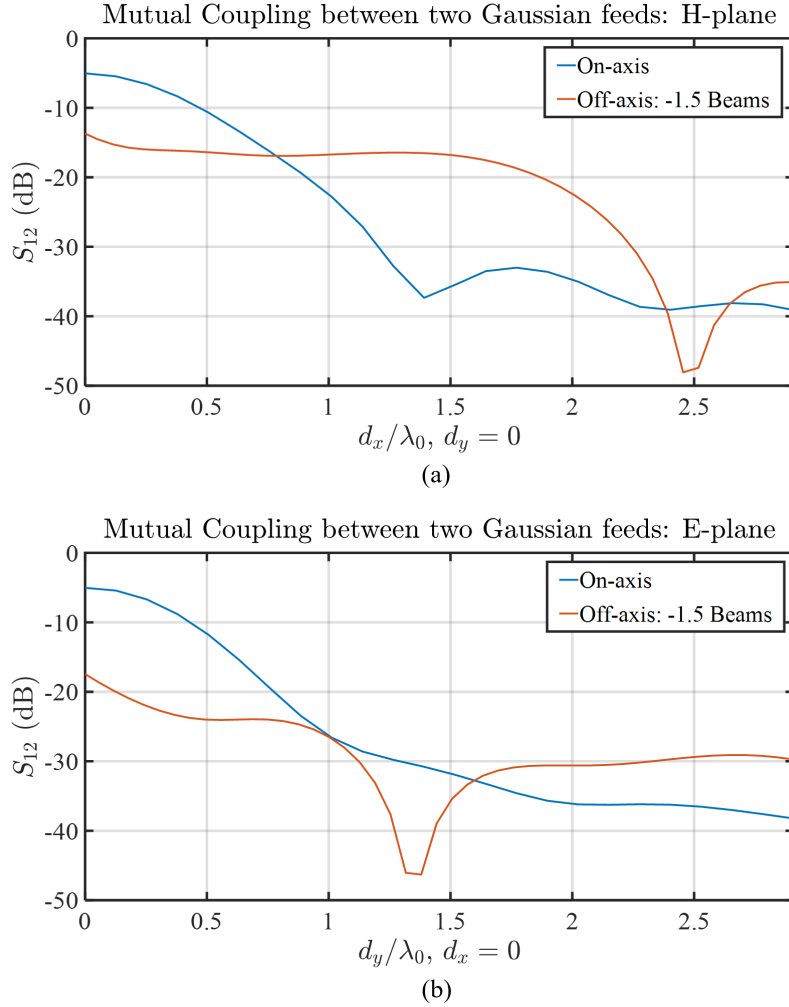


Figure 4.13: Mutual coupling between two Gaussian feeds when placed under a plastic lens of $D_{lens} = 6\lambda_0$ in (a) H-plane and (b) E-plane.

4.3.2. Effect of feed pattern on mutual coupling

In order to understand the impact of lens truncation angle and the feed type on the mutual coupling between feeds, the results obtained for mutual coupling using Source 1 is compared with the results calculated using sources 2 and 3. Source 2 is placed under a plastic lens with the same specifications as the one used for Source 1, whereas Source 3 is placed under a plastic lens with an $f_{\#} = 1$ thus resulting in a lens truncation angle of 30° . The solid angle where only first reflections occur when the feed is placed at the focus of this lens is $\theta_{\Omega} = 22^\circ$ in comparison to the case of the previous lens of $f_{\#} = 0.812$ where the solid angle was $\theta_{\Omega} = 16^\circ$. The region of the lens surface that contribute to second reflections forms an angular region of 8° on either side of the solid angle for the plastic lens of $f_{\#} = 1$. On the other hand, the angular region for the second reflections is 16° on either side of the solid angle for the plastic lens of $f_{\#} = 0.812$. The on- and off-axis ray tracing pictures for a plastic lens of $D_{lens} = 15\lambda_0$ having an $f_{\#} = 1$ are shown as examples in Figure 4.14.

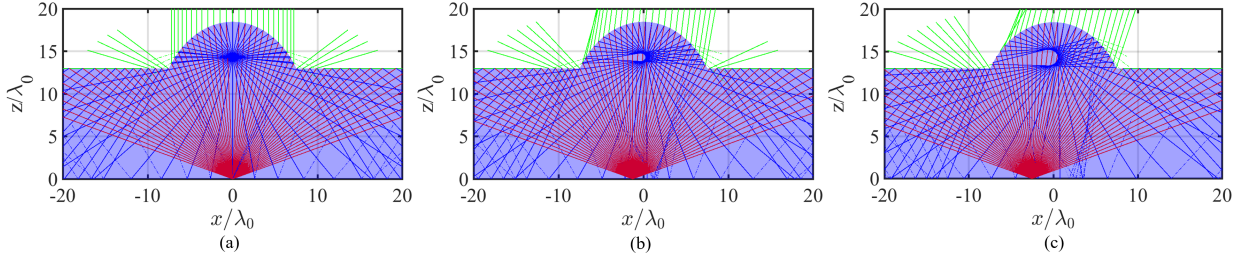


Figure 4.14: Ray tracing picture of a feed (a) placed at focus, (b) displaced to -2 beams, and (c) displaced to -4 beams from the focus of a plastic lens with $D_{lens} = 15\lambda_0$ having an $f_{\#} = 1$. The incident, reflected and transmitted rays are indicated with red, blue, and green colours, respectively.

The mutual coupling between two feeds in H- and E-plane when the first test feed is placed at the focus of the lens with $D_{lens} = 15\lambda_0$ is shown in Figure 4.15 (a) and (b), respectively, for all the three different feeds. It can be observed from the results that the mutual coupling values for all the three feeds are comparable for the on-axis case, especially in the H-plane. This is due to the fact that the impact on the mutual coupling is predominantly affected by the first reflections that are uniformly spread across the ground plane, as can be seen from the solid blue lines shown in the ray tracing pictures in Figure 4.7 (a) and Figure 4.14 (a). It can be seen from the graph that the mutual coupling pattern for Source 2 in the E-plane has severe oscillations. These are associated to the interference between the side lobe of the feed far-field of the feed and the reflected fields from the lens surface.

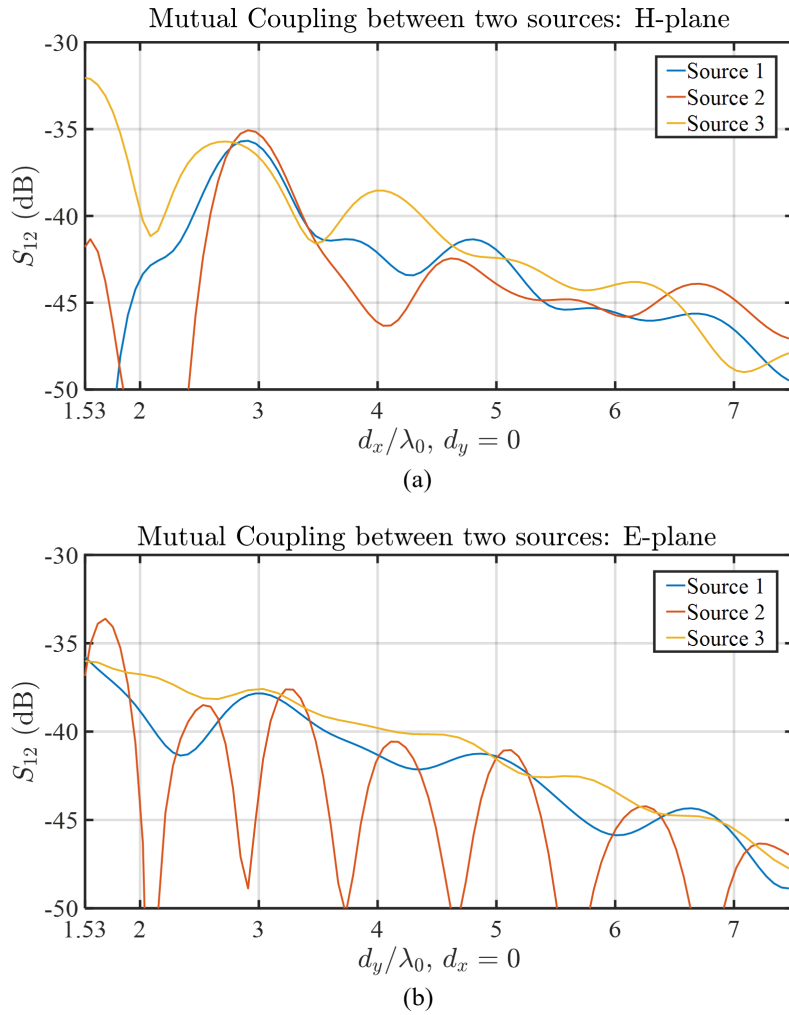


Figure 4.15: Mutual coupling between two feeds in (a) H-plane, and (b) E-plane when placed at the focus of a plastic lens with $D_{lens} = 15\lambda_0$.

In off-axis cases, where the feed is displaced to -2 beams and -4 beams in the H-plane, the mutual coupling results obtained are as shown in Figure 4.16 (a) and (b), respectively. Although the mutual coupling values obtained for Source 3 are comparable to the ones obtained using Sources 1 and 2, its pattern is slightly different. This can be attributed to the fact that the lens truncation angle is smaller for Source 3, thus the angular region where the second reflections occur is smaller, especially for displaced source case, as seen in the ray-tracing picture in Figure 4.14 (b) and (c).

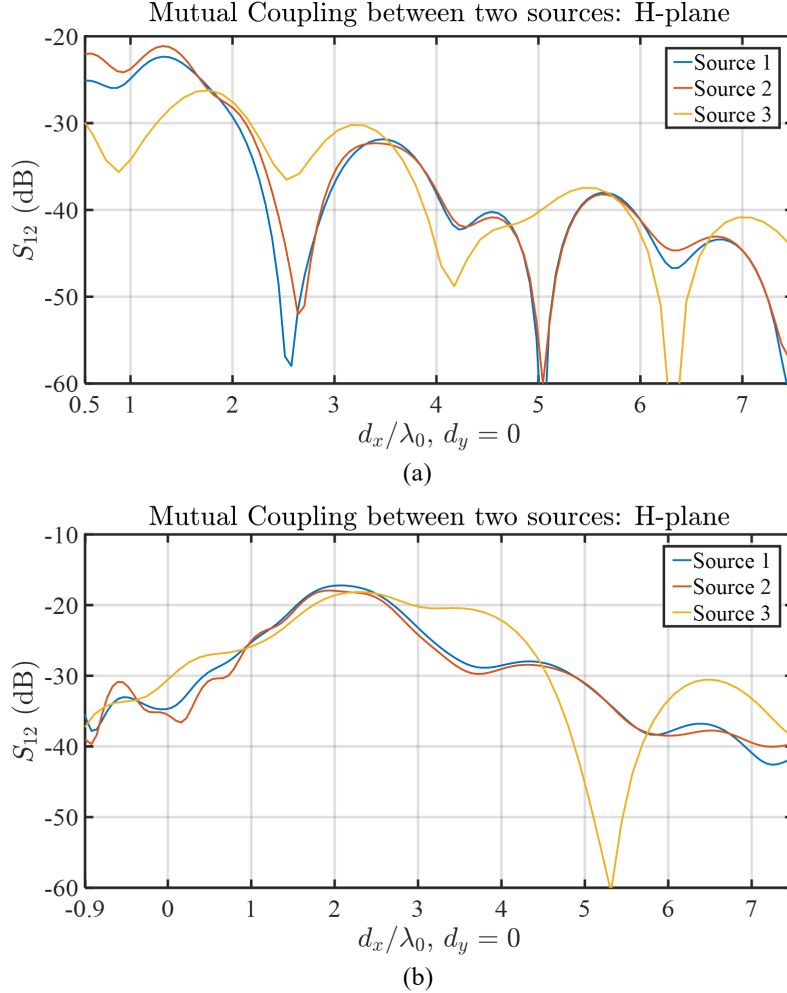


Figure 4.16: Mutual coupling between two feeds in H-plane when the first test feed is displaced to (a) -2 beams, and (b) -4 beams from the focus of a plastic lens with $D_{lens} = 15\lambda_0$.

Hence, from the above results it can be concluded for the considered cases that the lens truncation angle and the feed type does influence the mutual coupling between two feeds under a lens. The effect is more prominent for the off-axis cases, i.e, the case when the first test feed is displaced from the focus of the elliptical lens. Therefore, as part of the design procedure for a lens antenna with multiple feeds, it is insightful to evaluate the mutual coupling level for each specific lens antenna geometry. In order to understand how varying the lens material would impact the mutual coupling between two feeds, silicon lens case study is also performed. The results and inferences obtained from this study is elucidated in Chapter 5.

5

Case Study: Silicon Lens

In this chapter, the effect on mutual coupling between two antenna feeds under a lens is studied for the case when the lens material is changed to silicon ($\epsilon_r = 11.9$). Similar to the case of plastic lens, two different lens diameters are considered for the silicon lens: $D_{lens} = 6\lambda_0$ and $D_{lens} = 15\lambda_0$.

5.1. Geometry of the considered silicon lenses

For the case of silicon lenses ($\epsilon_r = 11.9$), the eccentricity (e) is equal to 0.28 thus making the shape of the silicon lenses close to a circle. The impact of the silicon material on the lens curvature can be clearly observed from the ray tracing picture in Figure 5.1, for a lens of $D_{lens} = 15\lambda_0$ and $f_{\#} = 0.55$, i.e. a truncation angle of 65° . One can see that the solid angle, Ω (highlighted in orange), where secondary reflections from the lens surface do not occur, is much wider than the case of the plastic lens. From the Figure 5.1, it can be seen that for an on-axis scenario, the secondary reflections occur only at the extreme edge of the lens. Consequently, the mutual coupling between two feeds under a silicon lens is impacted by the secondary reflections only when the lens truncation angle is significantly large.

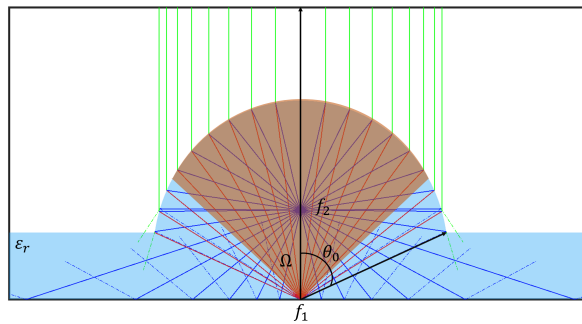


Figure 5.1: Ray tracing picture of a feed placed at the focus of an elliptical lens with $\epsilon_r = 11.9$, $D_{lens} = 15\lambda_0$ and $f_{\#} = 0.55$. The solid angle, Ω , is highlighted in orange. The incident, reflected and transmitted rays are indicated with red, blue, and green colours, respectively.

In order to compare the silicon lens surface to the plastic case, a ray tracing analysis is performed using silicon material for the same lens diameter and $f_{\#}$ as the plastic lens described in Section 4.3.1. Figure 5.2 shows the ray tracing pictures for on- and off-axis cases when a feed is placed under a silicon lens of $f_{\#} = 1$, i.e. a truncation angle of 30° . Unlike the plastic lens, where a truncation angle of 30° resulted in a curved lens surface, in the case of silicon material the lens surface is seemingly flat. The ray-tracing pictures for both on-axis and off-axis case clearly shows that only primary (first) reflections (shown in solid blue lines) occur on the lens surface. Therefore, unlike the case for the plastic lenses, there will be no secondary reflections contributing to the mutual coupling calculation in the GO-PO model.

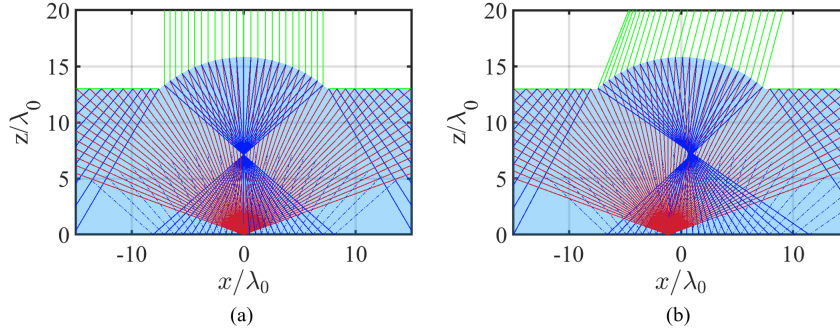


Figure 5.2: Ray tracing picture of a feed (a) placed at the focus, and (b) displaced to -4 beams in the H-plane from the focus of an elliptical lens with $\epsilon_r = 11.9$ and $D_{lens} = 15\lambda_0$. The incident, reflected and transmitted rays are indicated with red, blue, and green colours, respectively.

Similar to the case study performed for plastic lenses, different types of sources are placed under large ($D_{lens} = 15\lambda_0$) and small ($D_{lens} = 6\lambda_0$) silicon lens to see their corresponding impacts on the mutual coupling. The considered feeds and their far-field radiation pattern are described in Section 5.2.

5.2. Considered silicon lens antenna feeds

The impact of lens illumination is studied here for feeds with different radiation patterns, varying from broad beams to more directive feeds. Here, the following two types of feeds are considered:

- Source 1: A Double slot with -10 dB edge taper at 50° . The geometry of the double slot and its far-field radiation pattern is as shown in Figure 5.3 (a)
- Source 2: A Gaussian feed with an edge taper of -13 dB at 30° , whose far-field radiation pattern is shown in Figure 5.3 (b)

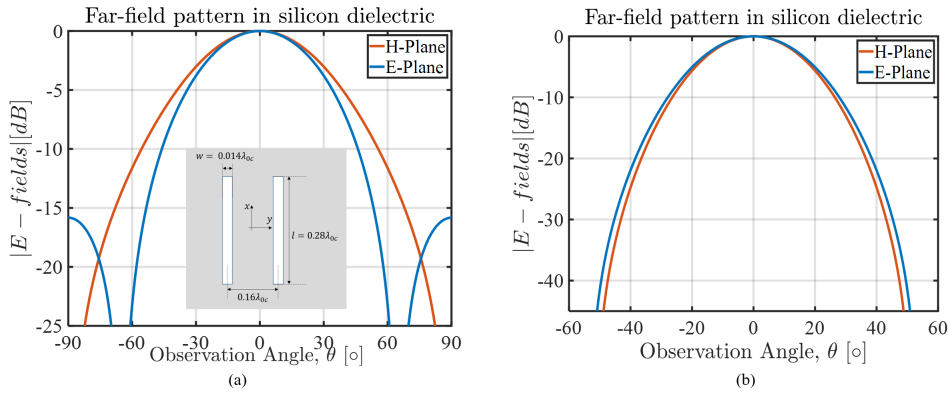


Figure 5.3: Far-field radiation pattern of (a) Source 1: Double slot with -10dB edge taper at 50° and (b) Source 2: Gaussian feed with an edge taper of -13dB in silicon ($\epsilon_r = 11.9$) homogeneous medium.

The far-field radiation pattern of these feeds are calculated in a homogeneous medium with a relative permittivity of $\epsilon_r = 11.9$. The cases considered for silicon lens study using different lens geometries and feed types are documented below.

	Lens Diameter	$f_{\#}$	Feed Type	Edge Taper	Feed Location	Broadside Directivity	Broadside Radiation Efficiency
Case 1	$15\lambda_0$	0.65	Source 1: Double Slot	-10 dB	On-axis Off-axis: -2 Beams, -4 Beams, -6 Beams	33.31 dB	0.84
Case 2	$6\lambda_0$	0.65	Source 1: Double Slot	-10 dB	On-axis Off-axis: -1.5 Beams	25.36 dB	0.84
Case 3	$15\lambda_0$	1	Source 2: Gaussian	-13 dB	On-axis Off-axis: -2 Beams	32.97 dB	0.94

Table 5.1: Silicon Lens Case Study

5.3. Results and Inferences

The mutual coupling analysis for lens antennas in silicon material were generated using the GO-PO model for different lens diameters, lens truncation angle and for the different feed types as described in Section 5.2.

5.3.1. Impact of the lens diameter

Consider the case where the double slot (Source 1) is placed at the focus of a silicon lens with $D_{lens} = 15\lambda_0$ having an $f_{\#} = 0.65$ (truncation angle = 50°). The far-field radiation pattern of this lens antenna, when the feed is at the lower focus of the lens (broadside) is shown in Figure 5.5. The silicon lens is covered with a standard quarter wavelength matching layer with a relative permittivity of $\epsilon_{rm} = 3.44$. This lens antenna has a radiation efficiency of $\eta_r = \frac{P_{rad}^{lens}}{P_{feed}^{rad}} = 0.8442$.

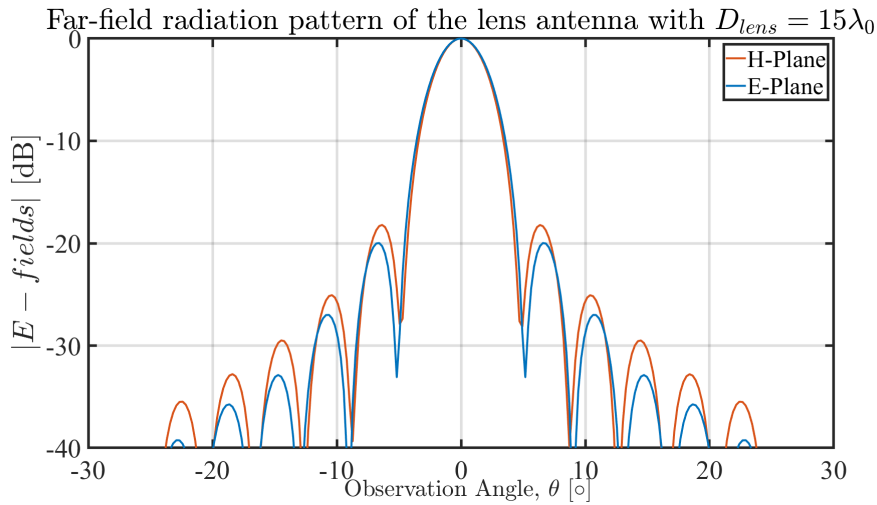


Figure 5.4: Far-field radiation pattern of the lens antenna (with matching layer) when the Double slot source (Source 1) is placed under a silicon lens of $D_{lens} = 15\lambda_0$.

Figure 5.5 shows the examples of lens antenna radiation pattern when the Double slot source is displaced to -2 beams and -4 beams in the H-plane. The radiation efficiency of the lens antenna changes to $\eta_r = 0.83$ when the Double slot feed is displaced to -2 beams, and to $\eta_r = 0.78$ when the feed is displaced to -4 beams.

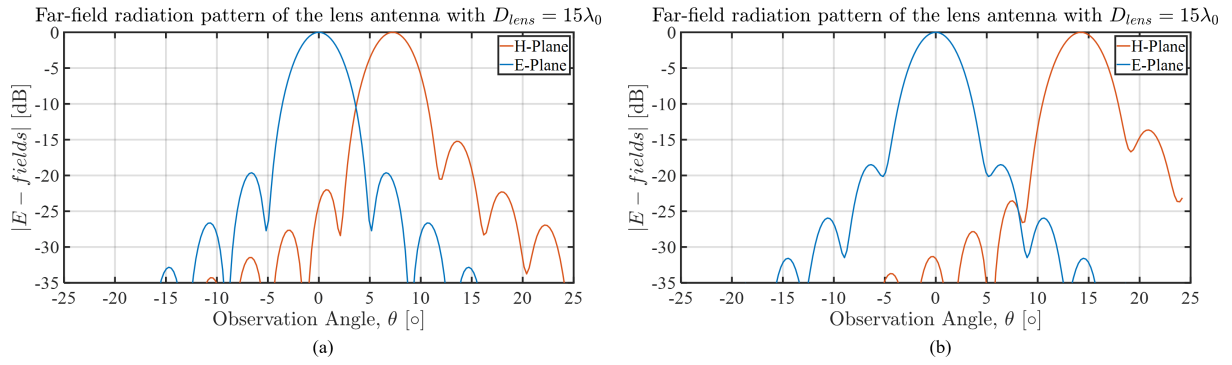


Figure 5.5: Far-field radiation pattern of the lens antenna (with matching layer) when the Double slot source (Source 1) is displaced to (a) -2 beams and (b) -4 beams in the H-plane from the focus of the silicon lens of $D_{lens} = 15\lambda_0$.

The ray-tracing picture for a feed placed at the focus of this elliptical lens is shown in Figure 5.6 (a). The feed is displaced to -2 beams, -4 beams and -6 beams to see the impact of off-axis scenarios on the ray tracing analysis. Figure 5.6 (b), (c) and (d) depicts the the ray tracing picture for these off-axis cases.

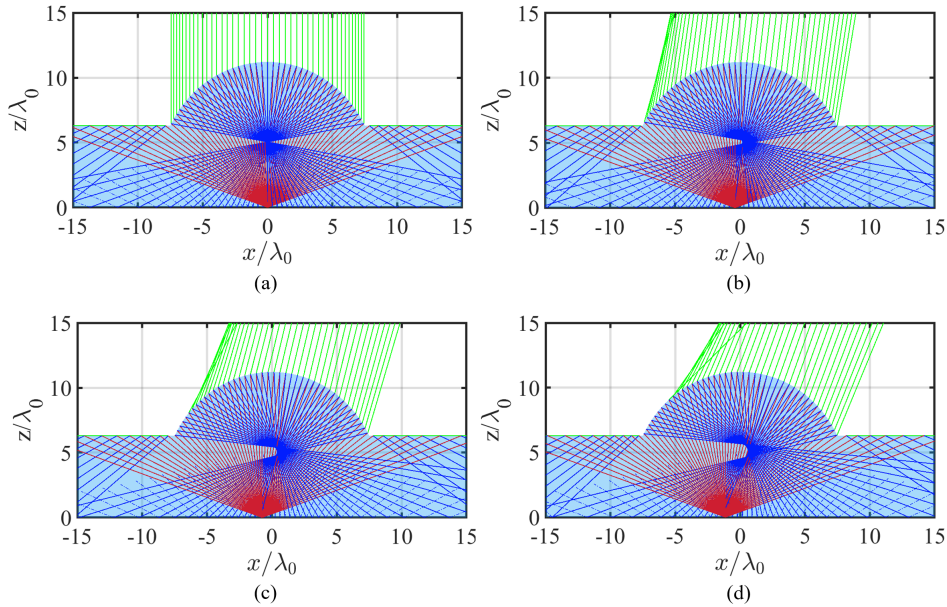


Figure 5.6: Ray tracing picture of a feed (a) placed at the focus, (b) displaced to -2 beams, (c) displaced to -4 beams, and (d) displaced to -6 beams in the H-plane from the focus of a silicon lens with $D_{lens} = 15\lambda_0$ and $f_{\#} = 0.65$. The incident, reflected and transmitted rays are indicated with red, blue, and green colours, respectively.

The mutual coupling results generated for the case when the double slot feed is placed on-axis and off-axis under a silicon lens without a matching layer is shown in Figure 5.7. The values obtained for mutual coupling between the two double slot feeds in both on- and off-axis scenarios are comparable since there are no secondary reflections from the lens surface to create a focusing pattern over the ground plane. The mutual coupling pattern is more smooth in the H-plane as opposed to the E-plane one since the far-field of the double slot, as shown in Figure 5.3 (a), has a broader pattern in the H-plane compared to the E-plane thus illuminating the the silicon lens surface more uniformly.

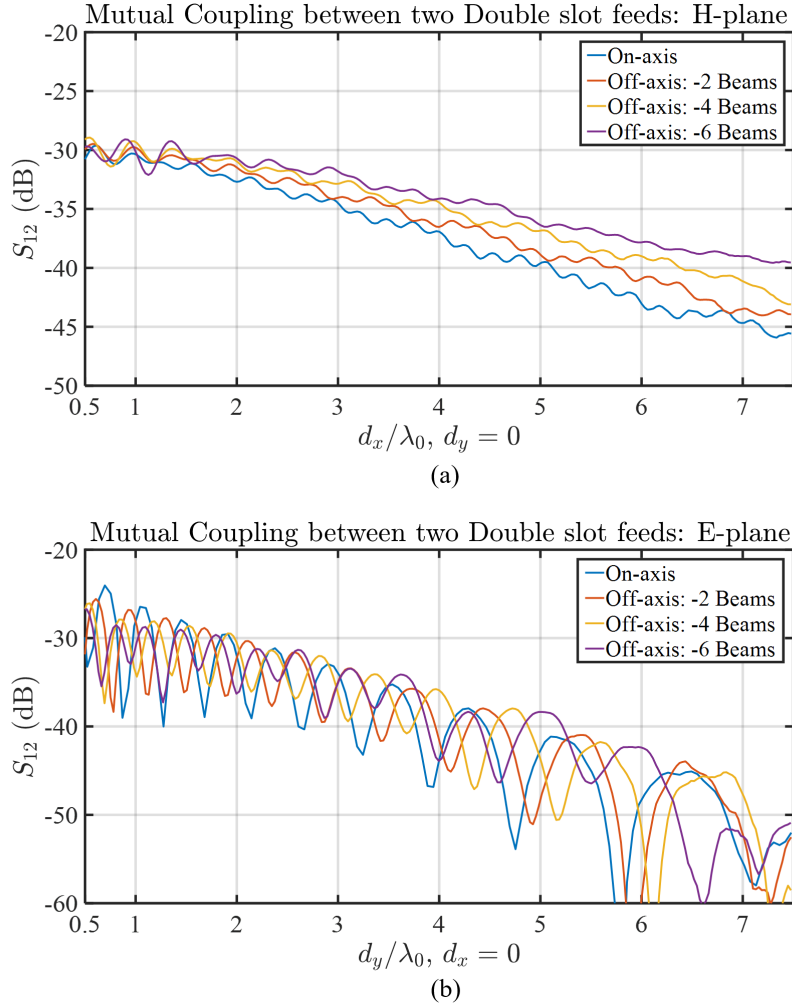


Figure 5.7: Mutual coupling between two Double slot feeds when placed under a silicon lens of $D_{lens} = 15\lambda_0$ and $f_{\#} = 0.65$ in (a) H-plane and (b) E-plane.

Likewise, the mutual coupling between two double slot feeds is calculated when the feeds are placed under a smaller silicon lens of $D_{lens} = 6\lambda_0$. The far-field radiation pattern for this lens case is shown in Figure 5.8 for on- and off-axis feed cases. The radiation efficiency of the lens antenna for the on-axis case is $\eta_r = 0.84$ and for the case when the feed is displaced to -1.5 beams in the H-plane is $\eta_r = 0.78$. The ray tracing picture for the smaller lens case is shown in Figure 5.9 for on- and off-axis case and the mutual coupling results obtained in both the main planes are shown in Figure 5.10.

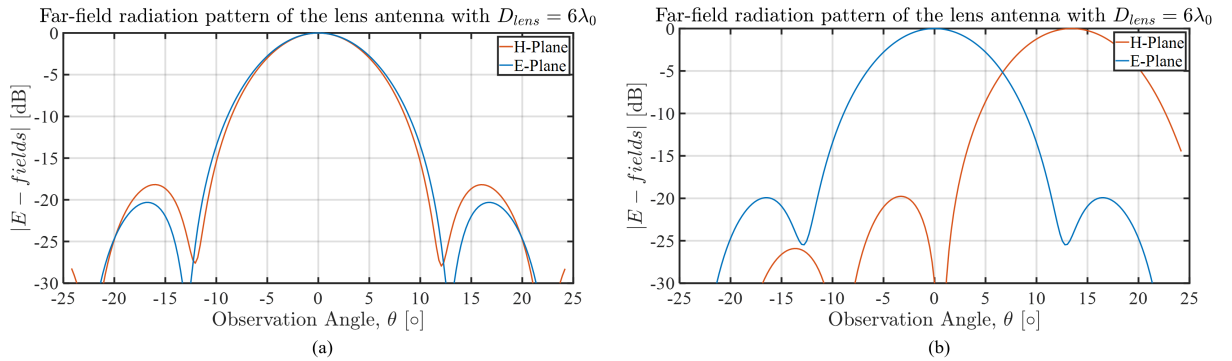


Figure 5.8: Far-field radiation pattern of the lens antenna (with matching layer) when the Double slot source (Source 1) is (a) at focus and (b) displaced to -1.5 beams in the H-plane from the focus of the silicon lens of $D_{lens} = 15\lambda_0$.

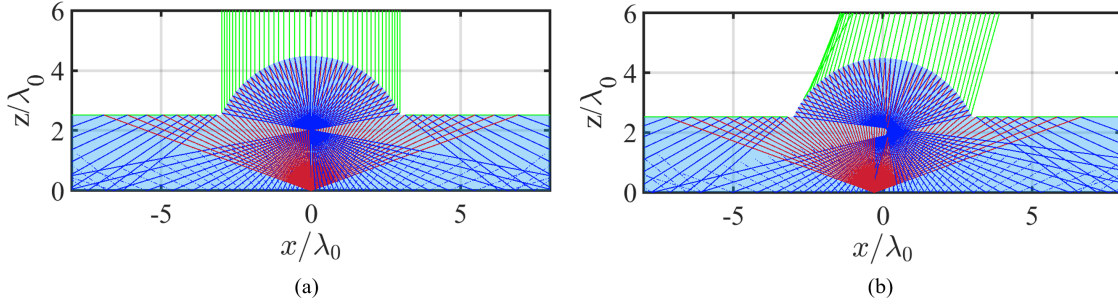


Figure 5.9: Ray tracing picture of a feed (a) placed at the focus, and (b) displaced to -1.5 beams in the H-plane from the focus of a silicon lens with $D_{lens} = 6\lambda_0$ and $f_{\#} = 0.65$. The incident, reflected and transmitted rays are indicated with red, blue, and green colours, respectively.

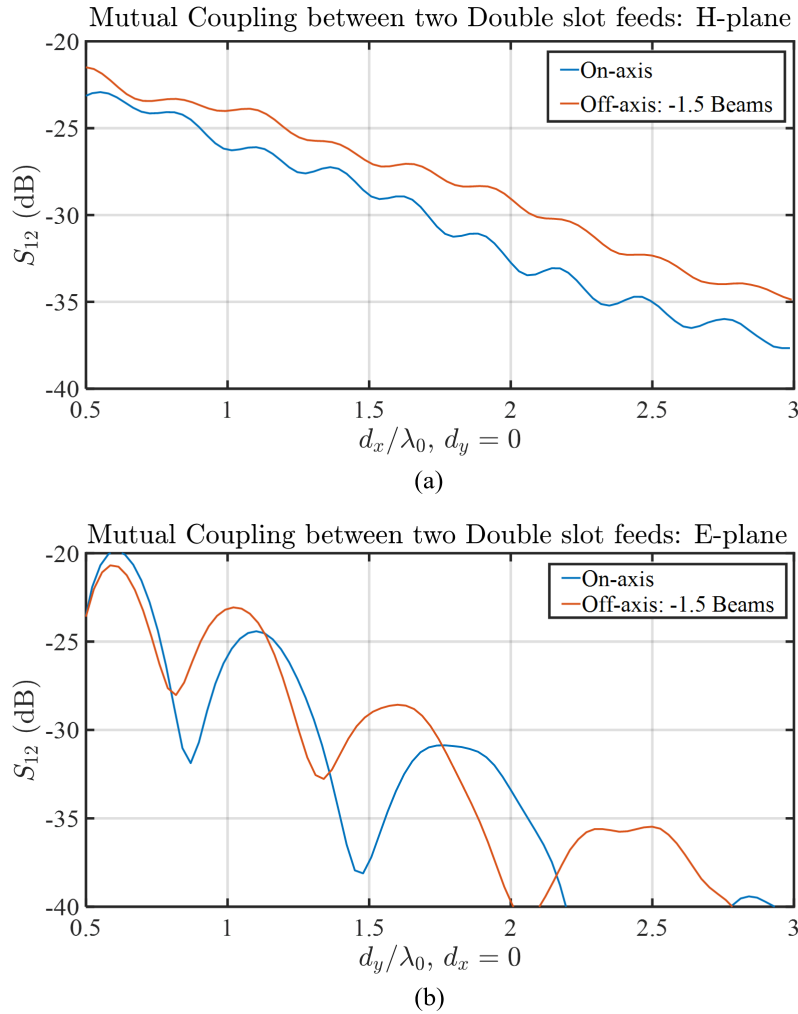


Figure 5.10: Mutual coupling between two Double slot feeds when placed under a silicon lens of $D_{lens} = 6\lambda_0$ and $f_{\#} = 0.65$ in (a) H-plane and (b) E-plane.

It is clear from the above graph that the pattern of the mutual coupling under the smaller lens follows that of the bigger lens, since there are no secondary reflections in the smaller lens as well. However, the field radiated from the lens surface by the first reflection is spread over a smaller region which leads to significantly higher mutual coupling levels ($\sim 10\text{dB}$) for the smaller lenses.

5.3.1.1. Effect of matching layer on the mutual coupling

Typically, in a silicon lens a matching layer is coated over the lens surface in order to improve the reflection efficiency. The matching layer acts as a quarter wavelength impedance transformer that ensures that most of the power from the antenna feed is transmitted outside the lens. The ideal matching layer considered here has a thickness of $\frac{\lambda_0}{4\sqrt{\epsilon_{rm}}}$ and a dielectric constant of $\epsilon_{rm} = \sqrt{\epsilon_r}$ where $\epsilon_r = 11.9$ for silicon. Figure 5.11 depicts the mutual coupling results obtained when a matching layer is added to the silicon lens surface in comparison to the results obtained without a matching layer. This comparison is performed for both on-axis and off-axis case for a silicon lens of $D_{lens} = 15\lambda_0$. The impact of the matching layer on the mutual coupling results is evident from the graph. Since most of the power is transmitted out of the lens, the EM fields that reflect back from the lens surface carry much lesser power thus reducing the mutual coupling. In the E-plane the impact of matching layer is less visible since the mutual coupling between the two sources in this plane is strongly affected by the null present in the far-field of the double slot. The far-field pattern of the Double slot is shown in Figure 5.3 (a).

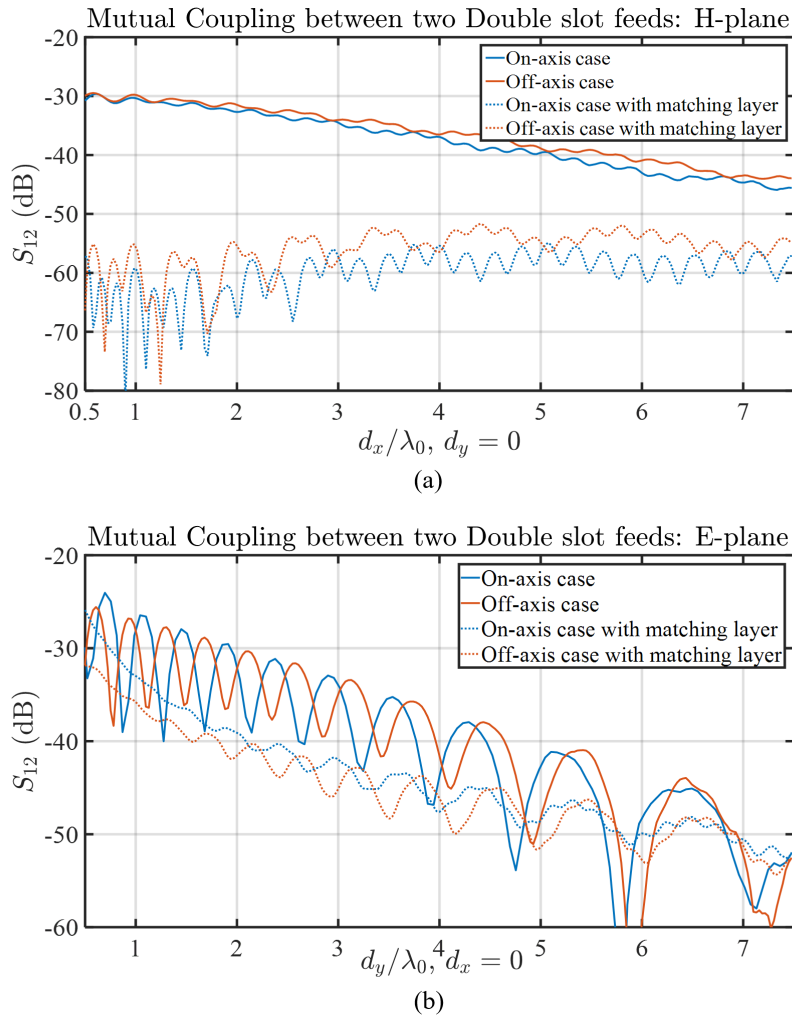


Figure 5.11: Mutual coupling between two Double slot feeds when placed under a silicon lens of $D_{lens} = 15\lambda_0$ and $f_{\#} = 0.6527$ in (a) H-plane and (b) E-plane.

5.3.2. Effect of the feed pattern on the mutual coupling

In this section, the mutual coupling results obtained using the double slot feed placed under the silicon lens of $f_{\#} = 0.65$ is compared with the results obtained for the case when a Gaussian feed is placed under the silicon lens of $f_{\#} = 1$ (truncation angle = 30°). The far-field radiation pattern of the silicon lens antenna with the Gaussian feed placed at the focus of the ellipse is shown in Figure 5.12. The radiation efficiency of this

lens antenna is $\eta_r = 0.94$. The ray tracing picture for this lens is depicted in Figure 5.2(a).

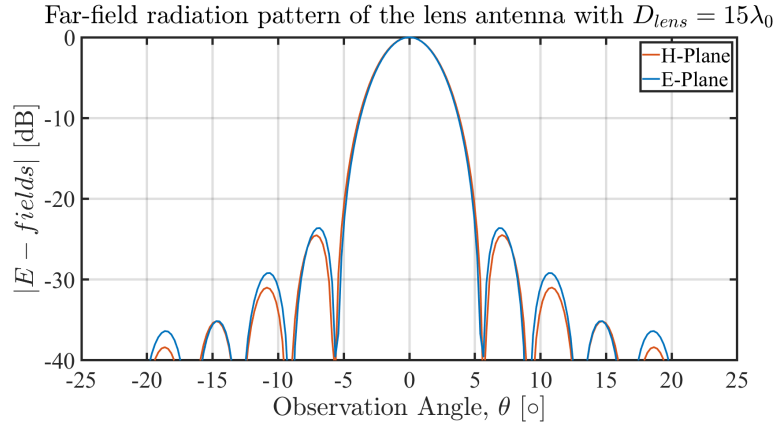


Figure 5.12: Far-field radiation pattern of the lens antenna (with matching layer) when the Gaussian source (Source 2) placed at the focus of the silicon lens of $D_{lens} = 15\lambda_0$.

Figure 5.13 compares the mutual coupling between the two feeds when the transmitting feed is placed at the focus of the silicon lens of $D_{lens} = 15\lambda_0$ in both H- and E-plane. The figure also compares the mutual coupling results achieved with and without the presence of a matching layer. Figure 5.14 shows a similar example with both the feeds displaced to -2 beams in the H-plane.

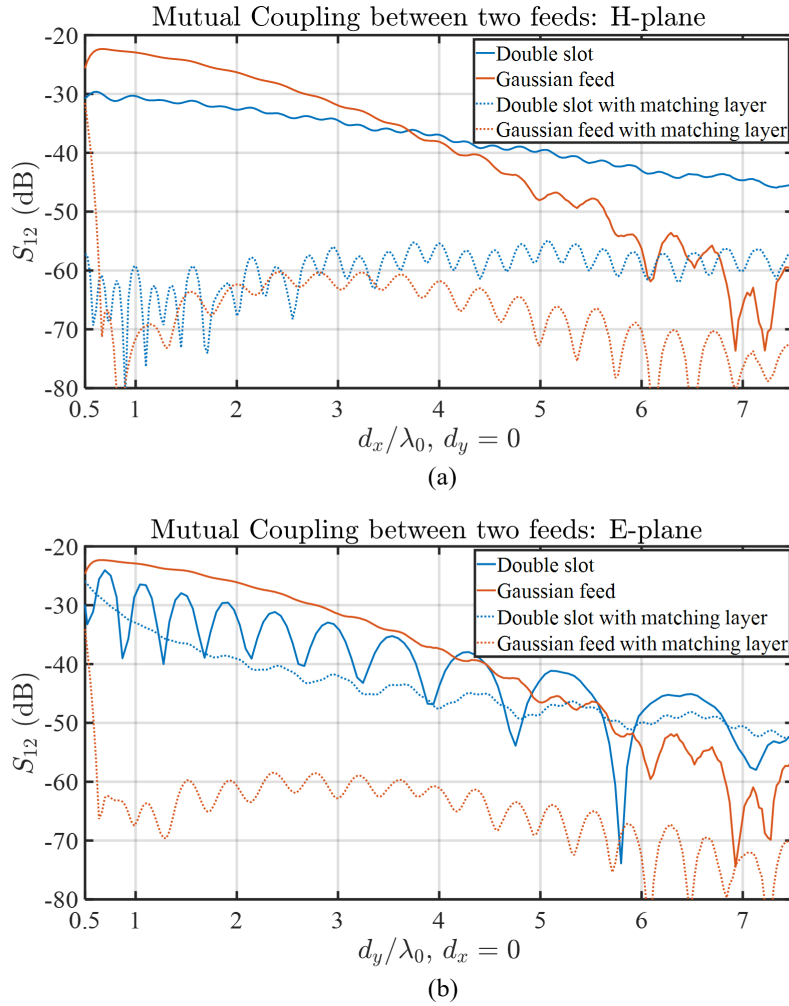


Figure 5.13: Mutual coupling between two feeds in (a) H-plane and (b) E-plane when the first feed is placed at the focus of a silicon lens of $D_{lens} = 15\lambda_0$.

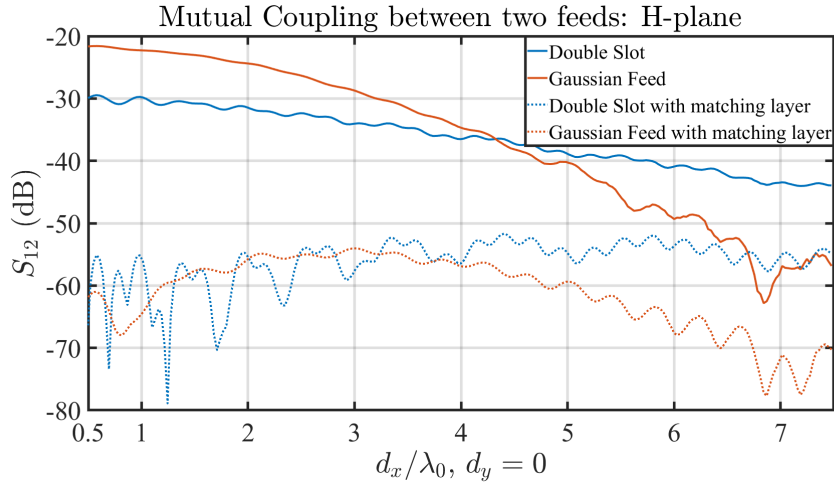


Figure 5.14: Mutual coupling between two feeds in H-plane when the first feed is displaced to -2 beams in the H-plane from the focus of a silicon lens of $D_{lens} = 15\lambda_0$.

From Figure 5.13, it can be observed that the mutual coupling value drops faster for the Gaussian feed (Source 2) placed under the silicon lens of $f_{\#} = 1$ as compared to the case of the double slot feed placed under the silicon lens of $f_{\#} = 0.65$. This can be accredited to the smaller truncation angle, resulting in a smaller surface area of the lens and thus a lower impact of first reflections especially at the locations near the lens edge. The addition of the matching layer over both lens cases results in a significant drop in the mutual coupling. Thus making the matching layer a necessary addition over the silicon lenses for mutual coupling reduction, despite the manufacturing complexity.

A 2-D mutual coupling pattern is generated for the silicon lens case, where the Gaussian feed is displaced to -4 beams from the focus of the lens, in the H-plane. Figure 5.15 shows this 2-D mutual coupling result obtained. Comparing this 2-D result with the one calculated for the plastic lens as shown in Figure 4.9, it can be observed that the silicon lens is clearly impacted by only the primary reflections and the mutual coupling level does not show significant increment in any particular region like in the case of plastic lens.

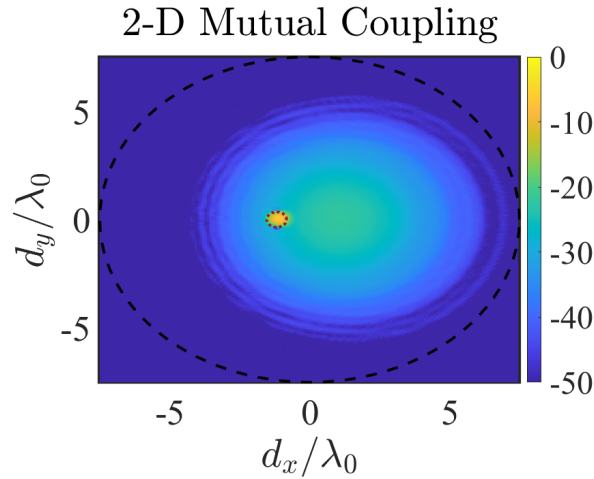


Figure 5.15: 2-D graph of mutual coupling distribution between two Gaussian feeds placed under a silicon lens of $D_{lens} = 15\lambda_0$. The transmission feed location is marked by the red dotted circle. The location of the receiving feed is displaced by dx and dy values over the lens focal plane.

Thus, based on the above results and the ones obtained in Chapter 4, it can be concluded that depending on the lens material the main contributing phenomenon to the mutual coupling between feeds placed under the lens changes and requires specific attention based on the geometry under consideration.

6

Conclusion

6.1. Summary and Conclusion

Lens antennas have been gaining traction for high frequency applications such as communication systems, phased arrays, MIMO RADAR systems in order to radiate the EM fields efficiently. Despite having significantly high radiation efficiency, lens antennas suffer from mutual coupling due to multiple internal reflections at the lens interface that leads to degradation of the system performance. There is not enough literature available to study the impact of mutual coupling under a lens antenna system. Hence, the aim of this thesis was to study the impact of mutual coupling in such systems and propose a model to evaluate this coupling using high frequency EM analysis techniques.

The model described in this thesis incorporates a simple analytical forward ray tracing approach to obtain the path of the reflected EM rays from the lens surface. A Geometrical Optics - Physical Optics (GO-PO) approximation method is added to the ray tracing to calculate the amplitude and phase of the reflected rays that would impinge on the antenna elements. The model accounts for ray caustics, thus making the GO-PO model well suited for the EM field approximations. In order to make the code computationally efficient, the antenna in reception formalism is used to estimate the mutual coupling between elements under a lens. This model provides the flexibility to analyse the effect of mutual coupling under various scenarios such as different feed types, lens material, lens geometries, and feed locations. Although the method described here accounts for reflections inside the lens until the second order reflections, it does not take into account the diffraction that occurs at the lens edge.

While the mutual coupling between elements under a lens can be evaluated using a full-wave simulation tool, the method is computationally intensive. In order to study the impact of mutual coupling between feeds based on their relative distance, several simulations need to be performed thus making the process extremely time consuming. The GO-PO model on the other hand can calculate the mutual coupling between two feeds as a function of their relative distance in one calculation cycle.

Several lens antenna scenarios were studied using the GO-PO model in order to understand the parameters most affecting the mutual coupling. Two comprehensive cases studies were performed and the inferences have been documented in this thesis. The lens material was found to impact the mutual coupling levels as it influences the lens curvature, the solid angle and hence the area on the lens surface where primary (1^{st}) and secondary (2^{nd}) reflections occur. For example, for the same truncation angle and lens diameter, the mutual coupling in plastic lens antennas were affected by both 1^{st} and 2^{nd} reflections, whereas there were no secondary reflections in the silicon lens antenna case. It was also observed in the case of plastic lenses that changing the lens diameter changed the directivity of the secondary reflections for the off-axis antenna element cases. The second reflection phenomenon in smaller lens case exhibited less directive behaviour with respect to the one of the larger lens case.

The lens edge illumination was also found to be an important parameter that affected the mutual coupling levels. It was observed in the case of plastic lenses that when more power from the feed illuminated the lens

edge, the second reflections contributions to the mutual coupling were more significant. When a feed with a more directive pattern was used, the mutual coupling pattern was observed to be impacted by only the first reflections. A study was also performed using silicon lenses to understand the impact of matching layer on the mutual coupling levels. It was found that the mutual coupling showed significant drop (~ 20 dB) in value over the entire lens focal plane.

In conclusion, the study lead to the understanding that when different feed types and/or lens specifications are employed, the mutual coupling patterns change considerably. Therefore, it is necessary to analyse each unique design individually in terms of its mutual coupling performance.

6.2. Future Outlook

The model presented in this thesis to evaluate the mutual coupling between feeds under a single lens performs within the expected validity margin of the assumed approximations. This model can be expanded to multiple lens element arrays since the high frequency EM analysis tools such as ray tracing and GO-PO methods are not limited by the geometry of a single lens surface.

At present the model is coded in MATLAB. Subsequently, it can be made into a user interface tool for estimating mutual coupling levels for future lens antenna designs within the Terahertz Sensing group.

Bibliography

- [1] H. Zhang, S. Bosma, A. Neto, and N. Llombart, "A dual-polarized 27-dbi scanning lens phased array antenna for 5g point-to-point communications," *IEEE Transactions on Antennas and Propagation*, pp. 1–1, 2021.
- [2] G. Godi, R. Sauleau, and D. Thouroude, "Performance of reduced size substrate lens antennas for millimeter-wave communications," *IEEE Transactions on Antennas and Propagation*, vol. 53, no. 4, pp. 1278–1286, 2005.
- [3] M. Arias Campo, D. Blanco, S. Bruni, A. Neto, and N. Llombart, "On the use of fly's eye lenses with leaky-wave feeds for wideband communications," *IEEE Transactions on Antennas and Propagation*, vol. 68, no. 4, pp. 2480–2493, 2020.
- [4] J. Ala-Laurinaho, J. Aurinsalo, A. Karttunen, M. Kaunisto, A. Lamminen, J. Nurmiharju, A. V. Räsänen, J. Säily, and P. Wainio, "2-D beam-steerable integrated lens antenna system for 5G E-Band access and backhaul," *IEEE Transactions on Microwave Theory and Techniques*, vol. 64, no. 7, pp. 2244–2255, 2016.
- [5] A. Artemenko, A. Mozharovskiy, A. Maltsev, R. Maslennikov, A. Sevastyanov, and V. Ssorin, "Experimental Characterization of E-Band Two-Dimensional Electronically Beam-Steerable Integrated Lens Antennas," *IEEE Antennas and Wireless Propagation Letters*, vol. 12, pp. 1188–1191, 2013.
- [6] E. Gandini, A. Tamminen, A. Luukanen, and N. Llombart, "Wide field of view inversely magnified dual-lens for near-field submillimeter wavelength imagers," *IEEE Transactions on Antennas and Propagation*, vol. 66, no. 2, pp. 541–549, 2018.
- [7] M. Alonso-delPino, S. Bosma, C. Jung-Kubiak, G. Chattopadhyay, and N. Llombart, "Wideband multi-mode leaky-wave feed for scanning lens-phased array at submillimeter wavelengths," *IEEE Transactions on Terahertz Science and Technology*, vol. 11, no. 2, pp. 205–217, 2021.
- [8] A. Neto, S. Maci, and P. de Maagt, "Reflections inside an elliptical dielectric lens antenna," *IEE Proceedings - Microwaves, Antennas and Propagation*, vol. 145, no. 3, pp. 243–247, 1998.
- [9] M. Ozdemir, H. Arslan, and E. Arvas, "Mutual coupling effect in multiantenna wireless communication systems," in *GLOBECOM '03. IEEE Global Telecommunications Conference (IEEE Cat. No.03CH37489)*, vol. 2, pp. 829–833 Vol.2, 2003.
- [10] H. Singh, H. L. Sneha, and R. M. Jha, "Mutual coupling in phased arrays: A review," *International Journal of Antennas and Propagation*, vol. 2013, p. 348123, Apr 2013.
- [11] B. T. Arnold and M. A. Jensen, "The Effect of Antenna Mutual Coupling on MIMO Radar System Performance," *IEEE Transactions on Antennas and Propagation*, vol. 67, no. 3, pp. 1410–1416, 2019.
- [12] J. Christensen, A. Carlström, A. Emrich, and P. de Maagt, "The Geostationary Atmospheric Sounder (GAS)," in *Sensors, Systems, and Next-Generation Satellites X* (R. Meynart, S. P. Neeck, and H. Shimoda, eds.), vol. 6361, pp. 51 – 61, International Society for Optics and Photonics, SPIE, 2006.
- [13] H. Zhang, S. Bosma, A. Neto, and N. Llombart, "A Dual-Polarized 27-dbi Scanning Lens Phased Array Antenna for 5G Point-to-Point Communications," *IEEE Transactions on Antennas and Propagation*, vol. PP, pp. 1–1, 04 2021.
- [14] N. Llombart, D. Emer, M. Arias Campo, and E. McCune, "Fly's eye spherical antenna system for future tbps wireless communications," *European Conference on Antennas and Propagation*, 2017.
- [15] S. Sorensen and K. Pontoppidan, "Lens analysis methods for quasioptical systems," in *The Second European Conference on Antennas and Propagation, EuCAP 2007*, pp. 1–5, 2007.

- [16] E. Heyman and L. Felsen, "High frequency fields in the presence of a curved dielectric interface," *IEEE Transactions on Antennas and Propagation*, vol. 32, no. 9, pp. 969–978, 1984.
- [17] D. Pasqualini, F. Capolino, A. Toccafondi, and S. Maci, "High-frequency analysis of the surface induced currents on elliptical dielectric lens antennas," vol. 2, pp. 860 – 863 vol.2, 02 2000.
- [18] M. M. Taygur and T. F. Eibert, "A ray-tracing algorithm based on the computation of (exact) ray paths with bidirectional ray-tracing," *IEEE Transactions on Antennas and Propagation*, vol. 68, no. 8, pp. 6277–6286, 2020.
- [19] A. Neto, D. Pasqualini, A. Toccafondi, and S. Maci, "Mutual coupling between slots printed at the back of elliptical dielectric lenses," *IEEE Transactions on Antennas and Propagation*, vol. 47, no. 10, pp. 1504–1507, 1999.
- [20] J. Dong and A. I. Zaghoul, "Hybrid ray tracing method for microwave lens simulation," *IEEE Transactions on Antennas and Propagation*, vol. 59, no. 10, pp. 3786–3796, 2011.
- [21] M. M. Taygur, I. O. Sukharevsky, and T. F. Eibert, "A Bidirectional Ray-Tracing Method for Antenna Coupling Evaluation Based on the Reciprocity Theorem," *IEEE Transactions on Antennas and Propagation*, vol. 66, no. 12, pp. 6654–6664, 2018.
- [22] P. Pathak, "High frequency techniques for antenna analysis," *Proceedings of the IEEE*, vol. 80, no. 1, pp. 44–65, 1992.
- [23] M. Albani, G. Carluccio, and P. H. Pathak, "Uniform ray description for the po scattering by vertices in curved surface with curvilinear edges and relatively general boundary conditions," *IEEE Transactions on Antennas and Propagation*, vol. 59, no. 5, pp. 1587–1596, 2011.
- [24] D. Pasqualini and S. Maci, "High-frequency analysis of integrated dielectric lens antennas," *IEEE Transactions on Antennas and Propagation*, vol. 52, no. 3, pp. 840–847, 2004.
- [25] "Cst Studio Suit 2018 [Online]." Available at <http://www.cst.com>.
- [26] C. A. Balanis, *Antenna theory: Analysis and design*, p. 84–88. Wiley, 1997.
- [27] V. Rumsey, "On the design and performance of feeds for correcting spherical aberration," *IEEE Transactions on Antennas and Propagation*, vol. 18, no. 3, pp. 343–351, 1970.
- [28] C. A. Balanis, *Advanced engineering electromagnetics*, p. 314–323. J. Wiley & Sons, 2012.
- [29] D. M. Pozar, *Microwave Engineering*, p. 121–125. JohnWiley & Sons, Inc., 4 ed., 2011.
- [30] C. A. Balanis, *Advanced engineering electromagnetics*, p. 180–253. J. Wiley & Sons, 2012.
- [31] S. O. Dabironezare, *Fourier Optics Field Representations for the Design of Wide Field-of-View Imagers at Sub-millimetre Wavelengths*. PhD thesis, 2020.
- [32] C. A. Balanis, *Antenna theory: Analysis and design*, p. 144–150. Wiley, 1997.